The Dissertation Committee for Alok Arun Warey
certifies that this is the approved version of the following dissertation**:**

Development of an Electronic Sensor for Engine Exhaust Particulate Measurements

Committee:

Matthew J. Hall, Supervisor

Ronald D. Matthews

Ofodike A. Ezekoye

Janet L. Ellzey

Noel T. Clemens

Development of an Electronic Sensor for Engine Exhaust Particulate Measurements

by

Alok Arun Warey, B.E.; MSE

Dissertation
Presented to the Faculty of the Graduate School of
The University of Texas at Austin
in Partial Fulfillment
of the Requirements
for the Degree of

Doctor of Philosophy

The University of Texas at Austin
August 2005

Acknowledgements

I would first like to thank my advisor, Dr. Matthew Hall, for his guidance and encouragement throughout the course of the research project. I am very fortunate to have had the opportunity to work with him.

I would like to thank Dr. Ron Matthews and Dr. Ofodike Ezekoye for their guidance and support.

Thanks to the rest of the members of my dissertation committee: Dr. Janet Ellzey and Dr. Noel Clemens.

Thanks to the shop personnel: Curtis Johnson, and Don Artieschoufsky. Thanks to my fellow Thermal/Fluids graduate students especially Rochan Upadhyay for help with the model.

Thanks to Horiba Instruments Inc. for their guidance and support of this research.

Finally, I want to thank my brother Rohan and my parents for their support and encouragement.

Development of an Electronic Sensor for Engine Exhaust Particulate Measurements

Publication No. ___________

Alok Arun Warey, Ph.D.
The University of Texas at Austin, 2005

Supervisor: Matthew J. Hall

A new electronic sensor has been developed to measure the time-resolved concentration of carbonaceous particulate matter (PM) emitted in engine exhaust. The sensor is approximately the size of a standard automotive spark-plug or lambda sensor and can be mounted directly in the engine exhaust. It consists of a pair of closely spaced electrically isolated electrodes that protrude into the exhaust flow. One electrode is given a voltage bias of approximately1000 V while the other is the signal electrode. The sensor is capable of providing cycle-resolved feedback on the carbonaceous PM concentration in the exhaust to the engine control unit (ECU), thereby enabling real-time control of engine operating parameters. The sensor was tested in exhaust flows from a single cylinder diesel engine and from a steady-state acetylene diffusion flame in a flow tunnel. Steady-state engine measurements were made over a range of speed and load conditions while transient measurements were performed during engine start-ups and accelerations. The sensor response was compared to an opacity meter, gravimetric filter measurements, an aerodynamic particle sizer and a light scattering nephelometer. The output of the sensor compared well with exhaust opacity for the transient measurements and to filter mass loading for the steady-state tests.

Various parameters that affect the performance of the electronic sensor were studied. Parameters considered included sensor electrode length, diameter, electrode spacing, applied bias voltage, bulk flow velocity across the sensor electrodes, and the concentration of carbonaceous particulate matter in engine exhaust. The sensor signal varied linearly with the carbon mass concentration in the exhaust, the applied bias voltage and electrode length; it varied exponentially with the flow velocity, and had an inverse power dependence on the spacing between the electrodes. Electrode diameter did not have a significant effect on the sensor signal. A correlation was developed to predict the sensor signal under any engine operating condition and values of these parameters.

Based on the experimental data a hypothesis explaining the physical mechanism governing sensor behavior, regarding the charge transport between the two electrodes of the sensor, was proposed. A 1-D drift-diffusion model was developed to support this hypothesis.

TABLE OF CONTENTS

List of Figures……………………………………………………………….……x

List of Tables……………………………………………………………….…..xvii

Chapter 1: Introduction..1

- 1.1 Nature of Particulate Matter..4
- 1.2 PM Formation Mechanisms in Engines 7
  - 1.2.1 Particulate Nucleation 7
  - 1.2.2 Particulate Growth and Agglomeration...9
- 1.3 Review of Current PM Measuring Techniques................................10
- 1.4 Motivation for the Development of an Electronic PM Sensor..........22
- 1.5 Overview 23

Chapter 2: Experimental Setup 26

- 2.1 Acetylene Flame Test Rig...26
- 2.2 Engine...28
- 2.3 Dynamometer..31
  - 2.3.1 DYNOMAX Software...33
- 2.4 Exhaust Test Setup..34
- 2.5 Nephelometer 39
- 2.6 Aerodynamic Particle Sizer...44

Chapter 3: Sensor Design and Development 46

- 3.1 Sensor Design...46
  - 3.1.1 Sensor Construction 48
  - 3.1.2 Sensor Electronics...49
  - 3.1.3 Signal Conditioning..52

3.2 Sensitivity to SOF ... 58
3.3 Sensitivity to the Natural Charge ... 59
3.4 Effect of Electrode Orientation ... 60
3.5 Effect of Vibration, Flow Pulsation and Exhaust Temperature ... 62
3.6 Effect of Asymmetric Electric Field ... 63
3.7 Sensor Fouling ... 65
  3.7.1 Baseline Drift ... 73

Chapter 4: Performance Characteristics & Principle of Operation ... 78

4.1 Performance Characteristics ... 78
  4.1.1 Effect of Electrode Spacing ... 78
  4.1.2 Effect of Electrode Length ... 81
  4.1.3 Effect of Applied Voltage ... 83
  4.1.4 Effect of Flow Velocity ... 84
  4.1.5 Effect of Carbon Mass Concentration ... 90
4.2 Mechanism Governing Sensor Behavior ... 98
4.3 1-D Drift-Diffusion Model ... 116

Chapter 5: Results and Discussion ... 122

5.1 Acetylene Flame ... 122
5.2 Diesel Engine ... 125
  5.2.1 Transient Measurements ... 125
  5.2.1 Steady-State Measurements ... 128
  5.2.3 Crank-Angle Resolved Measurements ... 139
5.3 Nephelometer Comparison ... 146
5.4 Aerodynamic Particle Sizer ... 150

Chapter 6: Conclusions and Recommendations for Future Research 154

6.1 Recommendations for future work 156

Appendix A Engine Specifications 157

Appendix B Error and Uncertainty Analysis 158

B.1 Electrode Spacing 158

B.2 Electrode Length 160

B.3 Applied Bias Voltage 161

B.4 Flow Velocity 162

B.5 Carbon Mass Concentration 163

B.6 Uncertainty Analysis 164

References 167

VITA 174

LIST OF FIGURES

Figure 1.1: Evolution of emissions regulations for heavy duty diesel engines [3]..3

Figure 1.2: Chain-like structure of particle aggregates [6]………………………..5

Figure 1.3: A schematic representation of PM formation in combustion [11]……7

Figure 1.4: Schematic of a TEOM [17]……………………………………….11

Figure 1.5: Schematic of the Condensation Particle Counter [18]………………12

Figure 1.6: Schematic of the Differential Mobility Analyzer [18]………………13

Figure 1.7: Schematic of the Scanning Mobility Particle Sizer [18]…………….15

Figure 1.8: Impaction stages of a cascade impactor [19]………………………...16

Figure 1.9: Schematic of the Electrical Low-Pressure Impactor [20]…………...17

Figure 1.10: Optical layout of a LII system [23]………………………………...19

Figure 1.11: Nephelometer main housing [2]……………………………………20

Figure 1.12: Smoke sensor system [27]………………………………………….21

Figure 2.1: Picture of the metal flow tunnel [5]………………………………….27

Figure 2.2: Front and top view of the air blaster setup [5]………………………28

Figure 2.3: The Yanmar L-Series Engine [29]…………………………………..29

Figure 2.4: The DynoMite Water Brake and its Accessories [29]………………31

Figure 2.5: DYNOMAX Console Screen [29]…………………………………..33

Figure 2.6: Schematic of the experimental set up [30]…………………………..35

Figure 2.7: Picture of the engine and dyno setup [29]…………………………...36

Figure 2.8: Picture of the exhaust setup [31]…………………………………….37

Figure 2.9: Microbalance and electrical hot plates………………………………38

Figure 2.10: Nephelometer main housing [2]……………………………………39

Figure 2.11: Theoretical Mie scattering patterns [2]……………………………41

Figure 2.12: Mass loading correlation [32]………………………………………43

Figure 2.13: Aerodynamic Particle Sizer [34]…………………………………...44

Figure 2.14: Aerodynamic Particle Sizer with the Diluter on top [36]…………..45

Figure 3.1: Schematic of the sensor system……………………………………..47
Figure 3.2: Construction schematic of the sensor [5]……………………………49
Figure 3.3: Photograph of a typical sensor………………………………………49
Figure 3.4: Op-amp connection diagram [37]……………………………………50
Figure 3.5: Current to voltage converter circuit [38]…………………………….50
Figure 3.6: Charge amplifier schematic [5]……………………………………...51
Figure 3.7: Sensor output for an engine start and two revs (current to voltage converter)……………………………………………………………...52
Figure 3.8: Sensor output for an engine start and two revs (charge amplifier)….53
Figure 3.9: Sensor output for an engine rev……………………………………...54
Figure 3.10: Voltage follower circuit…………………………………………….55
Figure 3.11: Low pass filter circuit………………………………………………56
Figure 3.12: Sensor output for an engine start and two revs with a voltage follower and a low pass filter……………………………………………….57
Figure 3.13: Sensor output for an engine rev with a voltage follower and a low pass filter…………………………………………………………………58
Figure 3.14: Sensor output for an engine start followed by three accelerations when installed downstream of a filter………………………………………59
Figure 3.15: Sensor signal with no bias voltage…………………………………60
Figure 3.16: Effect of electrode orientation on the sensor signal………………..61
Figure 3.17: Sensor and opacity during engine start-up and revs………………..63
Figure 3.18: Photograph of sensor with dissimilar electrodes…………………...64
Figure 3.19: Effect of asymmetric electric field…………………………………65
Figure 3.20: Sensor signal for continuous engine operation……………………..66
Figure 3.21: Photograph of the sensor with platinum coated electrodes………...67
Figure 3.22: Photograph of enclosures for the sensor electrodes………………..68
Figure 3.23: Photograph of a new sensor design………………………………...69

Figure 3.24: Photograph of a new sensor design to minimize sensor fouling…...70
Figure 3.25: Photograph of a sensor designed to minimize sensor fouling……...70
Figure 3.26: Sensor output from two sensors for multiple engine starts and continuous operation at 60% of full load……………………………………...72
Figure 3.27: Sensor output for an engine start followed by continuous operation at 60% of full load for about 40 minutes……………………………………...73
Figure 3.28: Drift in the baseline level of two sensors during continuous operation at 60% of full load in a PVC pipe………………………………………..74
Figure 3.29: Effect of hot air flow across the sensor on the signal and baseline level……………………………………………………………………………75
Figure 3.30: Drift in the sensor baseline with no exhaust flow past the electrodes ……………………………………………………………………………76
Figure 4.1: Photograph of the three sensors with different electrode spacing…...79
Figure 4.2: Effect of electrode spacing on sensor signal for five engine load conditions……………………………………………………………………...80
Figure 4.3: Power values for five engine load conditions……………………….81
Figure 4.4: Photograph of the “U” shaped sensor………………………………..82
Figure 4.5: Effect of electrode length on sensor signal for two engine load conditions……………………………………………………………………...83
Figure 4.6: Effect of applied voltage on the sensor signal……………………….84
Figure 4.7: Effect of flow velocity on the signal magnitude of sensor 1………...86
Figure 4.8: Effect of flow velocity on the signal magnitude of sensor 2………...87
Figure 4.9: Effect of flow velocity on the signal magnitude of sensor 3………...88
Figure 4.10: Effect of flow velocity on the signal magnitude of sensor 4……….89
Figure 4.11: Correlation between the sensor signal and filter mass loading for sensor 1………………………………………………………………………..92

Figure 4.12: Correlation between the sensor signal and filter mass loading for sensor 2……………………………………………………………..93

Figure 4.13: Correlation between the sensor signal and filter mass loading for sensor 3……………………………………………………………..94

Figure 4.14: Comparison of experimental sensor signal to the correlation at constant engine speed of 1250 RPM and variable load…………………….96

Figure 4.15: Comparison of experimental sensor signal to the correlation at engine idle and speeds of 1250, 1500 and 2000 RPM……………………………...97

Figure 4.16: Comparison of experimental sensor signal to the correlation at engine idle and speeds of 1250, 1500, 1750 and 2000 RPM……………………….98

Figure 4.17: Schematic of the sensor mechanism………………………………100

Figure 4.18: Normalized Conductance (σ') vs. Filter mass loading for the three sensor designs………………………………………………………..105

Figure 4.19: Normalized Conductance (σ') vs. Filter mass loading for electrode spacing raised to power 1.4……………………………………………..106

Figure 4.20: Two views of the sensor with plate shaped electrodes……………108

Figure 4.21: Normalized Conductance (σ') vs. Filter mass loading for two different electrode spacing values of the plate shaped sensor geometry….109

Figure 4.22: Photograph of the two sensors with thin wires……………………110

Figure 4.23: Normalized Conductance (σ') vs. Filter mass loading for two sensors with small diameter electrodes……………………………………111

Figure 4.24: Normalized Conductance (σ') without electrode diameter vs. Filter mass loading for the sensors with electrode diameter of 1.65 mm………..112

Figure 4.25: Normalized Conductance (σ') without electrode diameter vs. Filter mass loading for the sensors with electrode diameter of 0.635 mm………113

Figure 4.26: Normalized Conductance (σ') without electrode width and electrode spacing of power 1.6 vs. Filter mass loading for the sensor with plate shaped electrodes……………………………………………………114
Figure 4.27: Computational domain for the model……………………………..116
Figure 4.28: Current values predicted by the model and measured experimentally ………………………………………………………………………..119
Figure 4.29: Effect of electrode spacing evaluated by the model and measured experimentally at 1250 RPM and 50% of full load……………………….120
Figure 5.1: Sensor output for different flame heights in flow tunnel…………..123
Figure 5.2: Sensor output for a pulsating acetylene flame……………………...124
Figure 5.3: Sensor output when the rotameter is set to full-scale reading……...124
Figure 5.4: Sensor output and exhaust opacity for an engine start followed by two accelerations………………………………………………………….126
Figure 5.5: Sensor and opacity during engine start-up…………………………127
Figure 5.6: Sensor and opacity for high flow-rate of purge air………………...127
Figure 5.7: Sensor output of a typical geometry for increasing engine load at a constant speed of 1250 RPM…………………………………………...129
Figure 5.8: Sensor output of another design for increasing engine load at a speed of 1250 RPM…………………………………………………………129
Figure 5.9: Reproducibility of sensor signal and filter mass loading at engine idle ………………………………………………………………………..130
Figure 5.10: Reproducibility of sensor signal and filter mass loading at 25% of full load………………………………………………………………131
Figure 5.11: Reproducibility of sensor signal and filter mass loading at 50% of full load………………………………………………………………131
Figure 5.12: Reproducibility of sensor signal and filter mass loading at 75% of full load………………………………………………………………132

Figure 5.13: Reproducibility of sensor signal and filter mass loading at 90% of full load……………………………………………………………………132
Figure 5.14: Summary of mean sensor output and mean filter mass loading for different loads at a constant engine speed 1250 RPM…………………….133
Figure 5.15: Correlation between the mean sensor output and filter mass loading…………………………………………………………………..134
Figure 5.16: Photograph of filters used at idle and 25% of full load…………...135
Figure 5.17: Difference between heated and unheated filters at five load conditions………………………………………………………………….136
Figure 5.18: EDS spectra for filters at the five engine load conditions………...137
Figure 5.19: SEM photo of a particle deposited on the filter paper…………….138
Figure 5.20: Carbon composition along the yellow line………………………..139
Figure 5.21: Sulfur composition along the yellow line…………………………139
Figure 5.22: Sensor output for 1 second at 1250 RPM…………………………140
Figure 5.23: Sensor output for 1 second at 2000 RPM…………………………140
Figure 5.24: Crank-angle resolved output of the sensor, opacity meter and optical switch for one engine cycle……………………………………………..142
Figure 5.25: Crank-angle resolved signal from the DPS [45]………………….143
Figure 5.26: Crank-angle resolved output of the sensor, opacity meter and optical switch for one engine cycle with high purge air flow rate………………...145
Figure 5.27: Crank-angle resolved output of the sensor and pressure transducer signal for one engine cycle……………………………………………..146
Figure 5.28: Sensor output and mass loading measured by unheated filters and nephelometer for five engine load conditions at 1250 RPM……………...147
Figure 5.29: Correlation between sensor output and mass loading measured by nephelometer…………………………………………………..………..148

Figure 5.30: Mass loading determined by the sensor, unheated filters and nephelometer for five engine load conditions at 1250 RPM……………...149
Figure 5.31: Number concentration measured by the APS at 1250 RPM and 50% of full load…………………………………………………………………151
Figure 5.32: Sensor output and C/SOF ratio determined from APS measurements for five load conditions at 1250 RPM……………………………………..152
Figure 5.33: C/SOF ratio during engine start-up……………………………….153

LIST OF TABLES

Table 1. Specifications of the test engine 29
Table 2: Specifications for sensors with different electrode spacing 79
Table 3: Specifications for sensors of different electrode lengths 82
Table 4: Design specifications for the different sensors 85
Table 5: Flow velocities for different engine speeds and pipe diameters 85
Table 6: Specifications for the different sensors 91
Table 7: Specifications for two configurations of the ‘plate’ sensor 107
Table 8: Specifications of the sensors with thin electrodes 110
Table A.1. Yanmar L100EE Specifications (yanmar.com) 157
Table B.1: Standard error of fit for varying electrode spacing under five load conditions at 1250 RPM 159
Table B.2: Standard error of fit for varying electrode length under two load conditions at 1250 RPM 160
Table B.3: Standard error of fit for different values of the applied bias voltage at two engine speeds of 1250 and 1500 RPM 161
Table B.4: Standard error of fit for ‘Sensor 1’ 162
Table B.5: Standard error of fit for ‘Sensor 2’ 163
Table B.6: Standard error of fit for ‘Sensor 3’ 163
Table B.7: Standard error of fit for ‘Sensor 4’ 163
Table B.8: Standard error of fit for the two sensors 164
Table B.9: Uncertainty values at the five engine operating conditions for zero-order uncertainty in the flow velocity 166
Table B.10: Uncertainty values at the five engine operating conditions for an uncertainty of 0.5 m/s in the flow velocity 166

Chapter 1: Introduction

There is increasing concern about the potential health hazards of particulate matter (PM), which has prompted increasingly stringent standards on PM emissions from automobiles and trucks. Medical researchers generally agree that particles of less than one micron in diameter are of primary concern, as these small particles tend to penetrate the natural filtration system of the human respiratory system. Some of the dominant sources of small particle emission are combustion-related processes, most notably the internal combustion engines in light and heavy-duty vehicles.

Many important new studies have been published, which show that breathing particulate matter at concentrations allowed by the current standards can likely cause significant health effects, including premature death and an increase in respiratory illness [1]. Several recently published community health studies indicate that exposure to particle levels well below the existing particulate matter standards is linked to respiratory and cardiovascular-related problems. These negative effects include premature death, hospital admissions from respiratory causes, and increased respiratory symptoms. Long-term exposure to particulate matter may increase the rate of respiratory and cardiovascular illness and reduce life span [1].

A less severe effect imposed by particulates is decreased service life of machinery exposed to high levels of PM. In gas turbine engines, the life expectancy of the blades is severely reduced as PM levels increase, and diesel engines suffer from accelerated wear under high PM concentrations [2].

Since 1998, particulate matter emission regulations in the US for heavy-duty diesel engines have mandated a reduction from 0.6 g/bhp-hr to the present level of 0.1 g/bhp-hr. Though this is a large improvement there is a requirement for an additional order-of-magnitude reduction, to 0.01 g/bhp-hr by 2007. Beginning in 2004, all passenger cars and light-duty trucks sold in the U.S. will be required to meet the same emission regulations regardless of the fuel type (EPA Tier 2). Thus, for the first time gasoline-fueled vehicles will have to meet particulate matter emission standards that in the past have only been required of diesel-fueled vehicles [3]. Gasoline engines, in general, are known to emit particulates during cold start, and direct-injection spark-ignition engines (DISI) have been shown to produce measurable PM during lean burn operation. A study comparing a DISI vehicle to a PFI vehicle over the FTP and US-06 cycles showed that while the PFI vehicle produced no detectable PM, the DI engine produced 0.015 g/mi of PM over the FTP cycle [4]. This level of PM passes the Tier 1 and LEV standards but fails the LEV 2 standard. So current port fuel-injected gasoline engines with catalysts will have no difficulty meeting the 2004 levels, but it is uncertain at this time if the new generation of direct-injection gasoline engines will be able to achieve certification [3]. All the improvements in diesel combustion technology achieved to date have resulted in a large reduction in the size of the emitted particles, but at the expense of a large increase in their number. It will take a major effort to meet the 2007 regulations and will most likely require the use of a particulate trap on all heavy-duty diesel engines and tighter control of engine-out particulate emissions. The evolution of emissions regulations for heavy duty diesel engines is shown in Figure 1.1.

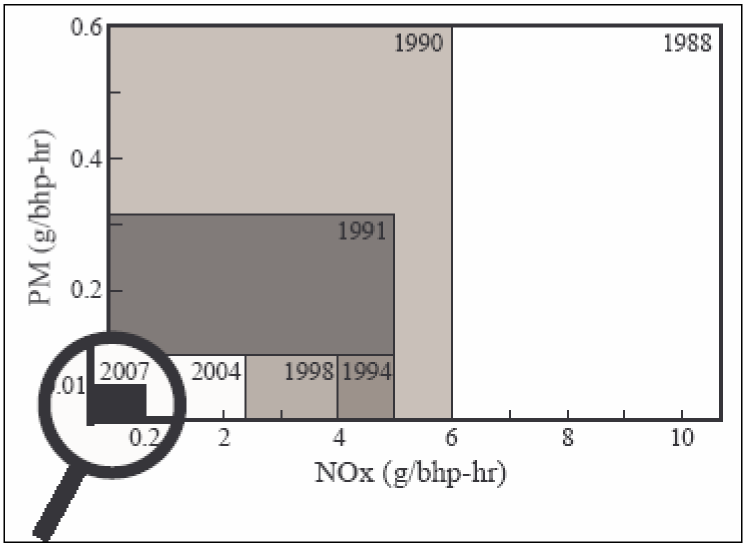

Figure 1.1: Evolution of emissions regulations for heavy duty diesel engines [3]

But this large reduction in total particulate mass will also create a new problem of measuring PM emissions reliably. The present gravimetric procedure of weighing an exhaust sample collected on a filter paper may be impractical because of the long time required to collect mass sufficient enough to be measured accurately. Today PM emissions are not as visible because the size of the particles emitted is several orders of magnitude smaller than that of engines, 10 years ago and mass emissions are lower. However, the number of particles emitted has increased by several orders of magnitude and poses a potential health concern. These new issues of size and number may prove to be important [3].

To meet the 2007 regulations, new diagnostic techniques will be needed to control the engine-out particulate emissions. Engine transients will play an ever-increasing role as engines continue to run cleaner. The filter paper method is completely useless in this regard. Only a few of the particulate measurement instruments used today are capable of real time measurements. Also all the diagnostic tools used today for PM measurement, consist of expensive equipment and cannot be used for on-board measurement. A PM sensor analogous to the lambda sensors used in gasoline-powered vehicles will prove to be extremely valuable in this regard. The sensor will provide cycle-resolved feedback on the PM concentration in the exhaust to the engine control unit (ECU), thereby enabling real-time control of engine operating parameters to lower PM emissions. It can also be used to monitor the performance of particulate traps [3, 5].

1.1 Nature of Particulate Matter

The generally accepted model of particulate matter is that it consists of a solid fraction, a soluble organic fraction (SOF), and sulfates [6]. The latter two are often combined into a single component, the volatile organic fraction (VOF) [3, 6]. The solid fraction is mostly carbon, which consists of molecules with C/H ratios ranging from 4 to 11. The solid fraction is commonly referred to as soot and it makes up the core of the particulate. Its density is approximately 2 g/cc. Morphologically, it consists of nearly spherical primary particles that cluster to form chain like aggregates [6]. The chain like structure of particulates is shown in Figure 1.2.

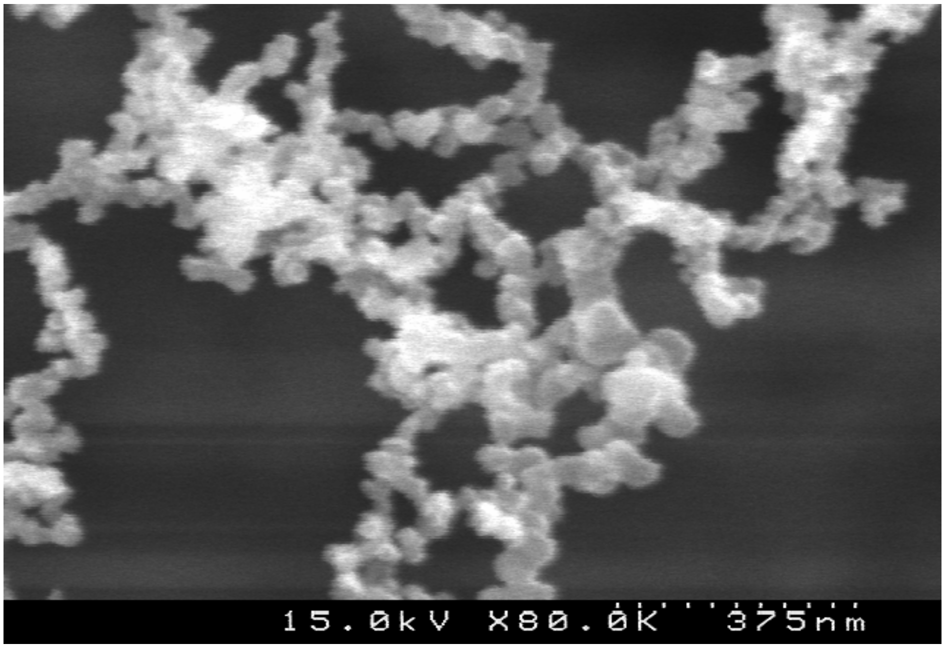

Figure 1.2: Chain-like structure of particle aggregates [6]

The diameters of these particles have been found to range from 10 nm to 50 nm as determined by specialized instruments and particulate micrographs [2]. Additional solid material occurs in the form of metal ash compounds derived from lubricating oil. The SOF consists of organic compounds with C/H ratios of 0.5-1.0, with a density of 0.8 g/cc. This includes the polycyclic aromatic hydrocarbons (PAH), which have two to six benzene rings joined in various forms. The SOF also includes partially oxidized products such as aldehydes and alcohols. Most of the SOF in PM is either adsorbed or condensed on the surface of the primary particles [3]. The sulfate content of PM is mainly hydrated sulfuric acid that is derived from fuel sulfur. Sulfur leaves the combustion chamber in the form of sulfur dioxide (>95%) and sulfur trioxide (2-5%). In the presence of water vapor the latter forms sulfuric acid, which is then adsorbed or absorbed by the primary particles [3]. The ratio of SOF to solid fraction in the particulates is affected by engine operating parameters. The relative amounts of SOF and solid fraction in the particulates has been found to vary with engine load – at light load, the particulate consists of mostly SOF, while at heavy load, the particulate consists of mainly solid carbon. Depending on how the particulate is formed, the SOF can comprise up to 75% of the particle mass [7, 8, 9, 10].

Particulate matter can be characterized by two distinct stages of development, particle formation or nucleation, and particle growth. The first stage is particle nucleation, where large numbers of spherical particles with diameters less than two-nm are formed in the combustion chamber. Stage two begins when these small particles grow in the post-flame environment and continue to grow as they pass into the lower temperature environment of the exhaust system. The two-nm spherules can grow to sizes up to 50-nm, and these particles then agglomerate into larger structures [3, 6]. A schematic representation of PM formation is shown in Figure 1.3.

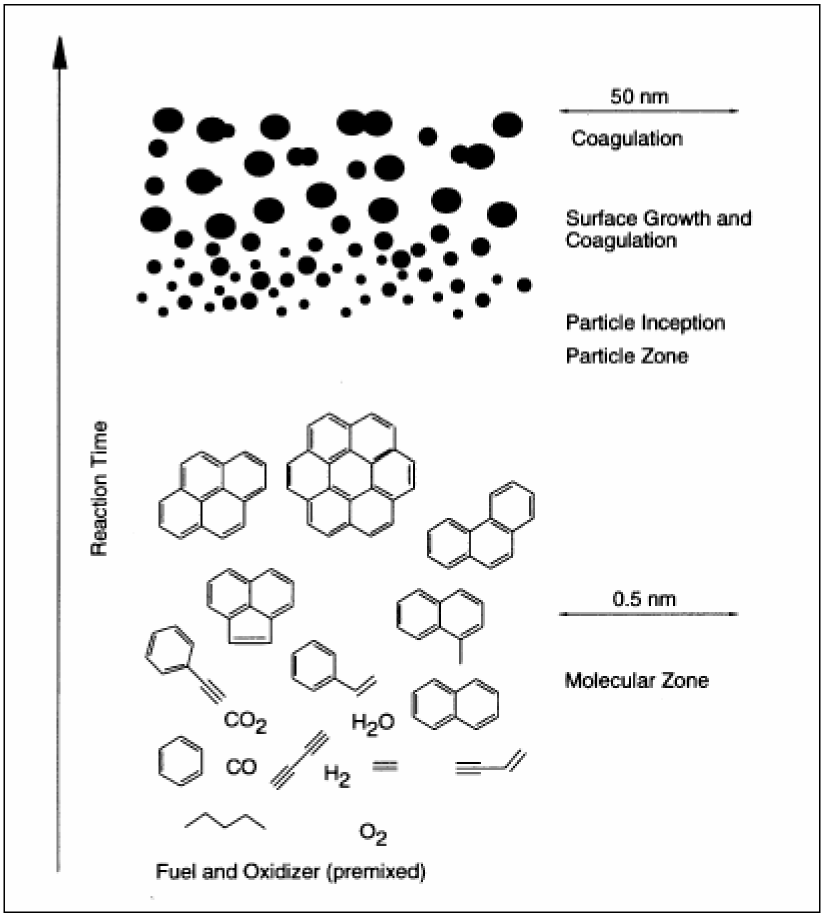

Figure 1.3: A schematic representation of PM formation in combustion [11]

1.2 PM Formation Mechanisms in Engines

1.2.1 Particulate Nucleation

Particulate nucleation in engines generally occurs from many different mechanisms. Particles can be formed when liquid fuel remaining in the cylinder after the passage of the flame front undergoes pyrolysis (the thermal degradation of organic materials at high temperatures under non-oxidative conditions), at which time the larger carbon - hydrogen molecules break down into smaller molecules of C_2H_2 and its higher analogues (C_nH_{2n}), which further dehydrogenate into molecules with a high carbon-to-hydrogen ratio (C/H ~ 4-11) [2, 6]. These carbon-rich molecules are often referred to as soot and they act as condensation sites for adsorption of SOF molecules.

Particulates also nucleate by homogeneous or gas-phase reactions involving unburned or partially oxidized hydrocarbons in the high temperature environment. The condensed products are mainly comprised of polycyclic aromatic hydrocarbons (PAH) and molecules with a high carbon-to-hydrogen ratio, which then serve as soot precursors [6].

According to Dec's model for soot formation in diesels [12], small soot particles nucleate just downstream of a standing rich flame that is downstream of the break-up length, where all of the liquid fuel has evaporated and some mixing with air has occurred via entrainment. These particles grow as they travel downstream in the jet especially in the recirculation zone near the jet head. The rich fuel vapor/air region of the jet is surrounded by a thin, near stoichiometric diffusion flame. The soot particles are oxidized on the fuel side of this diffusion flame while thermal NO_x is formed on the air side.

Particulates can also be formed from the products of heterogeneous-phase reactions when liquid fuel remaining after the flame front passes burns in the presence of oxygen in the post-flame high temperature environment. Since this reaction requires the presence of oxygen in the post-flame environment, PM nucleation from this mechanism increases at leaner air/fuel mixtures because the available post-flame oxygen concentration increases. This may be the case for diesel engines and for gasoline engines operating under stratified charge conditions [6].

A further particulate formation mechanism is reactions involving sulfur impurities in the hydrocarbon fuel. Current diesel and gasoline blends contain between 150-600 parts per million (ppm) of sulfur, which is oxidized in the combustion process to form sulfur dioxide. In vehicles equipped with oxidation catalysts, the sulfur dioxide is further oxidized to SO_3, which can then combine with water vapor to form sulfuric acid aerosol. The tendency of hydrated sulfuric acid to nucleate is believed to be the main source of nanoparticles that appear during dilution [3, 6].

Once particles nucleate, they can undergo growth and/or diminution by oxidation. Oxidation causes particles to diminish in size and follows an Arrhenius dependence on oxygen concentration and temperature [6, 7].

1.2.2 Particulate Growth and Agglomeration

After the nucleation stage, the soot precursors begin to grow immediately by adsorption, absorption, and condensation of the SOF molecules, which serves to increase particle size and mass. Once the temperature drops below approximately 500 °C the surface of the soot precursors becomes coated with adsorbed and condensed SOF matter where it resides in the form of a thin outer shell [2, 3]. The SOF molecules can adhere to the surface of the soot particles either chemically or physically (by van der Waals forces). Once the adsorbed layer develops around the particle, it can then absorb additional SOF molecules. Growth of particles via adsorption and absorption depends primarily on the availability of SOF molecules and the soot precursor surface area. Growth is enhanced by low temperature and high concentrations of both SOF molecules and particle surface area [7]. While adsorption and absorption begin as soon as particles and SOF molecules are brought in contact inside the combustion chamber, they contribute most substantially to PM mass when the exhaust is cooled and diluted, such as in the atmosphere. Condensation of SOF molecules on the particle occurs when the SOF vapor pressure exceeds its saturation vapor pressure in the sample air [2, 6].

Concurrently, the particles begin to combine with one another due to phoretic forces (coagulation). Growth via coagulation depends strongly on the number of particles nucleated, increasing as the number of nucleated particles increases. The combined effect of SOF accumulation and particle coagulation is the increase in primary particle diameter as well as the formation of larger particulate structures [6].

Particulate emission and composition are greatly affected by engine operating conditions, such as equivalence ratio, fuel injection timing in diesel engines, engine load, engine temperature, exhaust gas re-circulation (EGR), spark timing in spark-ignition (SI) engines, and fuel composition. These conditions directly impact cylinder temperature and pressure, fuel vaporization, and the amounts of available hydrocarbons and oxygen, all of which influence PM formation, oxidation, and composition [10, 13, 14, 15].

1.3 Review of Current PM Measuring Techniques

Besides the gravimetric/filter measurement technique there are several other instruments and techniques to measure PM mass loading as well as size distributions.

The tapered element oscillating microbalance (TEOM) is a widely used device for measuring PM mass loading in real time. A filter substrate is mounted on the tip of a hollow, tapered tube. As particles are deposited on the filter, the inertial mass increase alters the natural oscillating frequency of the tube, which is monitored to give a signal proportional to the total mass of the filter. Although the signal can be monitored with high temporal resolution, the sensitivity of the device is limited by the change in mass necessary to create a detectable change in oscillating frequency [3, 16]. A schematic is shown in Figure 1.4.

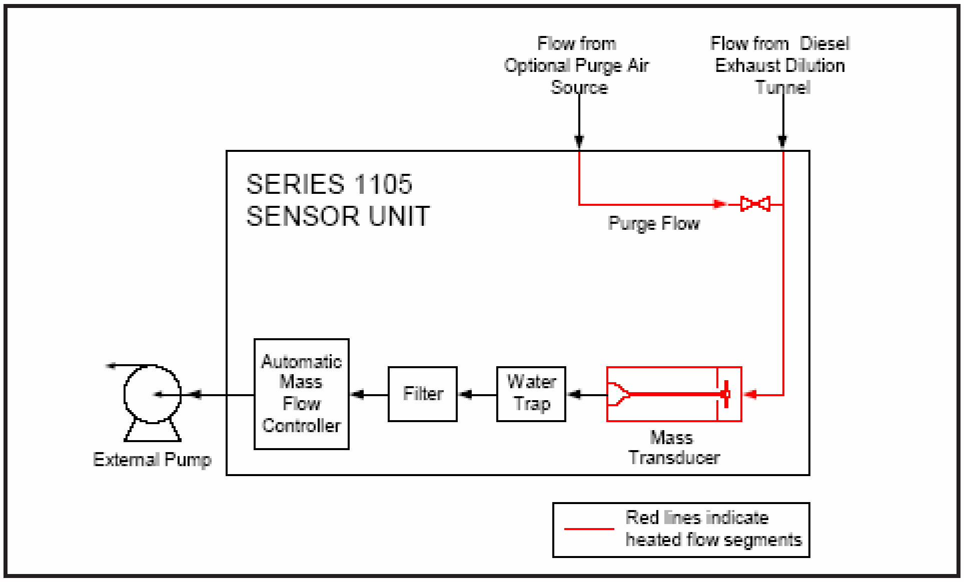

Figure 1.4: Schematic of a TEOM [17]

There are a number of techniques that measure PM volume fraction. The opacity meter measures the extinction of light as it traverses the exhaust stream. A smoke meter measures the decrease in reflectivity of a filter as it becomes soiled with PM [3].

The condensation particle counter (CPC) measures particle number by counting individual particles. Sufficient dilution of the exhaust is needed to reduce the number concentration to $< 10^5$ particles/cc to avoid multiple particles in the measurement volume. The diluted aerosol is saturated with alcohol vapor prior to entering a condenser, where it is cooled by thermal diffusion. The particles grow in size due to condensation of alcohol to about 2-3 μm and can be counted optically as they pass through a laser beam [2, 3]. A schematic is shown in Figure 1.5.

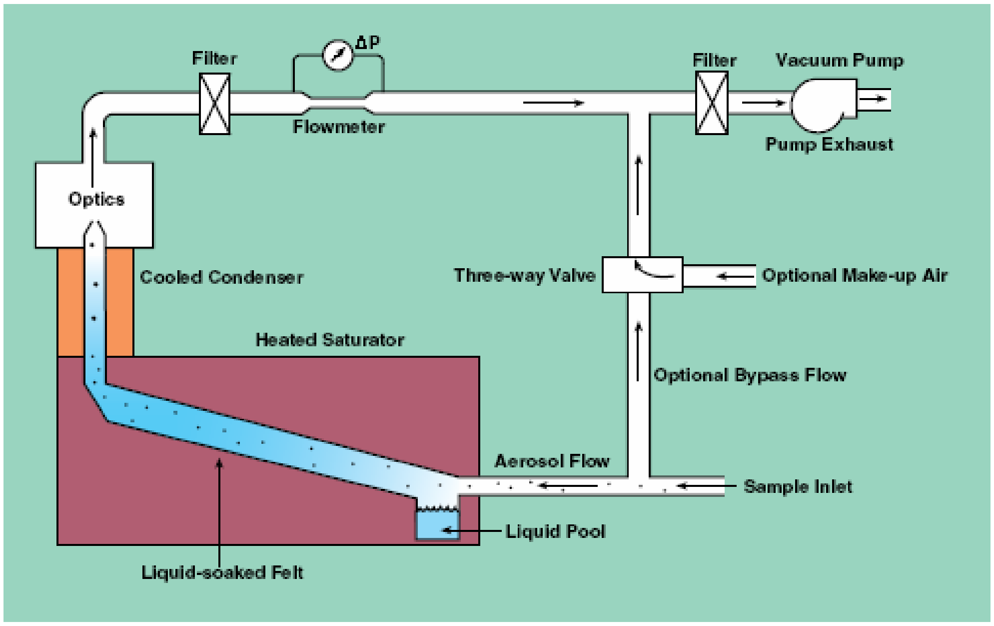

Figure 1.5: Schematic of the Condensation Particle Counter [18]

The Scanning Mobility Particle Sizer (SMPS) can determine particle size distribution by first charging the particles in a sample and then passing them though an electric field to separate them according to their electrical mobility in a Differential Mobility Analyzer (DMA) shown in Figure 1.6.

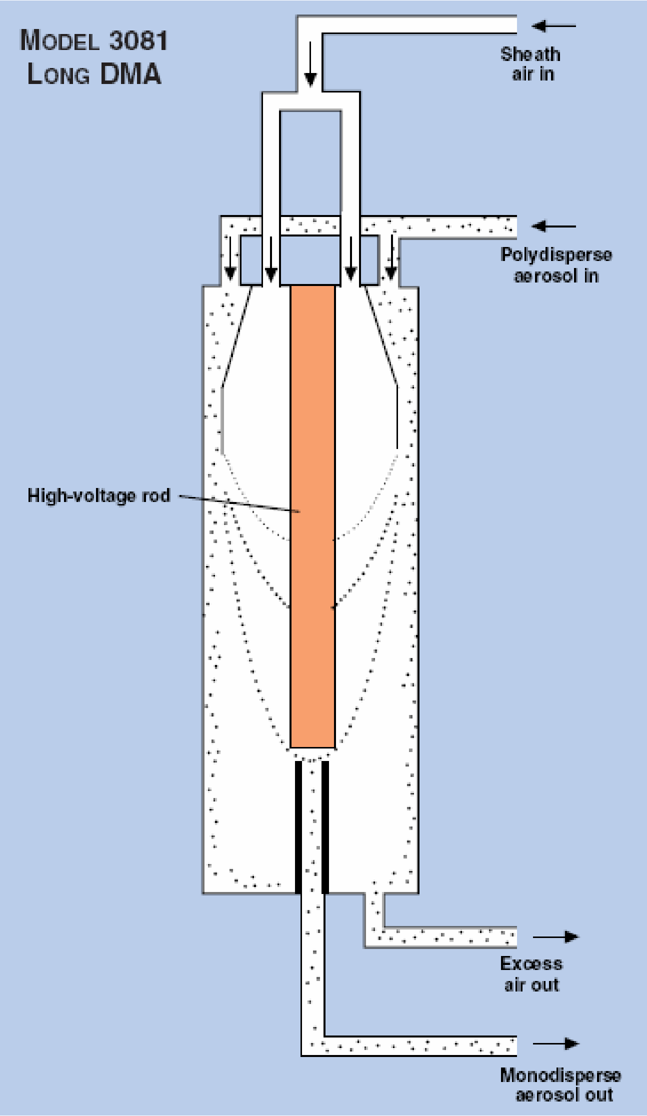

Figure 1.6: Schematic of the Differential Mobility Analyzer [18]

An electric field inside the DMA influences the flow trajectory of the charged particles. The DMA contains an inner cylinder that is connected to a negative power supply (0 to 10,000 VDC). This charged element provides a precise negative potential. Particles with negative charge are repelled towards and deposited on the outer wall. Neutral particles exit with the excess air. Particles with a positive charge move rapidly towards the negatively charged element. Only particles within a narrow range of electrical mobility have the correct trajectory to pass through an open slit near the DMA exit [18]. Electrical mobility is then related to the particle diameter, as particles with larger diameters have a higher inertia (lower electrical mobility) and drift more slowly in the induced electric field than smaller particles. The electric field strength and airflow rates are adjusted to account for particles of all sizes. The SMPS outputs the particle size distributions as well as integrated results: concentration, mean particle sizes and mode particle sizes, all of which are given on number, surface area, and volume-weighted bases. However, the SMPS can only resolve particle sizes below one micron, therefore the exhaust sample must be pre-filtered to remove particles larger than one micron before entering the SMPS. The SMPS is not capable of real time measurements and can only be used for steady state operation [2, 3]. However, Cambustion's fast PM analyzer is an SMPS capable of measurements in real time. The SMPS is commonly used in conjunction with a condensation particle counter (CPC) described above. A schematic of a SMPS is shown in Figure 1.7.

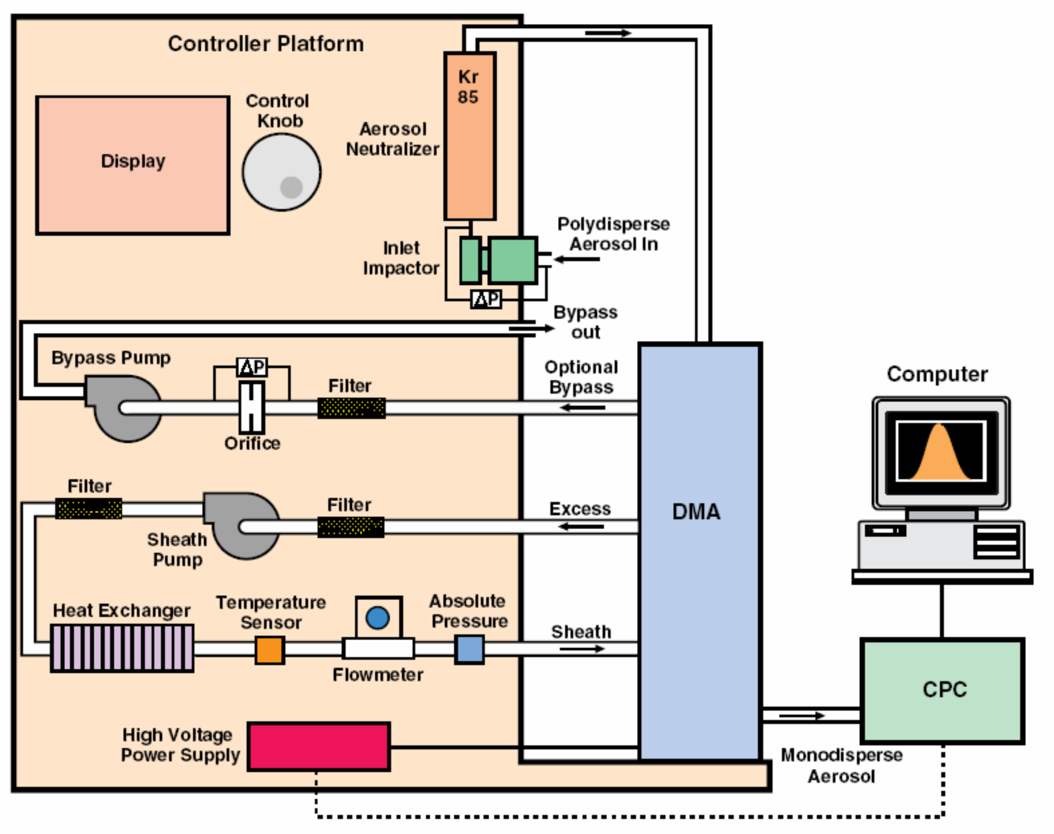

Figure 1.7: Schematic of the Scanning Mobility Particle Sizer [18]

A cascade impactor uses inertial mobility to separate particles by size. It uses several stages for removing particles of different sizes from the bulk air sample as shown in Figure 1.8. The separation of the aerosol particles is accomplished by passing the sample gas through jet orifices of successively lesser diameters with increasing gas jet velocities. The aerosol stream passing through a given nozzle is sharply accelerated away from a nearby collection plate. Particles in the aerosol stream having large enough inertia will not be able to accelerate with the bulk air stream and will therefore impact upon the collection plate while the other smaller particles will follow the airflow out of the impaction region. Several impactor stages are used, and each stage is responsible for removing a portion of aerosol particles in a discrete size range, depending on nozzle diameter and distance from the collection plate. Each collection plate is then weighed to determine the amount of particulate accumulation [2].

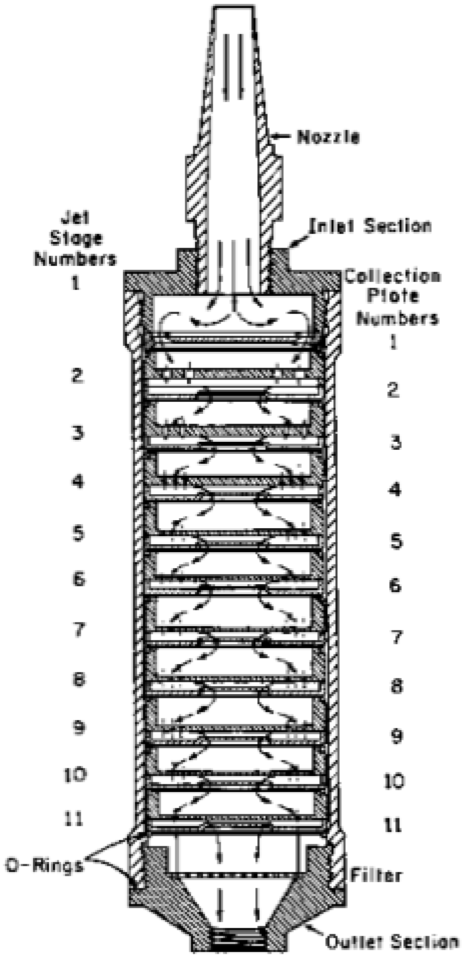

Figure 1.8: Impaction stages of a cascade impactor [19]

The electrical low-pressure impactor (ELPI) is capable of real-time measurements of particle diameters ranging from 30 nm to 10 microns. The operation of the ELPI is similar to the cascade impactor except the particles in the gas sample are first charged with a corona discharge. The charged particles then pass into a low-pressure impactor with multiple electrically isolated collection stages. As particles impact upon the collection plate, the electric current generated by the charged particles into each impactor stage is measured with an electrometer. As with the cascade impactor, the particle collection into each impactor stage is dependent on the aerodynamic size of the particles. Measured current signals from each stage are converted to aerodynamic size distribution using particle size-dependent relations describing the properties of the charger and the impactor stages [3]. A schematic of an ELPI system is shown in Figure 1.9.

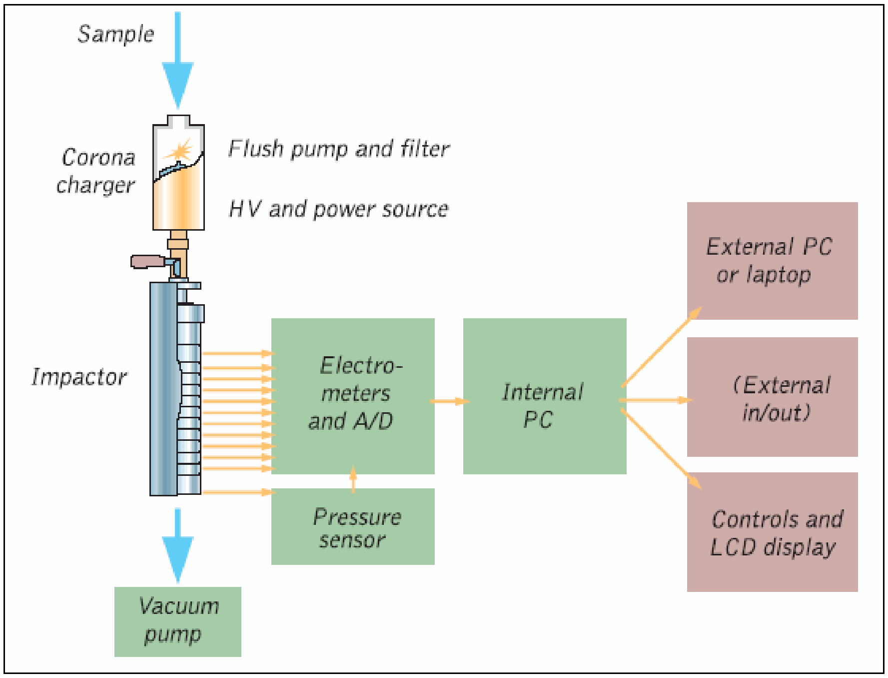

Figure 1.9: Schematic of the Electrical Low-Pressure Impactor [20]

Generally, the SMPS, ELPI, and CI require the sample to be diluted. Recent studies have shown that dilution of the exhaust samples can nucleate new particles. Also residence time and gas temperature can have a large impact on the nucleation and growth of particles. Thus diluting the exhaust sample has a strong impact on the particle size distribution, which might be a problem if particle size and/or number are regulated in the future [3].

Laser induced incandescence (LII) uses a high-energy laser beam to heat carbon particles to their vaporization temperature (~ 4000K). Any volatile material on the particles is vaporized in the process. Thermal radiation, incandescence, from the particles is then recorded and used to estimate the particle volume fraction and primary particle size. Particle volume fraction is obtained from the amplitude of the signal while the particle size is determined from the rate of decay of the incandescence signal. Since the non-carbonaceous particles absorb very little energy, LII selectively responds to carbon only [21]. Witze and co-workers [22] have also used LII for real time, in-situ measurements of the volatile fraction of diesel particulate matter. They used two laser pulses of comparable energy, separated by a time interval short enough to freeze the flow field, to measure the change in PM volume caused by laser-induced desorption of the volatile fraction. Exhaust dilution and cooling are not required for LII. The optical layout of a LII system is shown in Figure 1.10.

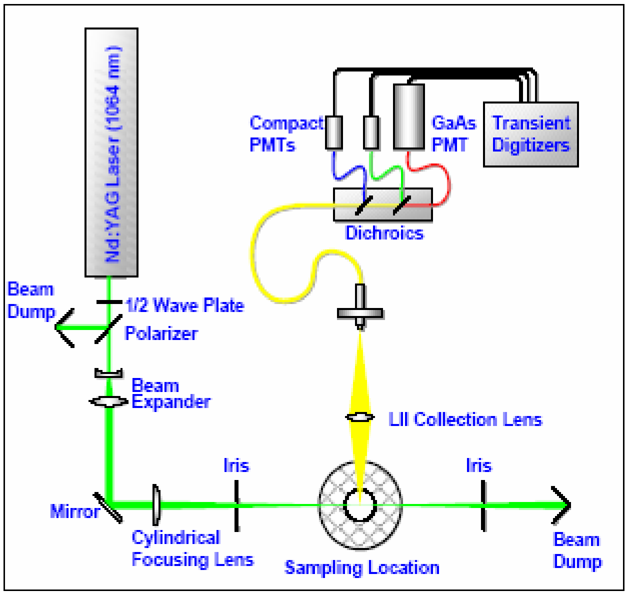

Figure 1.10: Optical layout of a LII system [23]

The nephelometer is a light scattering device capable of determining particle size and mass loading in an exhaust sample in real time. The light scattered by small particles (particle diameter on the order of the wavelength of the incident radiation) is dependent of the particle size. This angular scattering pattern can thus be used to determine the size of the particle. Some benefits of the real-time nephelometer measurement technique are PM measurements during transients, sensitivity to very low particulate mass loading, and minimal sample dilution [2, 6]. The main housing of a nephelometer is shown in Figure 1.11.

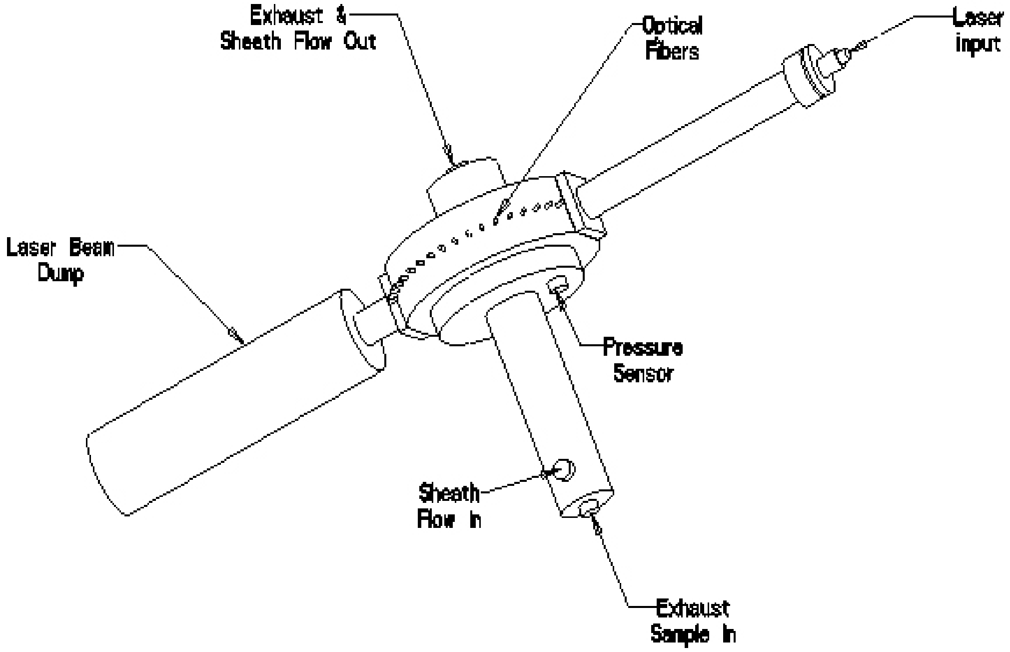

Figure 1.11: Nephelometer main housing [2]

Soot particles in diesel exhaust carry a natural charge and are electrically conductive [24-26]. Studies performed in diesel engines have shown that up to 70% of the particles are ionized [24-26]. Real-time smoke sensors have been developed to detect this natural charge on soot particles with limited success [24-26].

Allan and co-workers [27] have developed a smoke sensor based upon the ability of soot particles to affect the threshold current for arc-to-glow transition in spark discharges. The material at the cathode surface can have a strong effect on the current value for arc-to-glow transition. When a spark gap with metal electrodes is operated with repetitive spark discharges while in a soot laden gas flow, soot particles are continuously deposited upon the electrode surfaces and burned off by the sparks. If the peak spark current is high enough to allow the spark to begin in arc mode with a clean cathode, the presence of soot will result in sparks which remain in arc mode down to lower current levels. Depending upon the rate of deposition of soot on the cathode versus the rate of removal by the sparks, the relative arc activity during the sustaining period of the discharge will assume behavior somewhere between that of a clean metal cathode and that of a carbon cathode. By using signal processing techniques over a sufficient number of sparks, it is possible to obtain a signal that responds to changes in smoke levels. However their sensor had problems due to the temperature sensitivity of the sensor output and inconsistent sensitivity of the apparatus to smoke levels in the exhaust. Their smoke sensor system is shown in Figure 1.12.

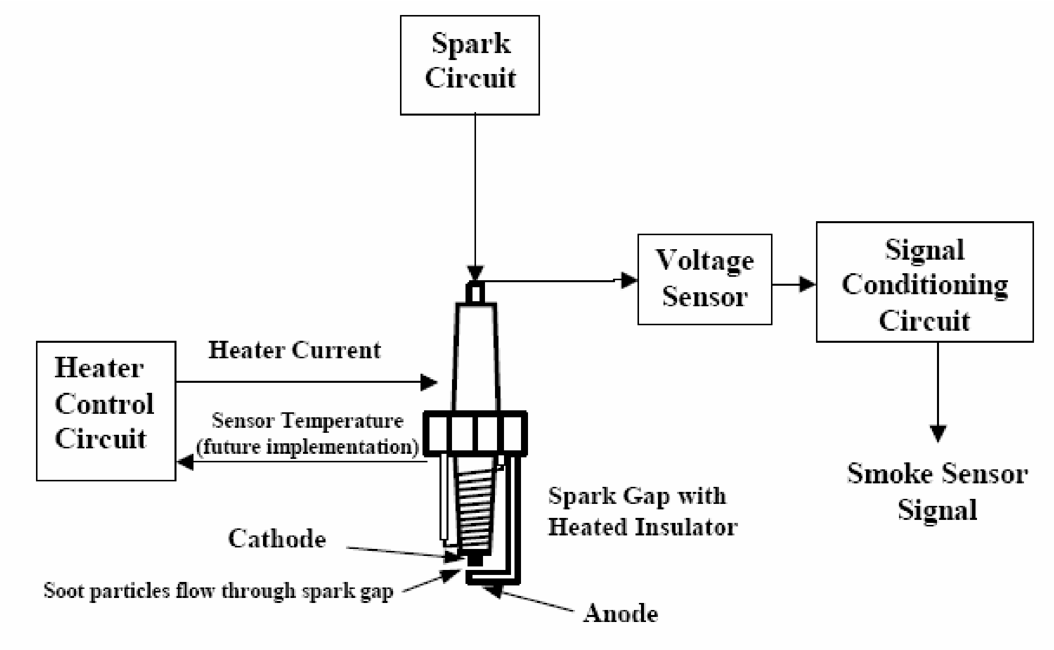

Figure 1.12: Smoke sensor system [27]

Ishida and co-workers [28] developed a sensor based on the principle of electron diffusibility between two electrodes by the dry soot in the exhaust. They imposed a voltage bias across a large cylindrically shaped anode in a PM laden flow. Since the conductivity of dry soot is significantly higher than that of SOF the change in the conductivity of diesel exhaust can be attributed to the dry soot. The change in aerosol conductivity is related to the change in microcurrent between the two electrodes. The change in detected current thus corresponds to the changes in concentration of soot particles in diesel exhaust. The electronic PM sensor developed in this research has a completely different geometry and operates at a much higher voltage than the sensor developed by Ishida and coworkers (1000 V vs. 150 V). The large annular geometry of their device was not suitable for in-situ measurements and was investigated as a research instrument. The present sensor is also much faster than their sensor.

1.4 Motivation for the Development of an Electronic PM Sensor

The motivation for the development of the sensor is the need to control engine-out particulate emissions from production diesel engines. All of the present techniques and instruments for PM measurement are bulky, require expensive equipment and cannot be used for on-board measurements. It is doubtful if the current instruments will have the sensitivity required for the new regulations. Industry will need new diagnostic tools to meet the 2007 and 2010 particulate matter regulations. Engine transients will play an ever-increasing role. Tighter control of PM emissions can be achieved if the ECU could get a real-time feedback on the PM concentration in the exhaust. For example consider the use of exhaust gas re-circulation in diesel engines. Exhaust gas re-circulation (EGR) is used to reduce NO_x emissions from light duty diesel engines. EGR reduces NO_x

because it dilutes the intake charge and lowers the combustion temperature. A practical problem in fully exploiting EGR is that, at very high levels, combustion becomes incomplete and unacceptable levels of particulate matter (PM) and hydrocarbons (HC) are emitted in the exhaust. The ECU needs a feedback signal so that it can use as much EGR as possible without producing unacceptable levels of PM [5]. Another application could be to detect failure of particulate traps.

What is needed is a PM sensor that can be mounted in the vehicle exhaust and which will provide cycle resolved feedback to the ECU. To achieve these goals the sensor has to satisfy the following requirements. First, the sensor needs to be small enough to be installed in the exhaust pipe. Second, it must provide the ECU with a signal correlated with the amount of soot being emitted. Third, the sensor has to be cost effective and durable.

1.5 Overview

This dissertation describes the development of a new electronic sensor capable of on-board measurement of the concentration of carbonaceous particulate matter in engine exhaust. The sensor is approximately the size of a standard automotive spark plug or oxygen sensor. It consists of a pair of closely spaced electrically isolated electrodes that protrude into the exhaust flow. One electrode is given a high D.C. voltage bias of 1000 V while the other electrode is connected to a custom built current to voltage converter circuit. The output of the current to voltage converter is passed through further signal conditioning and is then recorded by a PC based A/D data acquisition system.

This sensor makes use of the finite electrical conductivity of the carbonaceous fraction of the PM in the exhaust stream. The general mechanism governing sensor behavior is the formation of an electrically conductive channel between the two electrodes of the sensor, by the carbonaceous PM in the exhaust, thereby enabling a current flow. The carbonaceous PM in the exhaust thus acts like a resistance between the two electrodes. The idea for the PM sensor originated at the University of Texas and has been patented. The concept was successfully tested with a few prototypes in the exhaust of a steady-state acetylene diffusion flame in a previous project [5].

The sensor is capable of providing a cycle-resolved (or even crank-angle resolved) feedback on the carbonaceous PM concentration in the exhaust to the engine control unit (ECU). The sensor was tested in the exhaust of a single cylinder diesel engine and a steady-state acetylene diffusion flame under both transient and steady-state conditions. Various parameters that affect sensor performance were studied and a correlation was developed to predict the sensor signal for any geometry and engine operating condition. A hypothesis to explain the physical mechanism governing sensor behavior was proposed.

The experimental apparatus is discussed in Chapter 2. This includes the metal flow tunnel used for measurements with an acetylene flame, the Yanmar diesel engine, a water brake dynamometer and the exhaust setup. A nephelometer capable of measuring particle size and mass loading in real time and an aerodynamic particle sizer are also described. The sensor output was compared to both the instruments for steady-state tests.

Chapter 3 describes the key components of the electronic sensor and several tests that were conducted to investigate extraneous mechanisms that could contribute to the measured signal. Optimization of the sensor electronics is discussed. Various techniques investigated to minimize sensor fouling are also discussed.

Chapter 4 describes the study of various design parameters that affect the performance of the sensor. Parameters considered included sensor electrode length, diameter, electrode spacing, applied bias voltage, bulk flow velocity across the sensor electrodes, and the concentration of carbonaceous particulate matter in engine exhaust. A hypothesis to explain the principle of operation of the sensor is proposed. Development of a 1-D drift-diffusion model to support the hypothesis based on experimental observations is also discussed.

Chapter 5 presents the experimental results for the engine and the steady-state acetylene diffusion flame. Steady-state measurements were made over a range of speed and load conditions while transient measurements were performed during engine starts and accelerations. The sensor output was compared to gravimetric filter measurements, a light-scattering nephelometer and an aerodynamic particle sizer.

Chapter 6 summarizes this dissertation research, presents the corresponding conclusions and recommends future research in this area.

Chapter 2: Experimental Setup

The electronic PM sensor was tested in the exhaust flows from a single cylinder diesel engine and from an acetylene diffusion flame in a flow tunnel under both transient and steady–state conditions. Steady-state engine measurements were made over a range of speed and load conditions while transient measurements were performed during engine start-ups and accelerations. The sensor response was compared to an opacity meter, gravimetric filter measurements, a light scattering nephelometer and an aerodynamic particle sizer.

2.1 Acetylene Flame Test Rig

Tests with an acetylene diffusion flame were done in a 4 inch diameter metal flow tunnel as shown in Figure 2.1. The burner was constructed from stainless steel tubing with a 0.2 inch diameter orifice for the flame. The acetylene flame was located at one end of the flow tunnel and PM along with dilution air was pulled through the tunnel by an exhaust vent past the sensor. The flow rate of acetylene was varied to achieve different flame heights in a constant flow of dilution air. Once the flame was stable at a particular height, the sensor output was recorded.

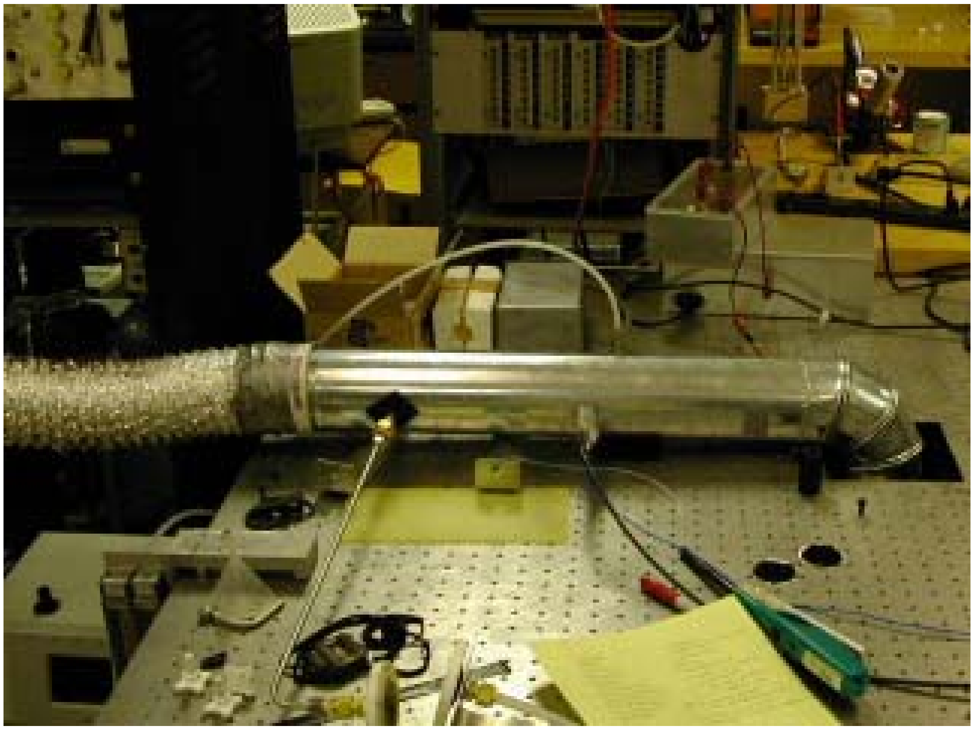

Figure 2.1: Picture of the metal flow tunnel [5]

To clean the sensor in between runs a ¼ inch copper tube was inserted into the flow tunnel. This tube was bent so that it aimed directly at the electrodes of the sensor without physically interfering with soot flow around the sensor. The other end of the tube was connected to a compressed air supply. A valve was used to control the compressed air, allowing the probe to be cleaned whenever necessary. A schematic of the “Air Blaster Setup” is shown in Figure 2.2 [5].

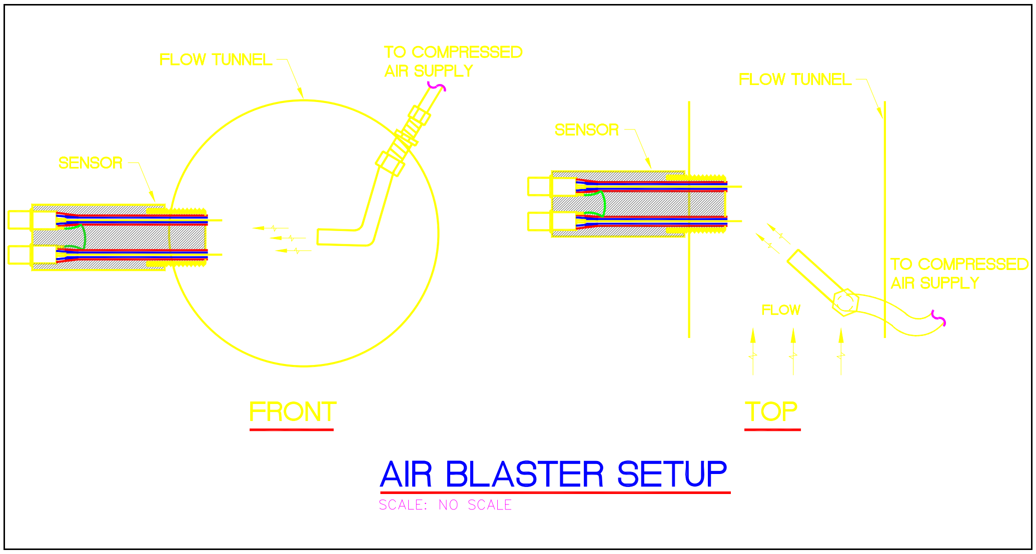

Figure 2.2: Front and top view of the air blaster setup [5]

2.2 Engine

The engine used in this research was a 0.418 L Yanmar L100EE single cylinder direct-injection diesel rated to produce 10 horsepower. The engine shown in Figure 2.3 is air-cooled and has a gravity-fed fuel tank mounted near the top of the cylinder. Specifications of the engine are given in Table 1. The complete specification sheet is listed in Appendix A.

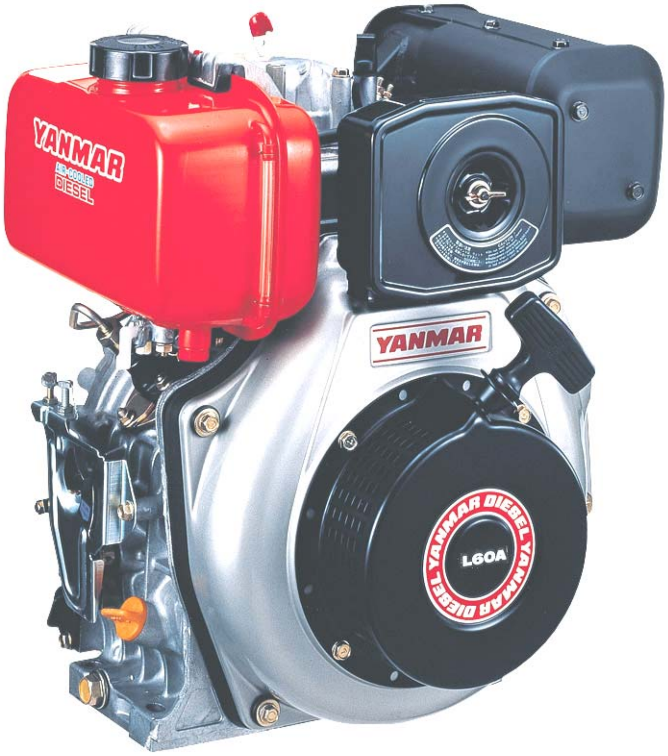

Figure 2.3: The Yanmar L-Series Engine [29]

Table 1. Specifications of the test engine

Specifications of the Test Engine	
Cylinders	1
Displacement (L)	0.418
Bore (mm)	86
Stroke (mm)	72
Compression Ratio	20:1

The engine offers both hand-start and an electric 12-Volt starter powered by an external battery. The engine has an alternator included in the starter system that negates the need for a charger on the test battery. The engine has an included muffler with a 1.5” tailpipe, which was left on for most of the tests. The muffler was later removed to make crank-angle resolved measurements with the sensor.

Since diesel engines have no throttle; during normal operation their torque output is dependent on the amount of fuel injected during the compression stroke. The fuel injection timing for this engine is about 17 degrees before top dead center (TDC) of compression and the fuel injection pressure is about 19.6 MPa. The fuel delivery is controlled by what is known as the “rack position,” which affects the length of time that the fuel injector is open and delivering fuel. The test engine has a completely internal fuel pump and the elements of injection control are inaccessible from the exterior of the engine [29]. The engine also has a fuel return line that brings excess fuel back to the fuel tank. The return line allows the fuel pump to have a larger volumetric flow rate, which increases pump longevity and has a side benefit of cooling the injected fuel. The Yanmar engine allows the operator to control rack position using a rotating lever mounted externally under the fuel tank. The rack was held in place by a set screw and jam nut. Once the desired torque was achieved, the jam nut was locked down and the torque was observed to ensure that it stayed constant.

The Power Take-Off (PTO) shaft is a horizontal, 1” diameter, keyed shaft, to which the dynamometer is attached [29]. A belt and pulley drive was used to achieve a torque reduction of 1.5:1 between the engine and the dynamometer. A toothed belt was used to avoid it from slipping [29].

2.3 Dynamometer

A dynamometer (dyno) is a device used to load an engine. There are several types, including eddy-current, electric, and water brake. The dynamometer used in these experiments was a water brake, shown in Figure 2.4, called the DYNO-Mite built by Land and Sea Inc.

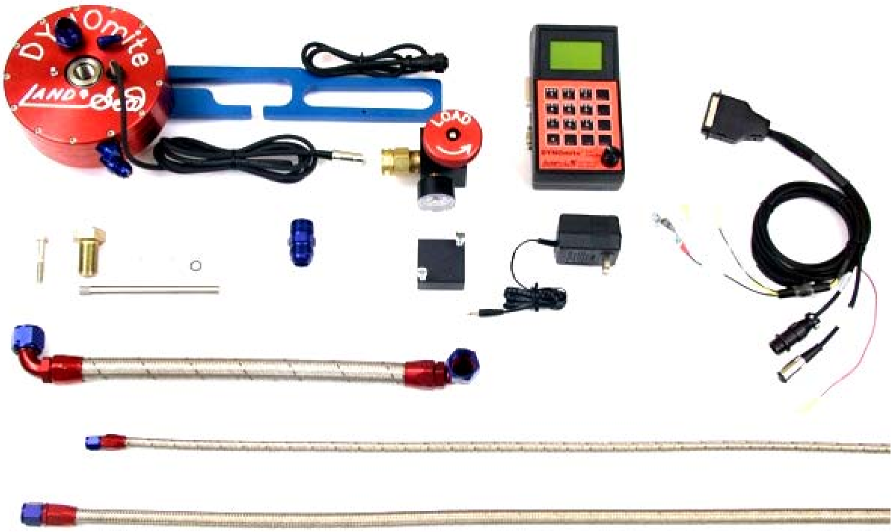

Figure 2.4: The DynoMite Water Brake and its Accessories [29]

The unit is 7” across, and is designed for small engines. The center of the pump impeller is designed to accept a ¾” keyed shaft, and the torque arm is mounted on the dyno housing. The torque arm is designed to hold the dyno in place while it is in use. The torque arm is held in place by the dyno setup, and a strain gauge mounted on the arm measures the torque. The dyno has a water inlet, an outlet, and a vent that allows air to both escape during testing and then re-enter when the water inlet is turned off. The amount of torque absorbed by the dyno depends on the water level inside the dyno. As the water level increases, the torque required to turn the blades also increases. The water flow into the dyno is regulated by the pressure valve mounted upstream of the dyno [29].

An automatic, computer controlled pressure valve was mounted upstream of the dyno. This device used a 12V-power supply to power a stepper motor that controlled the valve. The automatic valve interfaces with the test computer through Land and Sea’s full function harness. In addition to the automatic control valve, a pressure regulator was mounted further upstream. This was included in order to remove any unwanted effects of the varying pressure of the municipal water supply, which was the water source for the dyno in all the tests [29].

The dyno was also equipped with a Hall effect RPM sensor that tracks a magnet attached to one of the blades of the dyno. The output of the Hall effect sensor and the strain-gauge values from the torque arm are sent back to Land and Sea’s test computer. This LCD-based 4-fucntion computer can also interface with a PC via an RS-232 serial cable and Land and Sea’s proprietary software called, “DYNO-MAX 2000”. The computer can thus track and record the engine RPM and torque output [29].

The bearings on this dyno require occasional greasing and, because they are in such proximity to water, periodic replacement. The required parts were purchased at a bearing supply company, such as Purvis Bearing Service in Austin.

2.3.1 DYNOMAX Software

Land and Sea sells software specifically for use with the DYNOmite water brake. The software allows the user more control over the dyno than allowed by the LCD test computer and also has a Data Acquisition (DAQ) function. An RS-232 cable can be used to connect the PC’s serial port to the Land and Sea test computer. The DYNOMAX interface is shown in Figure 2.5 [29].

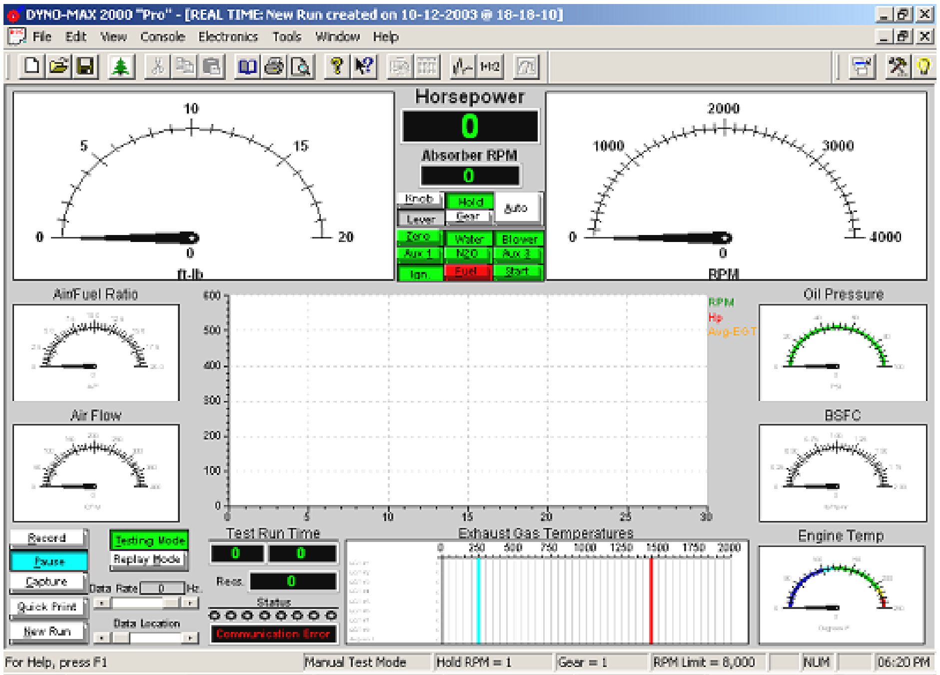

Figure 2.5: DYNOMAX Console Screen [29]

The console reads engine speed, torque, and horsepower. The software can be used to hold the engine’s RPM steady while the load is varied with the dyno. In this mode, the engine is accelerated from idle, and when it reaches the test speed, the dyno begins to apply more torque to hold the engine steady. DYNOMAX used a Proportional, Integral, and Derivative (PID) system to hold the engine speed constant. DYNOMAX 2000 also has provisions for data collection and recording. The user can specify the channels to be recorded and can control the duration of data collection. The recorded data from the previous 30 seconds is shown in a continuously rolling form in the center of the console screen. This allows the user to get a visual idea of the current values and the overall steadiness of the experimental data [29].

2.4 Exhaust Test Setup

An opacity meter was constructed to compare its output with that of the electronic sensor. The opacity meter consisted of a 75 W halogen lamp and a Thorlabs photodiode (DET 110). Purge air was supplied to keep the optics clean. The data were recorded by a Netdaq Fluke data acquisition system at intervals of 5 ms, and with a Measurement Computing PMD DAQ module, which allowed for variable sampling rates. The fastest allowable sampling rate was 20 micro-seconds. The FLUKE data acquisition system came with its own software while the Measurement Computing DAQ module was controlled using LABVIEW.

A 70 mm-diameter filter holder was available for particulate sampling from a previous University of Texas project. A vacuum pump was used to draw an iso-kinetic exhaust sample for the filter measurements. F&J Specialty Inc. model 200B70 filters were used to collect the gravimetric samples. A high voltage DC supply provided the bias voltage to the sensor. A +/- 15 V power supply provided power to the current to voltage converter circuit connected to one of the sensor electrodes and to the signal conditioning electronics. The sensor and its associated electronics are discussed in detail in the next chapter. A schematic of the experimental set-up is shown in Figure 2.6. Pictures of the exhaust setup are shown in Figure 2.7 and Figure 2.8.

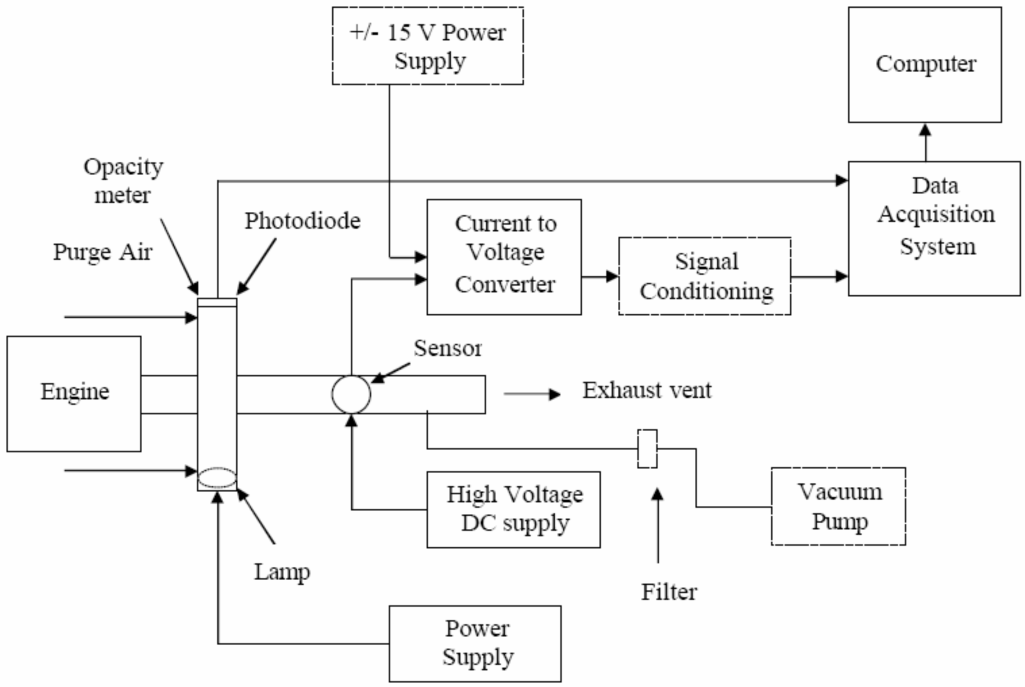

Figure 2.6: Schematic of the experimental set up [30]

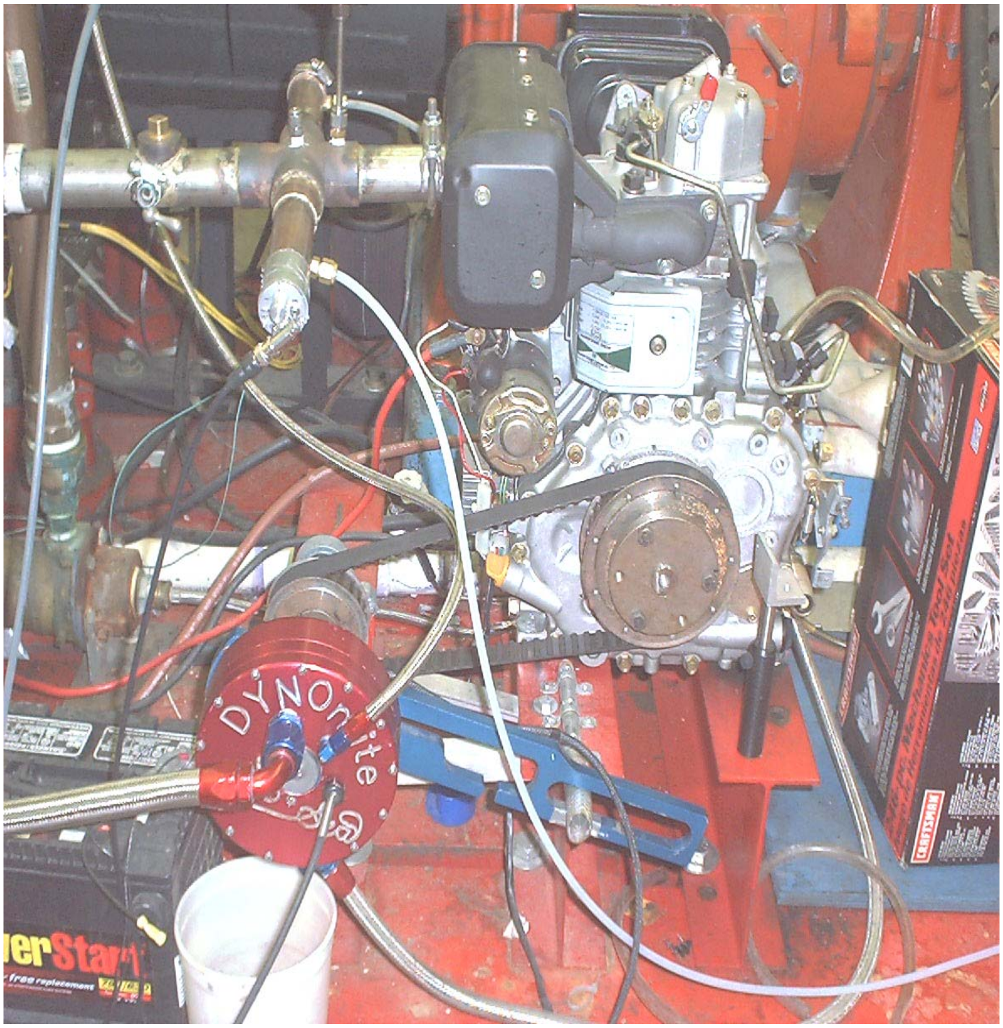

Figure 2.7: Picture of the engine and dyno setup [29]

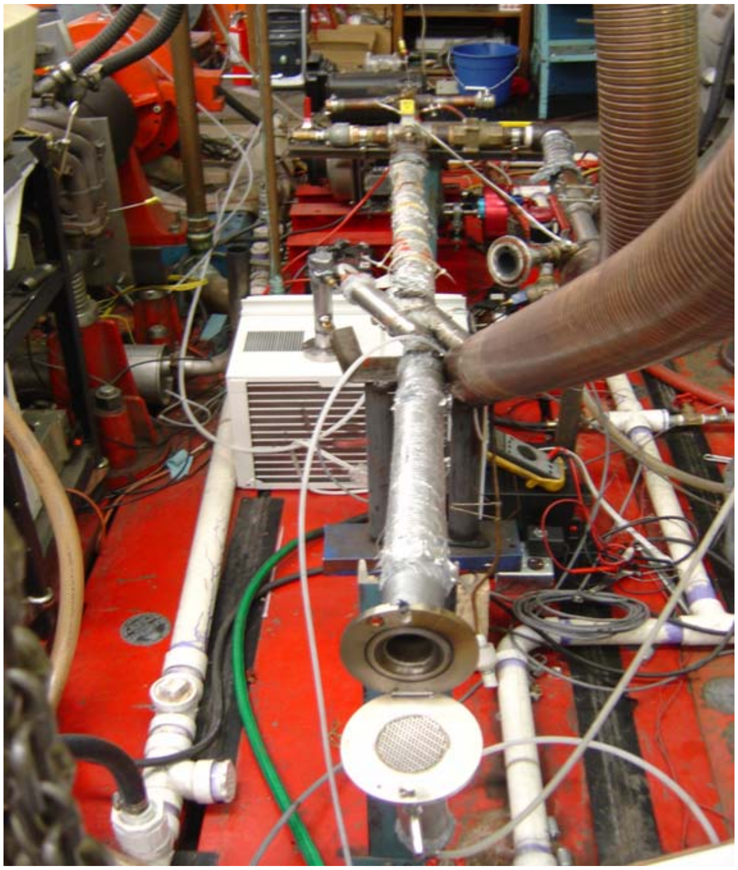

Figure 2.8: Picture of the exhaust setup [31]

At the end of each day of testing the filter papers were heated on electrical hot plates for 24 hours to evaporate water and soluble organic fractions (SOF). The filters were weighed on a Sartorius Research enclosed microbalance to a resolution of 0.1 mg. The hot plates and the microbalance are shown in Figure 2.9.

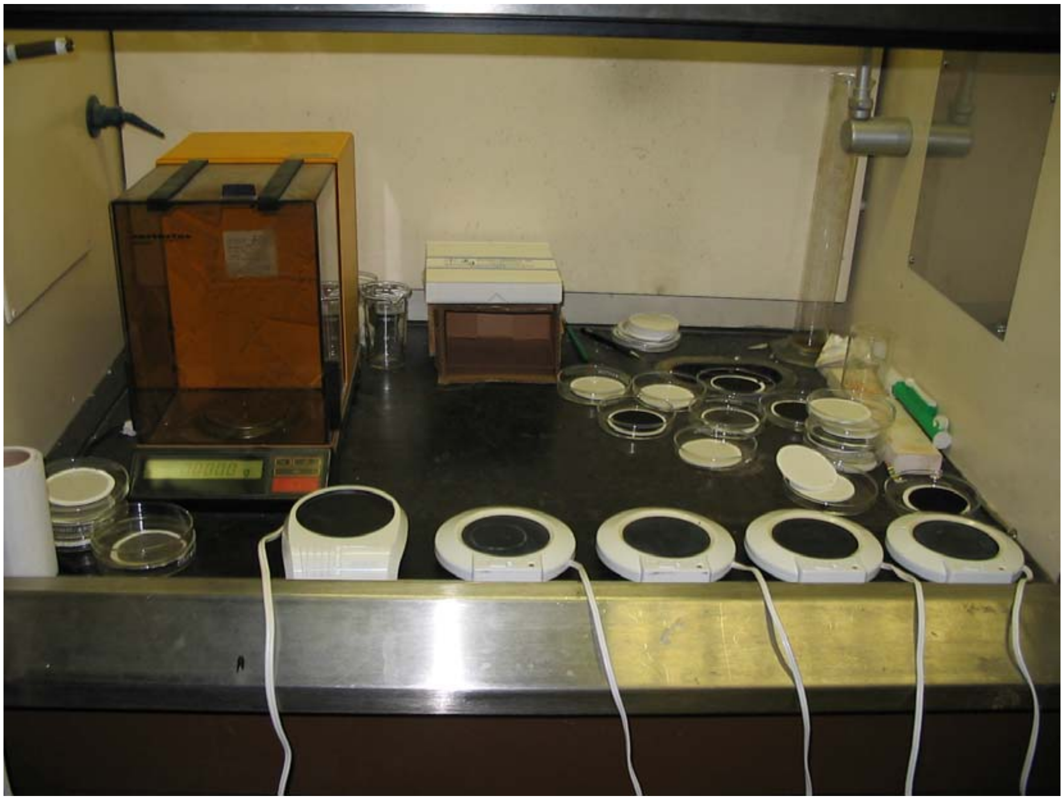

Figure 2.9: Microbalance and electrical hot plates

To vary the bulk flow velocity across the sensor electrodes, two PVC pipes having inside diameters of 2 and 3 inches were used in addition to the stock exhaust of 1.5 inch diameter. Holes were drilled in the pipes to mount up to two sensors simultaneously.

A Fairchild Semiconductor phototransistor optical interrupter switch was installed to correlate the sensor signal with the crank angle position. A small piece of metal shim stock was attached to the pulley, connected to the engine crankshaft, at approximately top dead center (TDC) of exhaust. A +/- 5 V power supply provided power to the optical switch. The output signal of the switch was recorded with the data acquisition system.

2.5 Nephelometer

The sensor output was compared to a nephelometer for steady-state tests in engine exhaust. The nephelometer system was developed here at the University of Texas by Mehta and co-workers [2]. Figure 2.10 shows the main housing of the nephelometer.

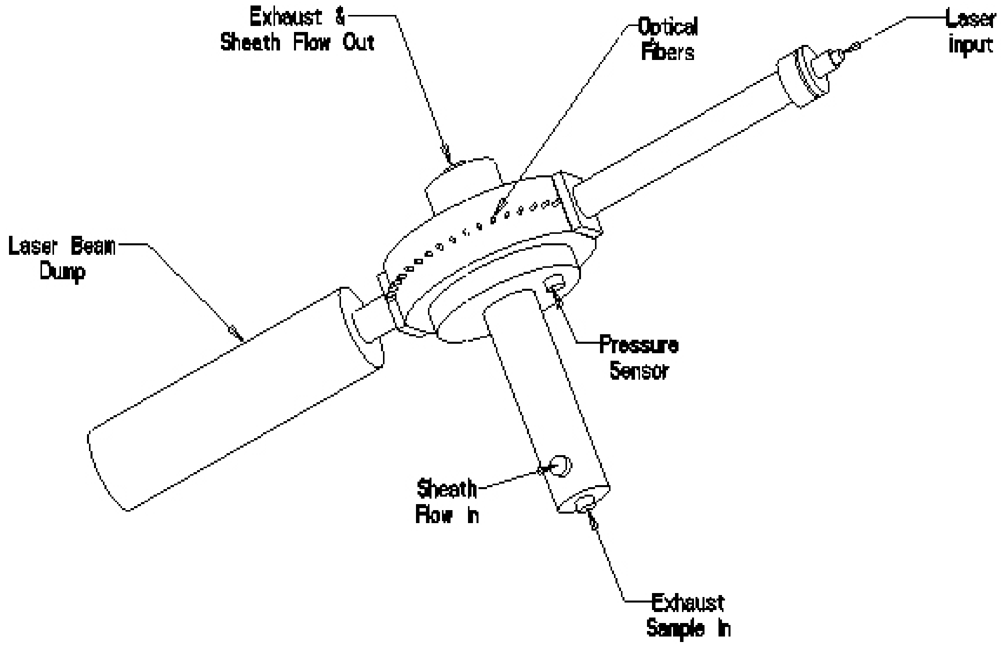

Figure 2.10: Nephelometer main housing [2]

An exhaust sample is drawn into the housing through a small tube located at the housing base and flows along the vertical axis and then exits through the top of the housing. A sheath co-flow is introduced near the base to ensure that the exhaust sample remains along the centerline axis and does not soil the optics. A 500 mW, 1064 nm infrared laser beam is routed from a remotely located diode laser to the main housing through an optical fiber. The laser beam then travels along the horizontal axis of the housing and interacts with the particle flow before finally terminating into a laser beam dump with an integral power monitor. Optical fibers with focusing lenses are positioned around the main housing in a single plane at 36 discrete angles ranging from 20° to 160° from the forward scattering direction in 4° increments and are used to carry the scattered radiation to a remotely located 16-bit CCD camera for measurement. The camera exposure time is about 450 msec and an exposure is taken every 2 seconds [6].

The measured angular scattering patterns are then compared to a database of theoretical scattering patterns based on Mie theory. The angular scattering patterns in the database were created from both a Mie scattering computer program and a separate Distribution Enhancement program. Both programs were written for use with MathCad software [2]. The Mie program calculated two polarization-dependent scattering intensity functions for a spherical particle based upon the wavelength of the incident radiation, the refractive index of the particle and the scattering medium, and the particle diameter. The two polarized scattering intensity functions were averaged to produce one simulated unpolarized scattering pattern since the actual infrared radiation from the laser was unpolarized. Theoretical scattering patterns for distributions of particle sizes were created using custom software that assembled the necessary single-sized unpolarized scattering patterns for a given distribution and weighted the contribution of scattering at each angle for a given particle size in the distribution by its corresponding fraction in the distribution. Researchers investigating particulate emissions from diesel engines have commonly reported log-normally distributed systems of particles, therefore the database of theoretical scattering patterns was created using log-normally distributed particle systems [32]. Mean diameters ranging from 50 nm to 2000 nm in 50-nm increments and logarithmic deviations ranging from 0.05 to 0.25 in 0.05 increments were considered. The refractive index used for generating the theoretical scattering patterns was 1.60-0.6*i*, a common value reported for soot [33]. The Mie scattering patterns are shown in Figure 2.11.

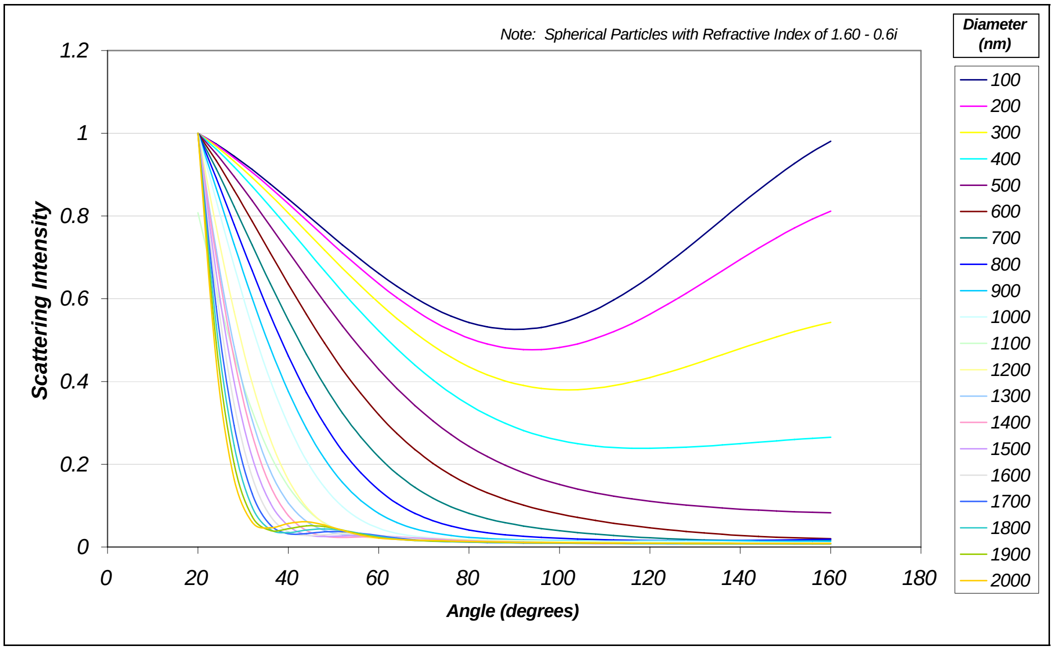

Figure 2.11: Theoretical Mie scattering patterns [2]

A separate Microsoft Excel macro, written in Visual Basic by Mehta and co-workers [2], was used to compare the measured scattering patterns to the database of theoretical scattering patterns and select the best-fit distribution. The best-fit distribution was defined as the theoretical distribution that produces the lowest sum of differences between measured and theoretical scattering intensity data for the set of angles between 20 degrees and 100 degrees from the forward scattering direction. Backscattering angles were not used because of uncertainties associated with the weak scattering at these angles.

The nephelometer uses unpolarized scattering information at 90° from the forward scattering direction to determine PM mass loading in real time. Scattering intensity at 90° is believed to be proportional to the cube of the diameter of the particle, and hence for spherical particles in a flow, proportional to the mass concentration of particles. Using a PM-laden exhaust sample from a steady state acetylene diffusion flame, 90° scattering measurements from the nephelometer were correlated to gravimetric filter measurements to produce an absolute calibration curve. Exhaust samples with increasing levels of PM were passed through the sample chamber and then through filters to generate the calibration curve. The slope of the calibration curve is used to scale subsequent 90-degree scattering data from an engine to obtain PM mass loading in real time [32]. The calibration curve is shown in Figure 2.12.

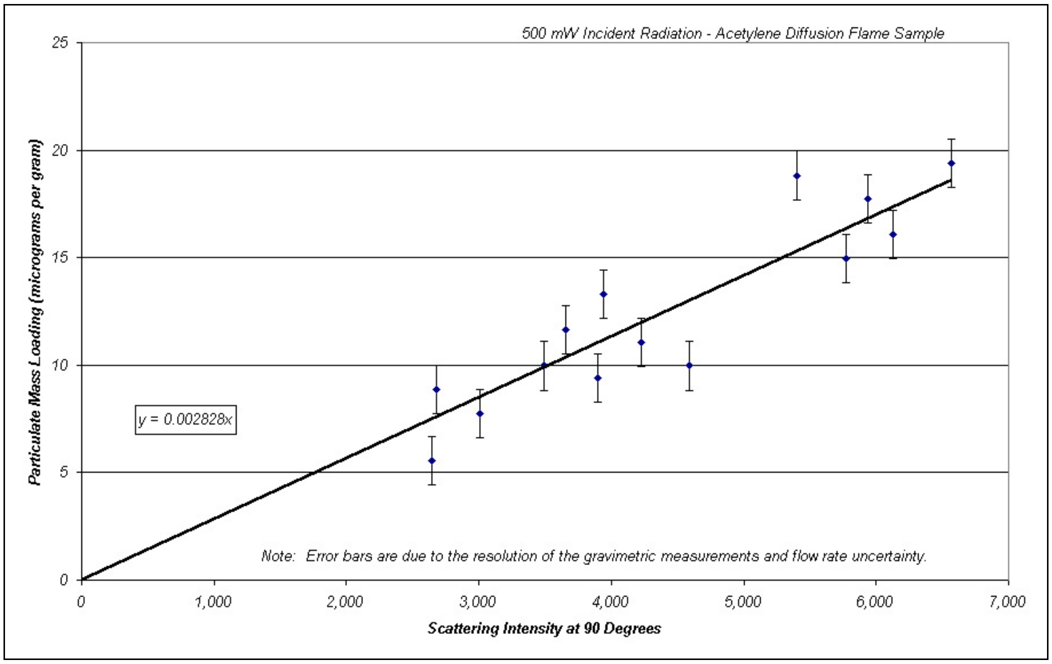

Figure 2.12: Mass loading correlation [32]

A 3/8 inch stainless tube was used to draw a sample from the main exhaust. This sampling line was connected to a 3/16 inch tube at the base of the main housing of the nepehlometer. A small KNF-brand vacuum pump drew the exhaust sample through the chamber and then through a Wyatt Technologies mass flow controller. A sheath flow of air was pumped into the annulus formed by the outer wall of the small exhaust tube and the inner wall of the surrounding housing. Both the exhaust and sheath flows exited the sample chamber from the top [6].

2.6 Aerodynamic Particle Sizer

A TSI Model 3320 Aerodynamic Particle Sizer (APS) shown in Figure 2.13 provided an additional instrument to make a qualitative comparison with the sensor output.

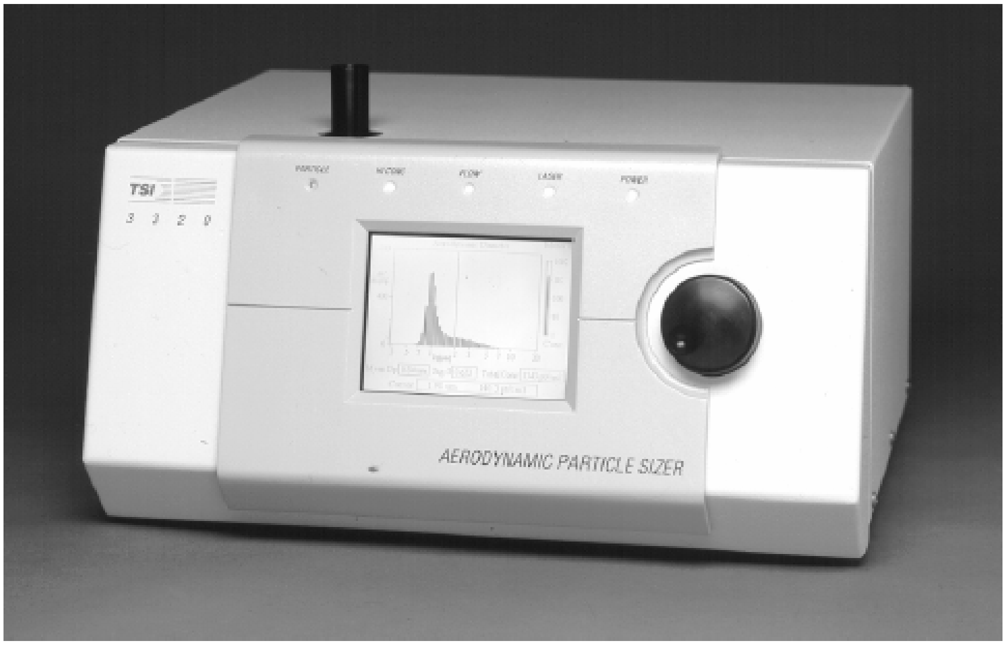

Figure 2.13: Aerodynamic Particle Sizer [34]

The APS uses the principle of inertia i.e. large particles with higher inertia accelerate less than small particles, to separate particles of different sizes by measuring their time-of-flight as they are accelerated across two laser beams [35]. The time-of-flight data is converted to aerodynamic diameter through an internal function derived from a calibration with particles of known diameter. The APS is capable of counting and sizing particles with aerodynamic diameters in the range of 0.5 to 20 μm. The APS can accurately measure aerosol concentrations less than 1000 particles/cm^3. For high concentrations a dilution system is necessary. For all the engine tests a TSI Model 3302A diluter of dilution ratio 100:1 was used. It worked by cleaning 99% of the sample flow and recombined the clean air with the separated 1% of the sample. To clean the sample the diluter first removed large particles by impaction and then removed the remaining particles with a series of HEPA filters. Two pressure gauges could be used to control the flow-rates and identify leaks or clogs in the system. The diluter was placed on top of the APS unit as shown in Figure 2.14 [35]. A 3/8 inch stainless tube was used to draw a sample from the main exhaust line. The sample was passed through a cold trap to condense out the water vapor in the exhaust and to cool the gas entering the diluter to less than 40 °C. An internal pump in the APS drew the sample through the diluter into the particle counter.

Figure 2.14: Aerodynamic Particle Sizer with the Diluter on top [36]

Chapter 3: Sensor Design and Development

Throughout the research reported in this dissertation the sensor design underwent several changes. These changes came about as experience using the sensor in the engine exposed weaknesses and areas of potential improvement. This chapter describes the key components of the electronic sensor and several tests that were conducted to investigate extraneous mechanisms that could contribute to the measured signal. Various techniques and sensor designs investigated to minimize sensor fouling are also discussed.

3.1 Sensor Design

The sensor is approximately the size of a standard automotive spark plug or oxygen sensor. It consists of a pair of closely spaced electrically isolated electrodes that protrude into the exhaust flow. One electrode is given a high D.C. voltage bias of 1000 V while the other electrode is connected to a custom built current to voltage converter circuit. The output of the current to voltage converter is passed through further signal conditioning, which is discussed later in this chapter, and is then recorded by a PC based A/D data acquisition system.

This sensor makes use of the finite electrical conductivity of the carbonaceous fraction of the PM in the exhaust stream. The general mechanism governing sensor behavior is the formation of an electrically conductive channel between the two electrodes of the sensor, by the carbonaceous PM in the exhaust, thereby enabling a current flow. The carbonaceous PM in the exhaust thus acts like a resistance between the two electrodes. The magnitude of the current (I) derived from the sensor is in the range of $10^{-8} – 10^{-9}$ A. This idea for the PM sensor originated at the University of Texas and has been patented. The concept was successfully tested with a few prototypes in the exhaust of a steady-state acetylene diffusion flame in a previous project [5]. The sensor has many attributes that would make it attractive for production vehicle applications. These include: sensitivity, low cost, simplicity, and ease of implementation. A schematic of the sensor system is shown in Figure 3.1.

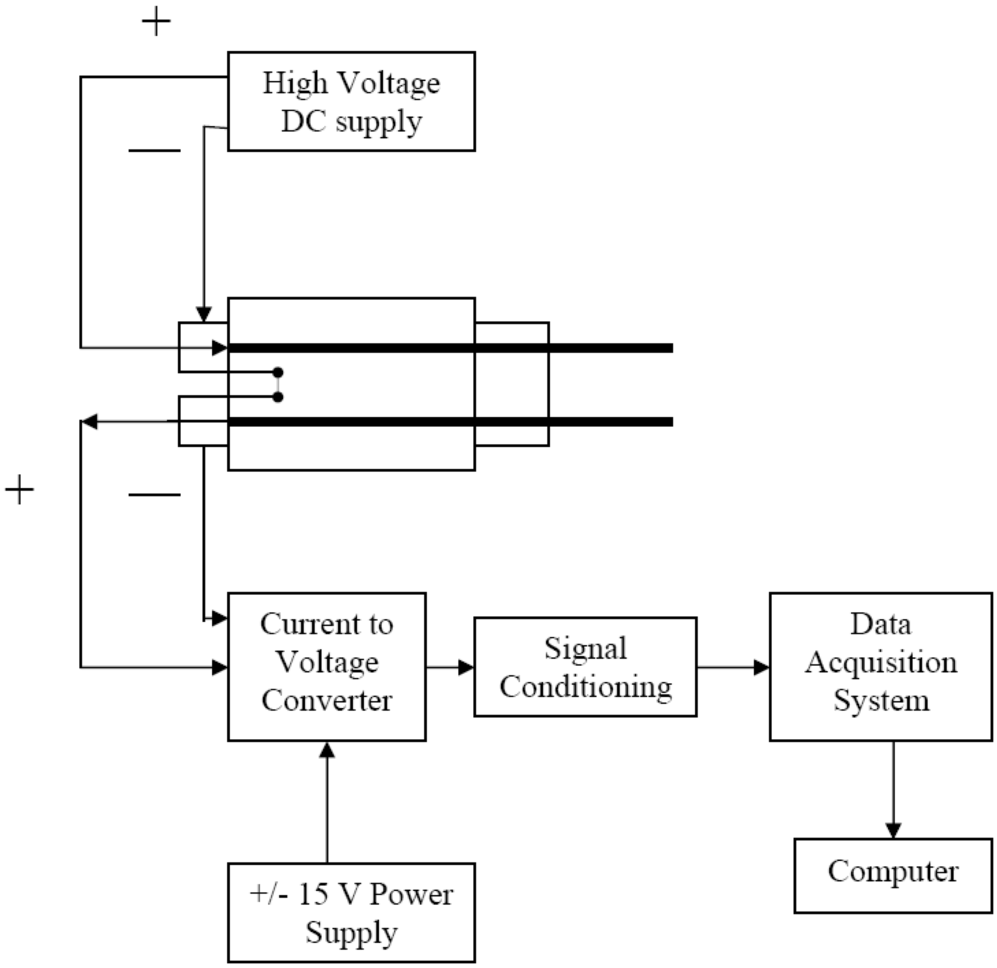

Figure 3.1: Schematic of the sensor system

3.1.1 Sensor Construction

The sensor electrodes were constructed by soldering two copper wires to two separate BNC connectors. A teflon tube was slid over each electrode after the wires were soldered to the BNC connector. Next, a copper tube was slid over the teflon tubing. This was done to ensure complete electrical isolation of the two electrodes. It was necessary to completely isolate the electrodes from the cold weld used to make the sensor body. Cold weld is not a perfect insulator and has some electrical conductivity. If the electrodes were not completely isolated, it provided an electrical path from the electrode to which the voltage bias was applied to the detector electrode. The next step was to give the sensor a common ground. A ground copper strap was soldered from each copper tube to its respective BNC connector and a strap was soldered between the two copper tubes. A mold was made out of a plastic 35mm film canister. The canister was cut in half lengthwise, creating a half cylinder. A 1/2” NPT pipe thread fitting was placed at one end of the canister. The two electrodes were laid across the body of the canister. The canister mold was filled with cold weld and allowed to cure. The electrodes extended well past the cold weld and the pipe fitting. A construction schematic of the sensor is shown in Figure 3.2. A photograph of a typical sensor is shown in Figure 3.3.

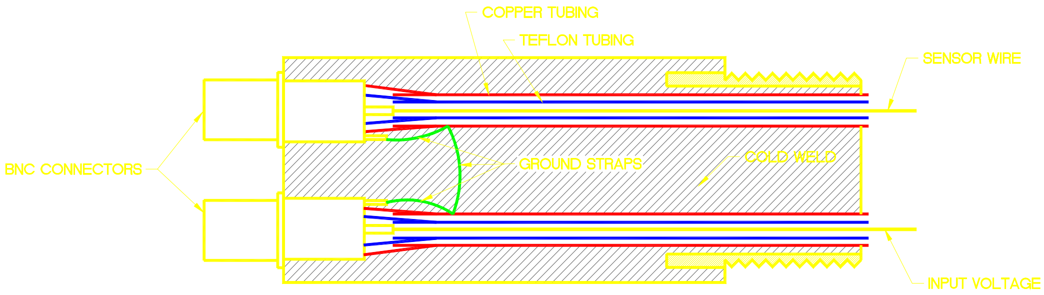

Figure 3.2: Construction schematic of the sensor [5]

Figure 3.3: Photograph of a typical sensor

3.1.2 Sensor Electronics

The output of the sensor was connected to either a custom built current to voltage converter or to a custom made charge amplifier circuit. The sensor could not be operated with a commercial charge amplifier and a current amplifier. The current to voltage converter consisted of a Burr-Brown op-amp (either part # OPA111AM-ND or OPA128JM-ND) and three resistors. The connection diagram of the op-amp is shown in Figure 3.4 while the current to voltage converter circuit is shown in Figure 3.5. The circuit was constructed on a small protoboard and was placed inside a metal box for isolation. A +/- 15 V power supply provided power to the circuit.

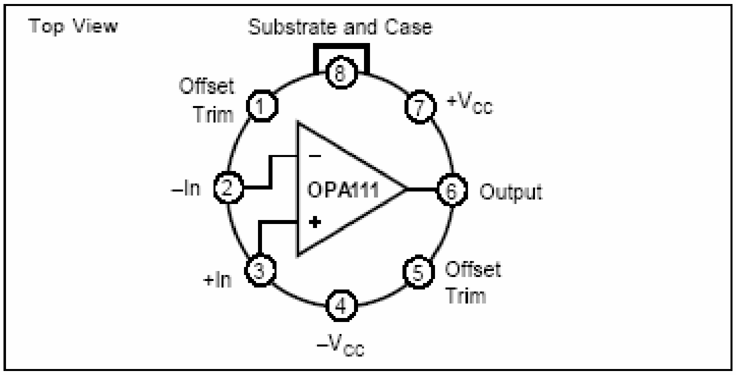

Figure 3.4: Op-amp connection diagram [37]

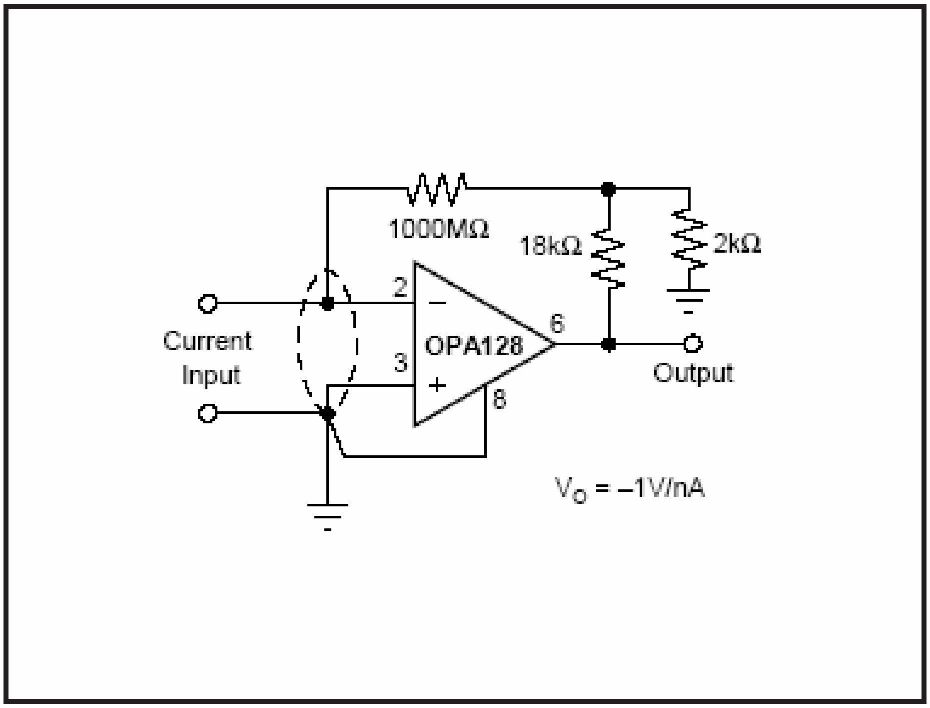

Figure 3.5: Current to voltage converter circuit [38]

The charge amplifier circuit consisted of the op-amp (OPA111AM-ND or OPA128JM-ND), two resistors, and two capacitors. A schematic of the charge amplifier circuit is shown in Figure 3.6 along with the values for the resistors and capacitors. The circuit was constructed on a small protoboard and was placed inside a metal box for isolation. A +/- 15 V power supply provided power to the circuit.

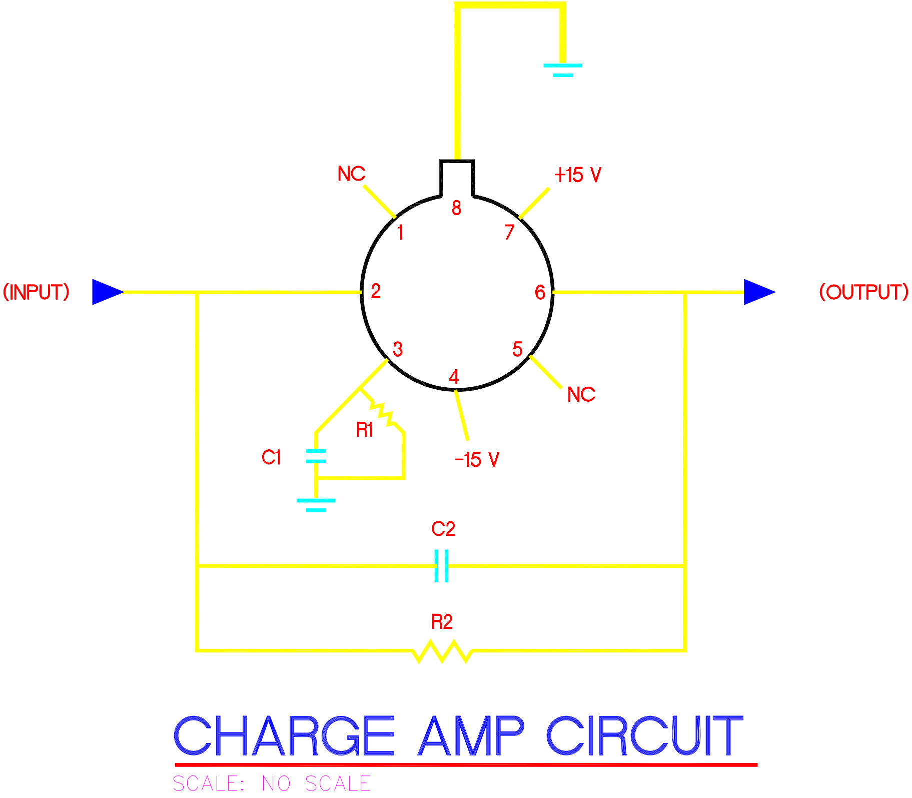

R1 = 1000 MΩ, R2 = 1000 MΩ, C1= 271 pf, C2 = 12 pf

Figure 3.6: Charge amplifier schematic [5]

3.1.3 Signal Conditioning

Initially the output of the current to voltage converter and the charge amplifier was connected directly to the data acquisition system. Figure 3.7 shows the output of the sensor, when connected to the current to voltage converter, for an engine start followed by two engine accelerations (revs). Figure 3.8 shows the output of the sensor for an engine start followed by two accelerations when the sensor is connected to the charge amplifier circuit. The sensor could detect the increase in soot concentration during engine start and accelerations but there was a lot of noise in the sensor signal.

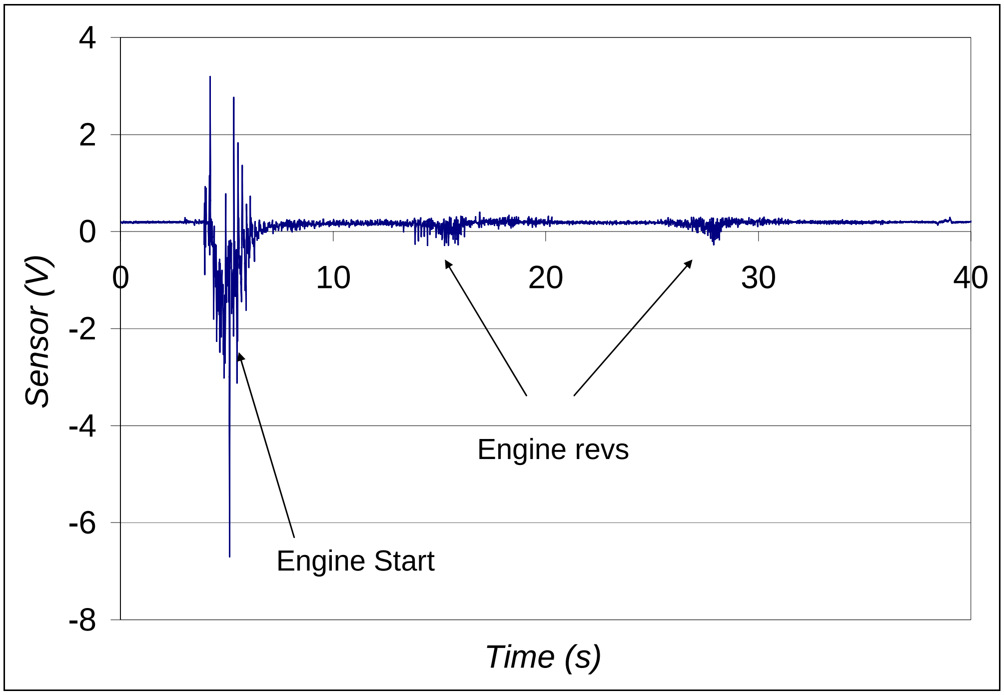

Figure 3.7: Sensor output for an engine start and two revs (current to voltage converter)

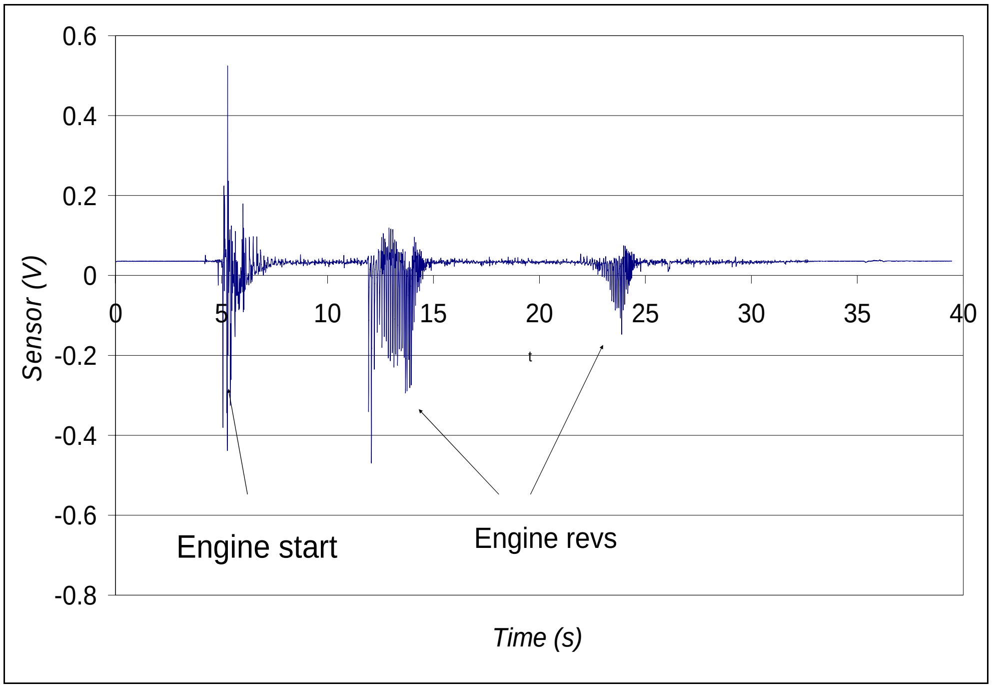

Figure 3.8: Sensor output for an engine start and two revs (charge amplifier)

Also the sensor signal, instead of being a continuous smooth curve, was comprised of discrete peaks or spikes. Figure 3.9 shows the sensor output for an engine acceleration ('rev') on an expanded time scale. The discrete spikes in the signal are clearly visible. These spikes were not noise but response of the sensor to fluctuations in PM concentration.

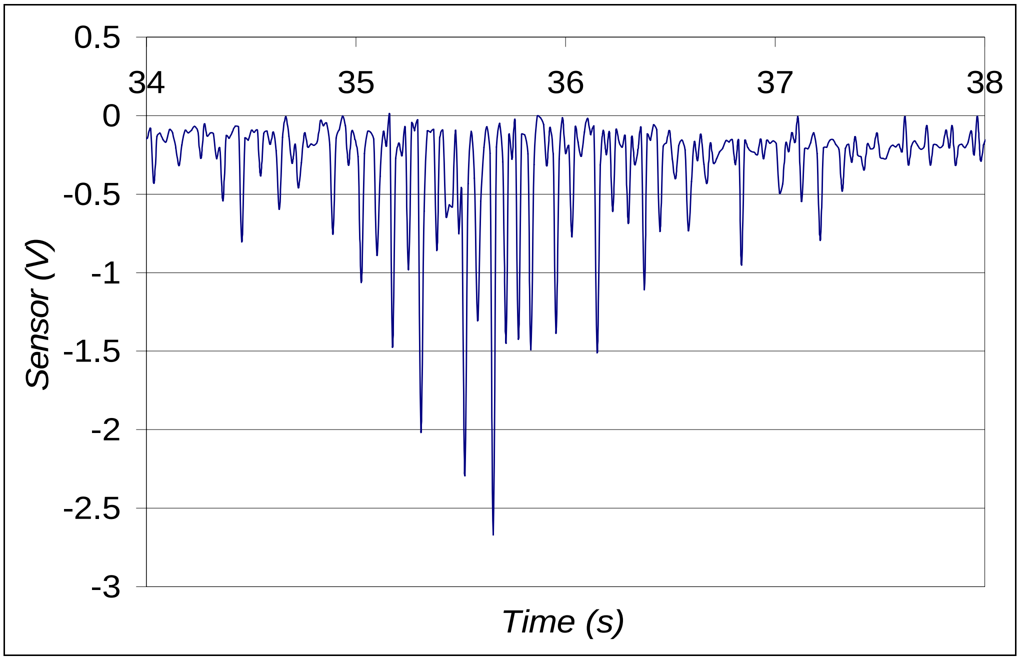

Figure 3.9: Sensor output for an engine rev

To minimize the noise in the sensor signal and eliminate its discrete nature a voltage follower and a low pass filter were added to the sensor system. The voltage follower had an op-amp with unity gain (gain = 1). This configuration is commonly referred to as a unity gain buffer, and it decreases the impedance of the source connected to the DAQ device. A power supply was used to provide +/- 15 V to the voltage follower. The voltage follower circuit is shown in Figure 3.10. The output of the current to voltage converter or the charge amplifier was the input to the voltage follower. The output of the voltage follower was passed through a low pass filter before it was recorded by the data acquisition system.

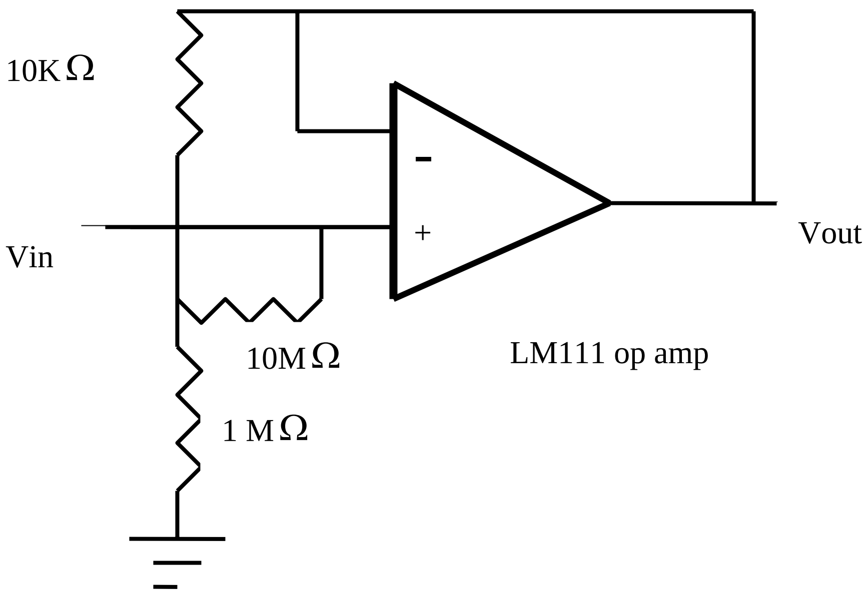

Figure 3.10: Voltage follower circuit

The low pass filter had the following relation

$$Cut \cdot off \cdot frequency = \frac{1}{2\pi RC} \qquad (3.1)$$

A 1000Ω resistor and capacitors of 1 μF, 2.2 μF and 6.8 μF were tested. The 1000Ω resistor and the 6.8 μF capacitor gave the best signal to noise ratio. The low pass filter thus had a cut off frequency of about 23 Hz. The low pass filter circuit is shown in Figure 3.11.

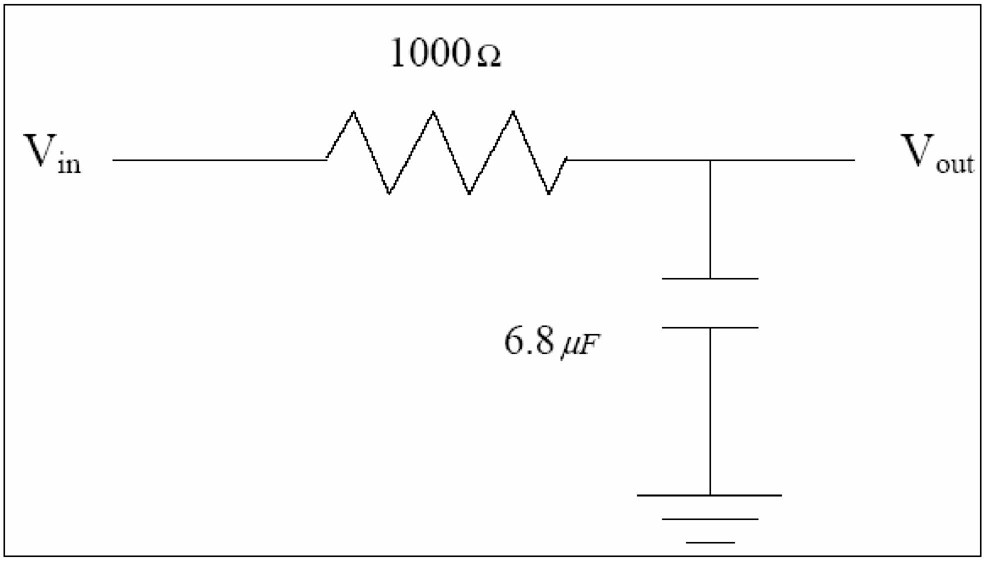

Figure 3.11: Low pass filter circuit

Figure 3.12 shows the output of the same sensor, as in Figure 3.7, for an engine start followed by two accelerations with the voltage follower and the low pass filter included in the sensor system. The noise in the sensor signal was minimized and the signal to noise ratio was improved dramatically with the addition of the voltage follower and the low pass filter to the system. The output voltage range of the soot sensor was determined by the voltage follower and the low pass filter (±12 volts).

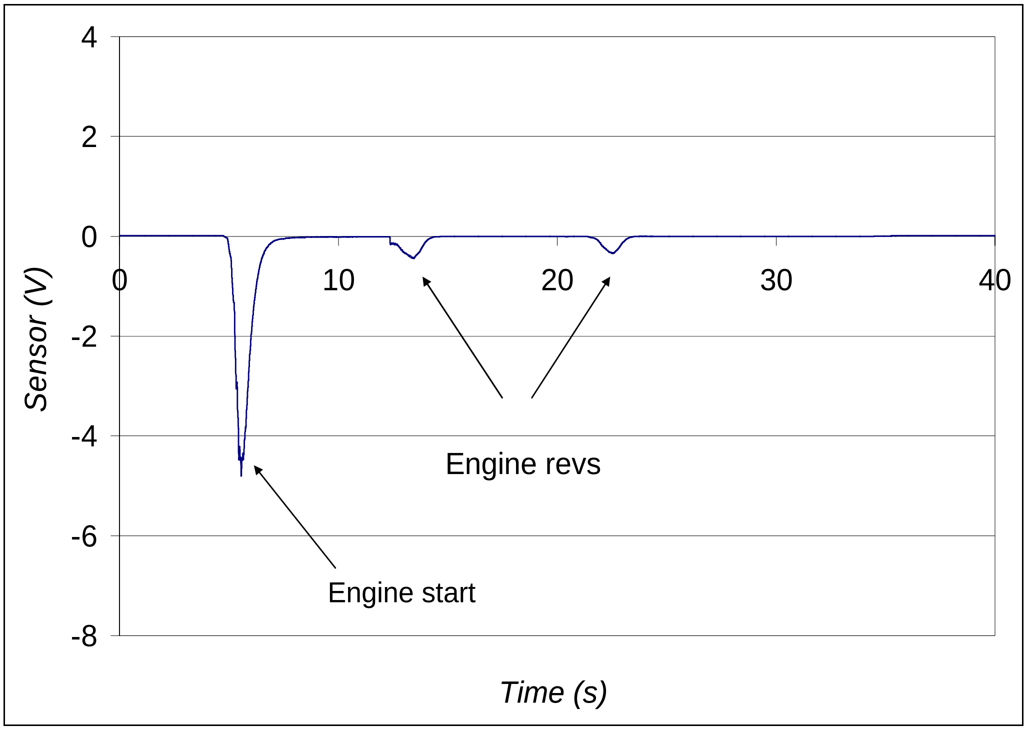

Figure 3.12: Sensor output for an engine start and two revs with a voltage follower and a low pass filter

Figure 3.13 shows the sensor output for an engine 'rev' on an expanded time scale. The sensor signal was a continuous smooth curve instead of discrete spikes. The sensor could still detect the transient fluctuations in soot concentration.

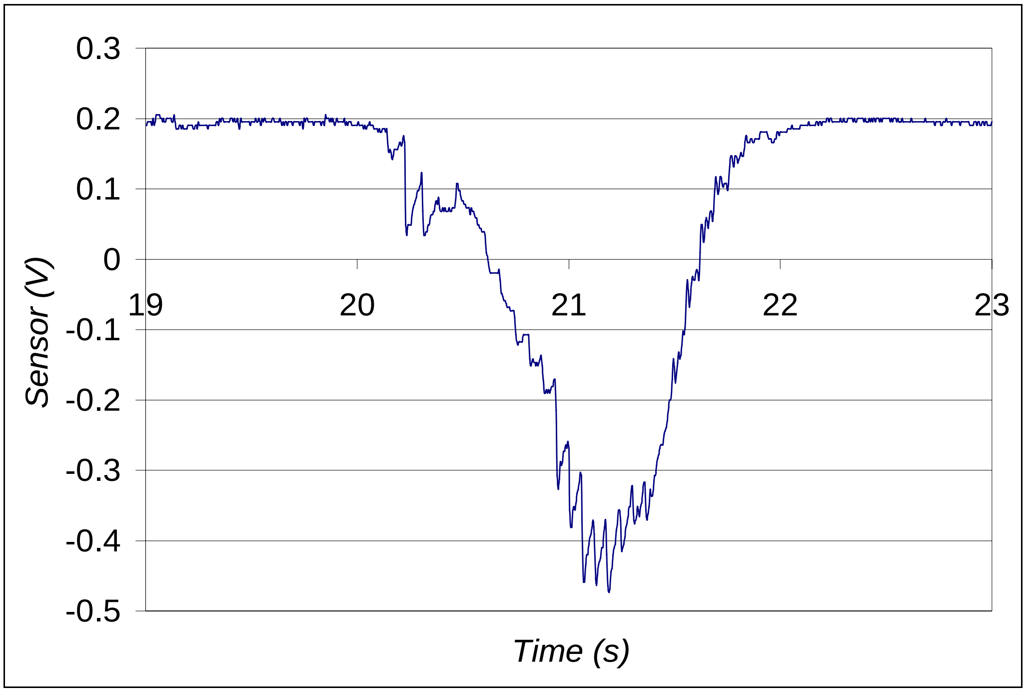

Figure 3.13: Sensor output for an engine rev with a voltage follower and a low pass filter

3.2 Sensitivity to SOF

Several tests were performed to investigate which components of particulate matter the sensor was sensitive to. It was found that the sensor was sensitive to only the carbonaceous fraction of particulate matter and not the soluble organic fractions (SOF) or sulfates, since the electrical conductivity of these components is orders of magnitude lower than the carbonaceous fraction [28]. This was tested by replacing the acetylene flame in the flow tunnel by fumes from oil evaporating on a hot plate. The sensor did not react to the SOF particulates.

The sensor was installed downstream of a filter in the exhaust of the diesel engine. The filter blocks most of the carbonaceous particles in the exhaust but allowed a higher fraction of the SOF through. Figure 3.14 shows the output of the sensor for an engine start followed by three accelerations. The sensor had some reaction to the engine start and accelerations but the signal magnitude was less than 1% of the typical response for normal operation in the exhaust. The sensor is thus primarily sensitive to the carbonaceous fraction of PM and not the SOF or sulfate component.

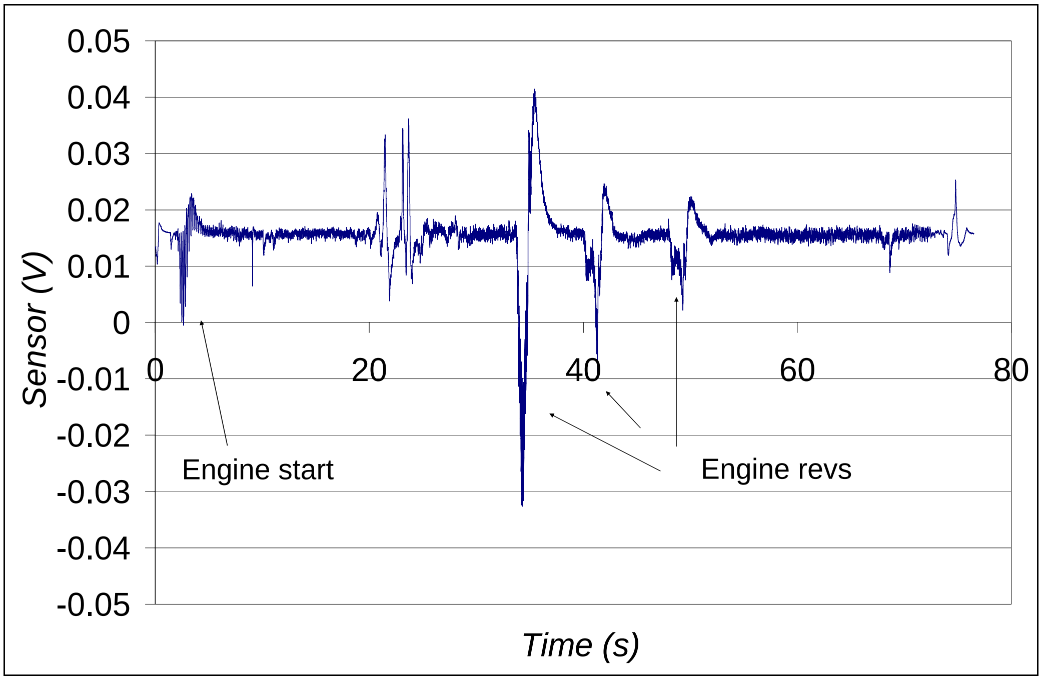

Figure 3.14: Sensor output for an engine start followed by three accelerations when installed downstream of a filter

3.3 Sensitivity to the Natural Charge

Several tests were conducted to investigate extraneous mechanisms that might contribute to the measured signal. The sensor was tested without applying a bias voltage. A typical example of the sensor output for a start-up followed by an acceleration is shown in Figure 3.15. Even without an applied voltage the sensor could detect the engine start and acceleration. This response is believed to be due to the natural charge carried by particles in the exhaust stream as mentioned previously. The signal magnitude, however, is less than 1% of the typical response for normal operation with an applied bias voltage. Therefore, this natural charge on the particles does not contribute significantly to the sensor signal when a bias voltage is applied.

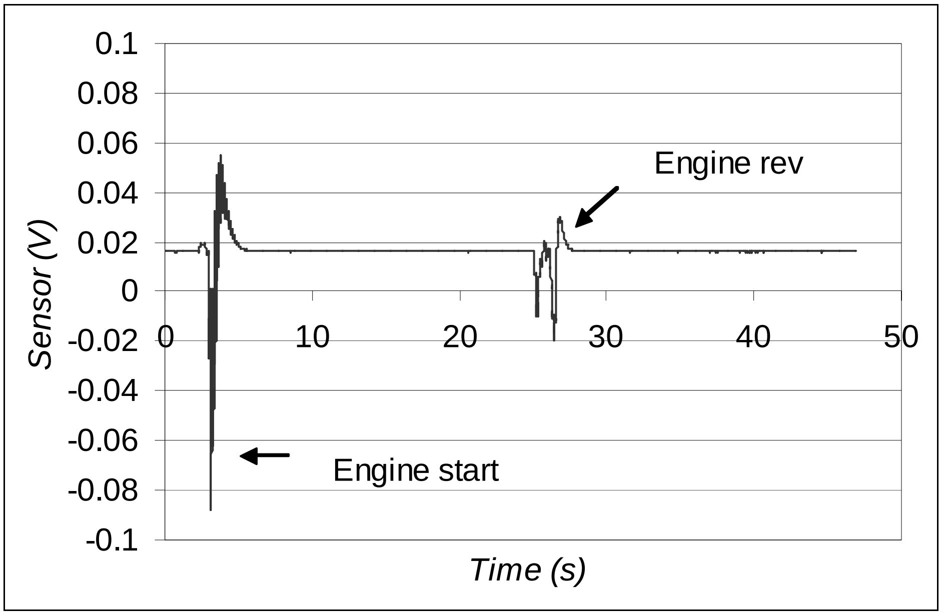

Figure 3.15: Sensor signal with no bias voltage

3.4 Effect of Electrode Orientation

Several tests were done to examine the effect of electrode orientation with respect to exhaust flow on the sensor signal. Different orientations of the two sensor electrodes with respect to the flow were tested in the metal flow tunnel with the acetylene flame and in the exhaust of the diesel engine. Figure 3.16 shows the output of the sensor for two orientations of the electrodes with respect to the exhaust flow. The engine was run at 1250 RPM and a load of 6 lb-ft, which is about 50% of full load. In one orientation the signal electrode was upstream of the electrode to which the voltage bias was applied, while it was downstream in the other. It was observed that electrode orientation did not have a significant effect on the sensor signal. The average difference in the mean sensor signal for the two orientations was 11%. Multiple runs were done on different days to ensure repeatability.

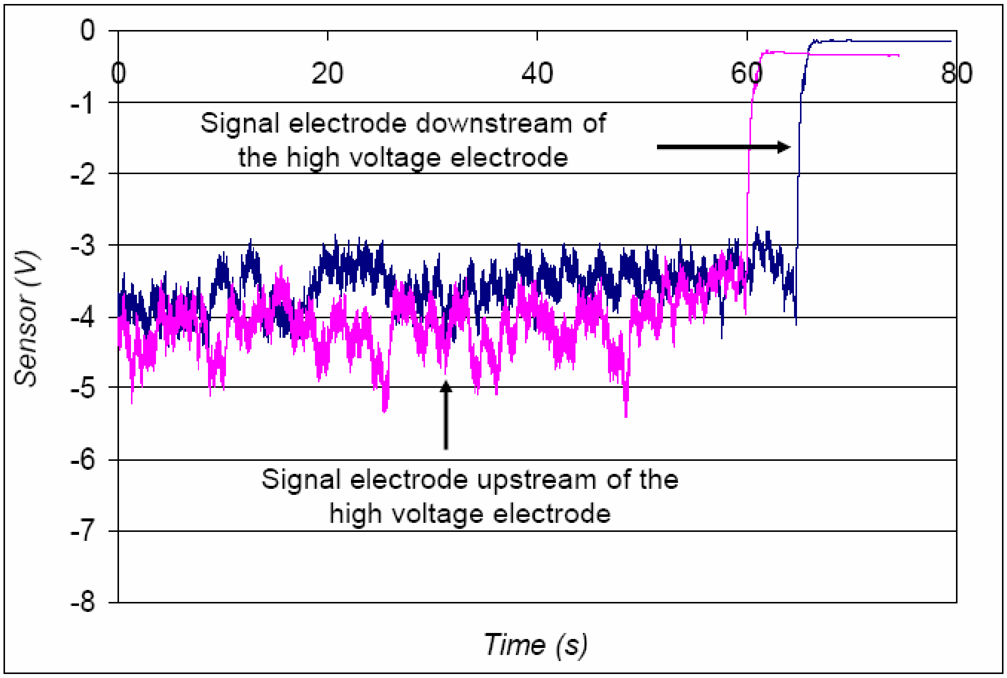

Figure 3.16: Effect of electrode orientation on the sensor signal

Hence, ion transfer between the two electrodes of the sensor was not considered to be a dominant mechanism since the orientation of the sensor with respect to the exhaust flow did not have a significant effect on the sensor signal.

3.5 Effect of Vibration, Flow Pulsation and Exhaust Temperature

To isolate any effects of engine vibration, flow pulsation, and exhaust temperature the sensor was mounted in a PVC pipe supported independently of the main exhaust system. A sample was drawn through this pipe by a vacuum pump at a fixed flow rate. A cold trap was installed upstream of this PVC section to cool the exhaust sample to about ambient temperature. The sensor output was qualitatively the same as when mounted directly in the exhaust as shown in Figure 3.17. Figure 3.17 also shows the output of the opacity meter for an engine start followed by two accelerations. The phase difference between the opacity meter, which was in the main exhaust system, and the sensor can be clearly seen. This phase difference was due to the time taken by the exhaust sample to reach the sensor, which was completely isolated from the engine exhaust setup. The magnitude of the signal was reduced, however, due to dilution and some particle deposition along the sampling line. Thus, the sensor signal, was found to be unaffected by engine vibration, flow pulsation and exhaust temperature effects.

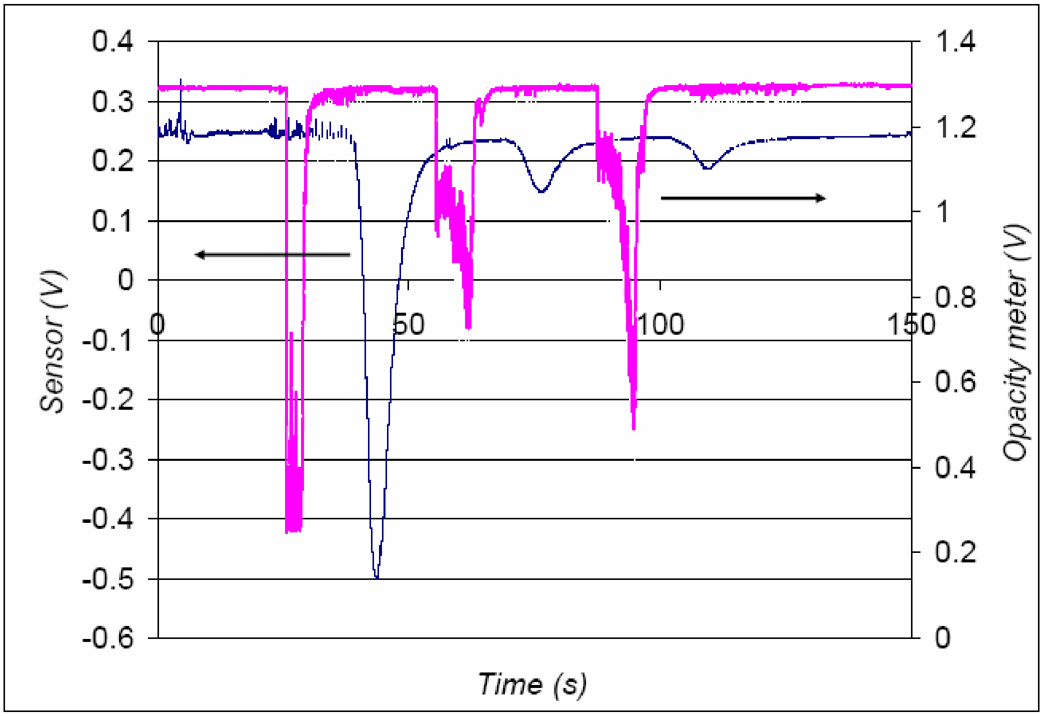

Figure 3.17: Sensor and opacity during engine start-up and revs

3.6 Effect of Asymmetric Electric Field

All the sensor designs tested so far had two electrodes of the same diameter and length. Hence, the electric field between the two electrodes was symmetric. A test was done to examine the effect of an asymmetric electric field on the sensor behavior. A new sensor was constructed with electrodes of the same length but different widths. One electrode was a thin cylindrical wire of diameter 0.6 mm while the other electrode was shaped like a flat plate of width 6.35 mm. The widths of the two electrodes, thus, differed by an order of magnitude. A photograph of the sensor is shown in Figure 3.18.

Figure 3.18: Photograph of sensor with dissimilar electrodes

Figure 3.19 shows the output of the sensor for two different runs at an engine speed of 1250 RPM and 50% of full load. In the first run the high voltage bias was applied to the plate shaped electrode while it was applied to the electrode made of thin copper wire in the second run. The signal magnitude is similar for both runs. Multiple runs were done on different days to ensure repeatability. The average difference in the mean sensor signal for the two orientations was 10%. Thus, an asymmetric electric field did not have a significant effect of the sensor signal.

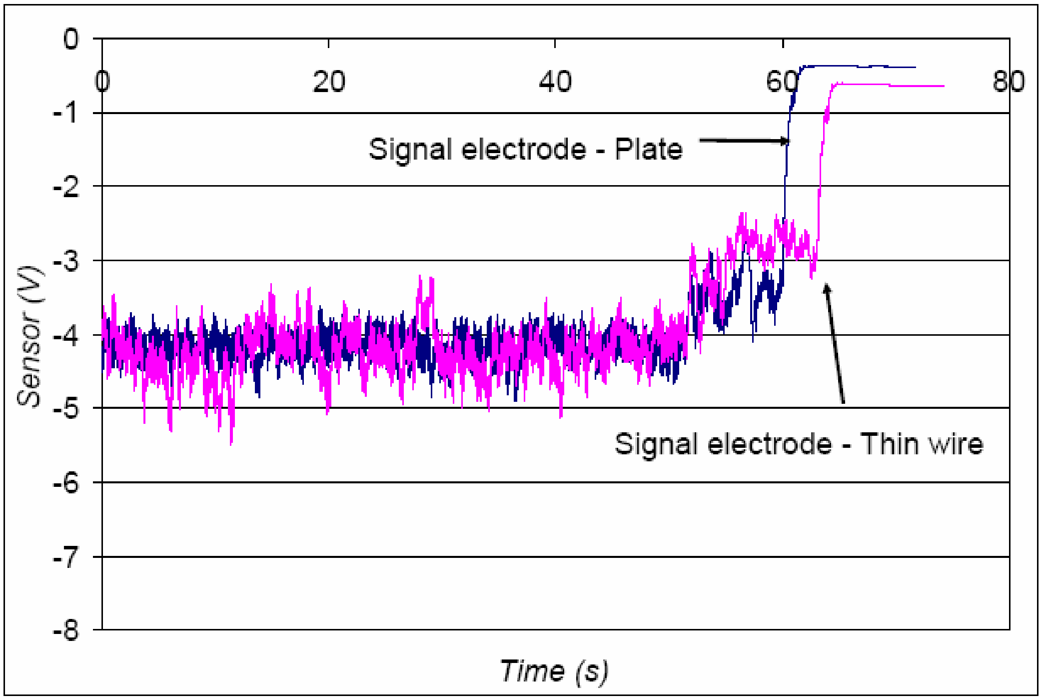

Figure 3.19: Effect of asymmetric electric field

3.7 Sensor Fouling

Several techniques were investigated to prevent or minimize sensor fouling. After multiple runs, without cleaning in between, the sensor baseline drifted towards a negative value, the signal magnitude increased at the same operating condition and the signal became noisy. If the sensor was operated continuously at a fixed engine load the signal drifted in the positive direction after about two minutes of operation as shown in Figure 3.20.

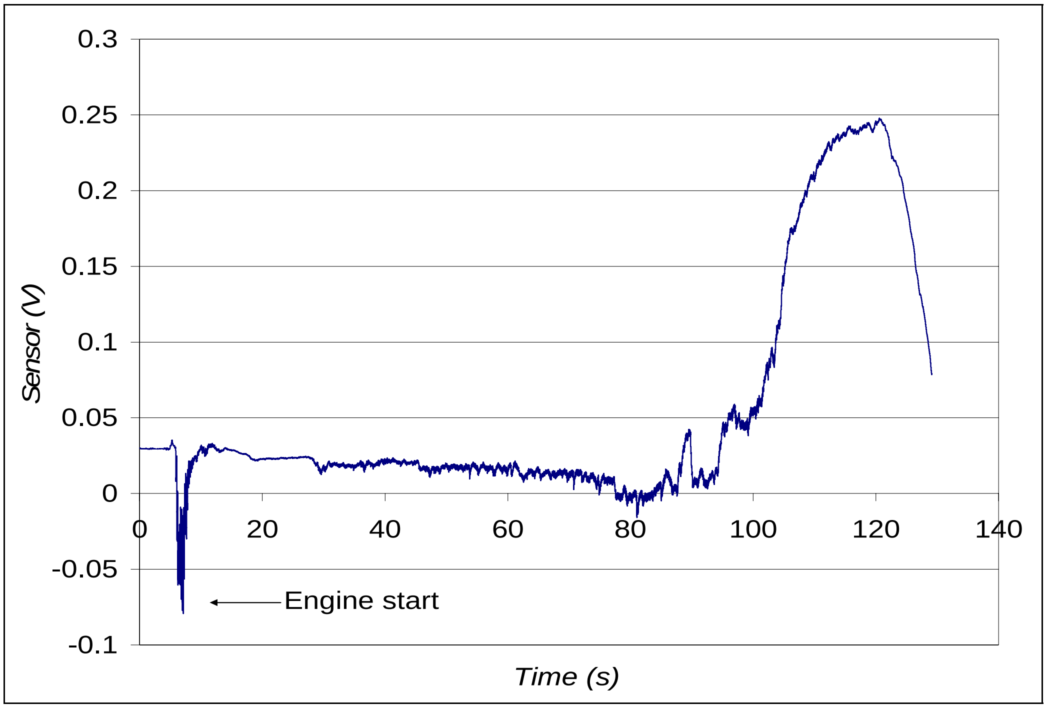

Figure 3.20: Sensor signal for continuous engine operation

Initially compressed air was used to clean the sensor electrodes in between tests. This technique worked well in the metal flow tunnel with the acetylene flame but proved to be ineffective in the engine exhaust. When testing in engine exhaust a thin oily film formed on the electrode surface after multiple runs. Successive engine runs, without cleaning the sensor in between, revealed the presence of particles standing on the electrode surface. A blast of compressed air was able to blow off some of these particles but it didn't get rid of the oily film and the particles sticking to it on the electrode surface. The sensor was cleaned with a brush and a solvent like acetone or gasoline to get rid of this oily film and particles sticking to the electrode surface.

The electrodes were coated with platinum. It was thought that platinum would aid in oxidizing the particles deposited on the electrode surface thereby reducing sensor fouling. The copper electrodes of one sensor were coated with platinum as per the procedure outlined by Koenig and coworkers [39]. A photograph of the sensor is shown in Figure 3.21. It was observed that coating the electrodes with platinum had no effect on sensor fouling. Since the electrodes conducted most of the heat away, the temperature was not high enough for oxidation of the soot particles.

Figure 3.21: Photograph of the sensor with platinum coated electrodes

An enclosure, similar to a lambda sensor, was designed for the two sensor electrodes to minimize sensor fouling. Holes were drilled on two sides of the enclosure to permit cross flow across the electrodes. A photograph of two enclosures is shown in Figure 3.22. The enclosure minimized sensor fouling and allowed continuous operation of the sensor for longer durations of about 7-8 minutes but after multiple runs, without cleaning in between, the sensor baseline still drifted in the negative direction.

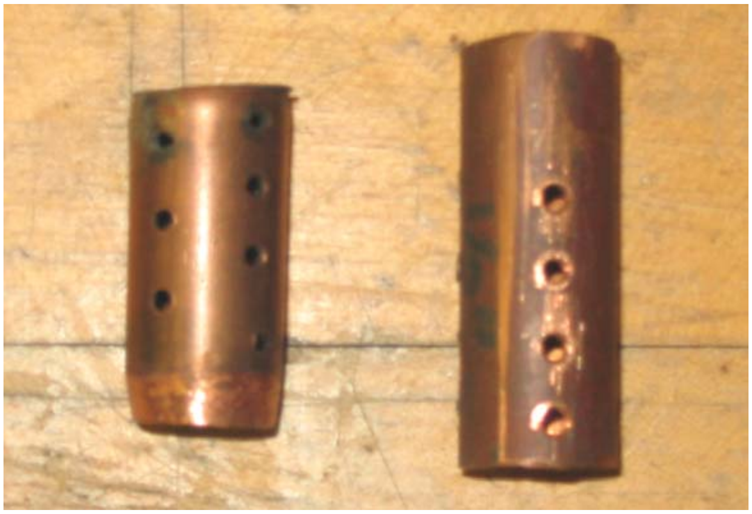

Figure 3.22: Photograph of enclosures for the sensor electrodes

A new sensor design, which incorporated both compressed air and an enclosure, was constructed. The sensor had two electrodes made of copper. The electrodes were shielded from the exhaust flow by an enclosure described above. A 3/16th inch copper tube was included in the sensor body. One end of the tube was connected to a compressed air supply while the open end was located just above the two electrodes in the enclosure. Compressed air was supplied continuously at a very low flow rate. It was thought that a continuous supply of compressed air would minimize deposition of particles on the electrode surface. The flow rate of air was maintained low enough to allow the PM laden exhaust to flow through the enclosure. A photograph of this new sensor design is shown in Figure 3.23. This design too had limited success but did not completely eliminate the effects of electrode fouling like baseline drift in the negative direction after multiple runs and signal drift in the positive direction after continuous operation for a long duration.

Figure 3.23: Photograph of a new sensor design

Finally, a new sensor design was conceived which showed great promise in preventing or minimizing sensor fouling. It was known that to prevent fouling of the electrodes, the electrode surface area exposed to the PM laden exhaust had to be minimized while maintaining good sensitivity and high signal to noise ratio. The new design consisted of insulated copper wires of diameter 2.0 mm i.e. the entire length of the electrode was insulated except for the wire ends. The extension of the signal electrode beyond the cold weld and the fitting was minimized, while the high voltage electrode was bent into a ‘U’ shape so that the un-insulated copper ends of the two electrodes faced each other. Photographs of two sensors based on this new design are shown in Figure 3.24 and Figure 3.25. The spacing between the electrodes could now be adjusted to control the signal magnitude and sensitivity. The insulation along the length of the electrodes prevented the oily film from forming on the electrode surface. As a result the particles stuck to the insulation and not to the electrode surface. Since only the ends of the electrodes were exposed to the exhaust, the deposition of particles on them was drastically reduced. The sensor could now be operated for long durations and multiple runs without cleaning.

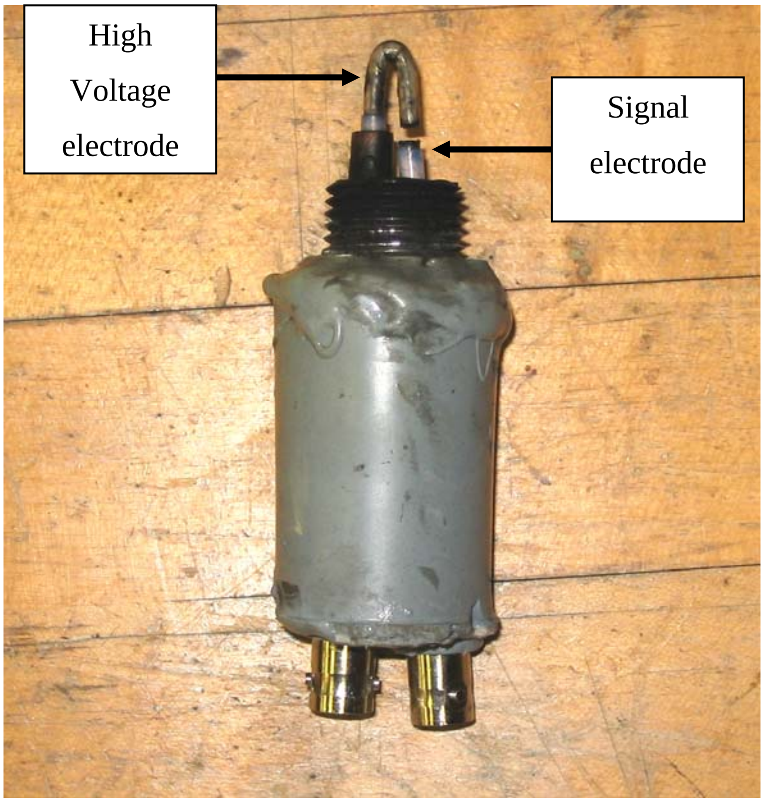

Figure 3.24: Photograph of a new sensor design to minimize sensor fouling

Figure 3.25: Photograph of a sensor designed to minimize sensor fouling

Figure 3.26 shows the output of two sensors for multiple engine starts and continuous operation under medium load (60% of full load) for about 40 minutes. One sensor was connected to the charge amplifier while the other was connected to the current to voltage converter. The engine was allowed to reach a steady idling speed after start-up. The load was then increased to about 60% of full load. After about 10 minutes the engine was shut off for a few seconds. This process was repeated 4 times. The PM emissions from the engine were much greater during the first 5 s of start-up than for either acceleration transients or for steady state operation at any speed/load condition. Even after four engine starts and continuous operation under 60% of full load the signal to noise ratio remained consistent, the signal did not drift in the positive direction and the signal level returned to the initial baseline level once the engine was shut off. This design can be further optimized for on-board operation in a production vehicle.

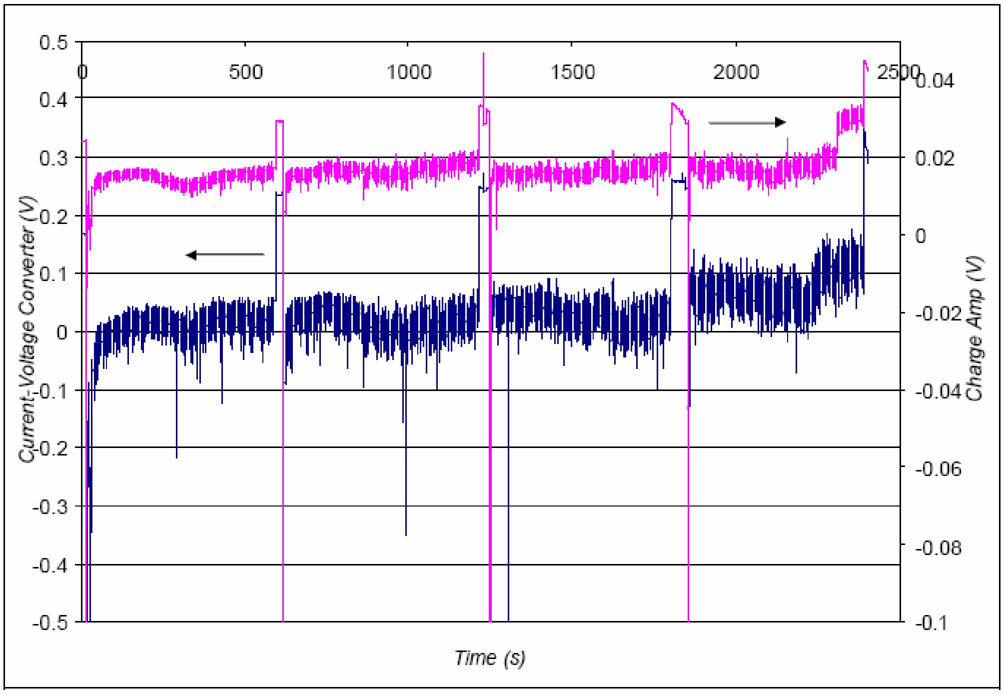

Figure 3.26: Sensor output from two sensors for multiple engine starts and continuous operation at 60% of full load

Figure 3.27 shows the output of the sensor for continuous operation at 60% of full load, after an engine start, for about 40 minutes. There was a shift in the baseline level but the signal magnitude, which is the difference between the baseline and the signal level, remained fairly consistent. This drift in the baseline level was investigated further and is believed to be due to the electronics and not the sensor itself. This issue is discussed in the next sub-section.

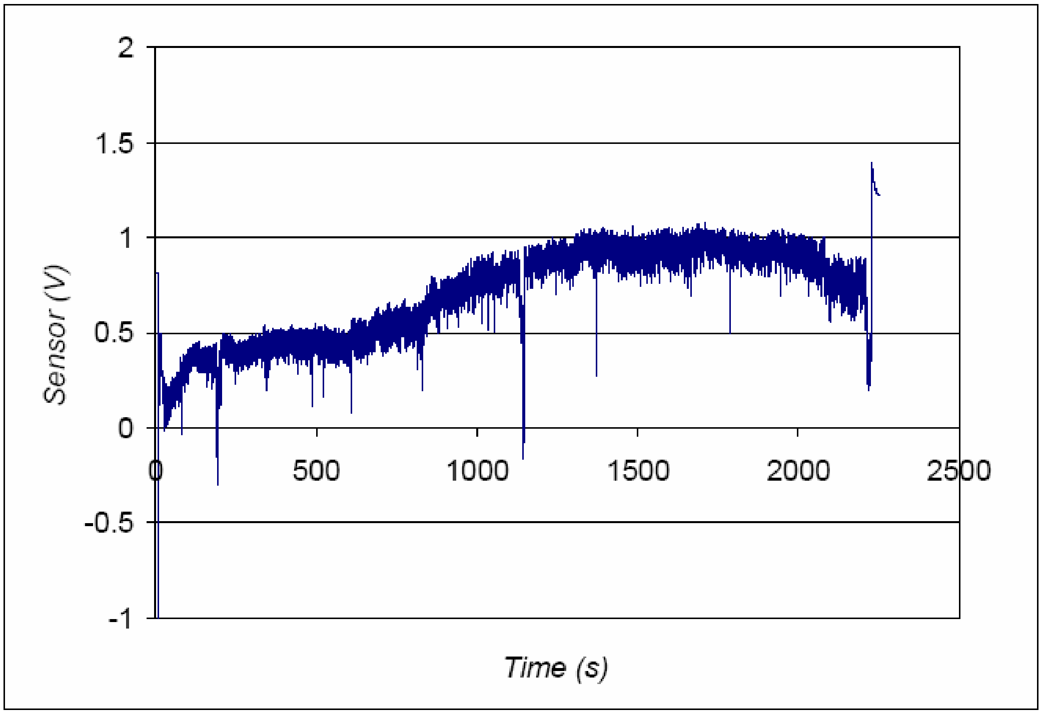

Figure 3.27: Sensor output for an engine start followed by continuous operation at 60% of full load for about 40 minutes

3.7.1 Baseline Drift

It was observed that there was drift in the baseline level of the sensor during continuous operation for long durations. There was no preferred direction for this drift. During some runs the baseline shifted in the positive direction while it drifted in the opposite direction during others. Several tests were carried out to further investigate this drift in the baseline level.

Two sensors were mounted simultaneously in a 1.5 inch PVC pipe connected to the main exhaust line downstream of a ball valve. One sensor was connected to the charge amplifier while the other was connected to the current to voltage converter. The engine was allowed to reach a steady idling speed after start-up. The load was then increased to about 60% of full load. After approximately every minute the valve was turned off for a few seconds to stop exhaust flow past the sensor electrodes. The drift in the signal baseline level over time could now be monitored. It was observed that the biggest shift in the baseline level occurred about 2-3 minutes after start-up. The drift in the baseline level after this initial shift was very gradual and the signal magnitude, which is the difference between the baseline and the signal level, remained consistent as shown in Figure 3.28.

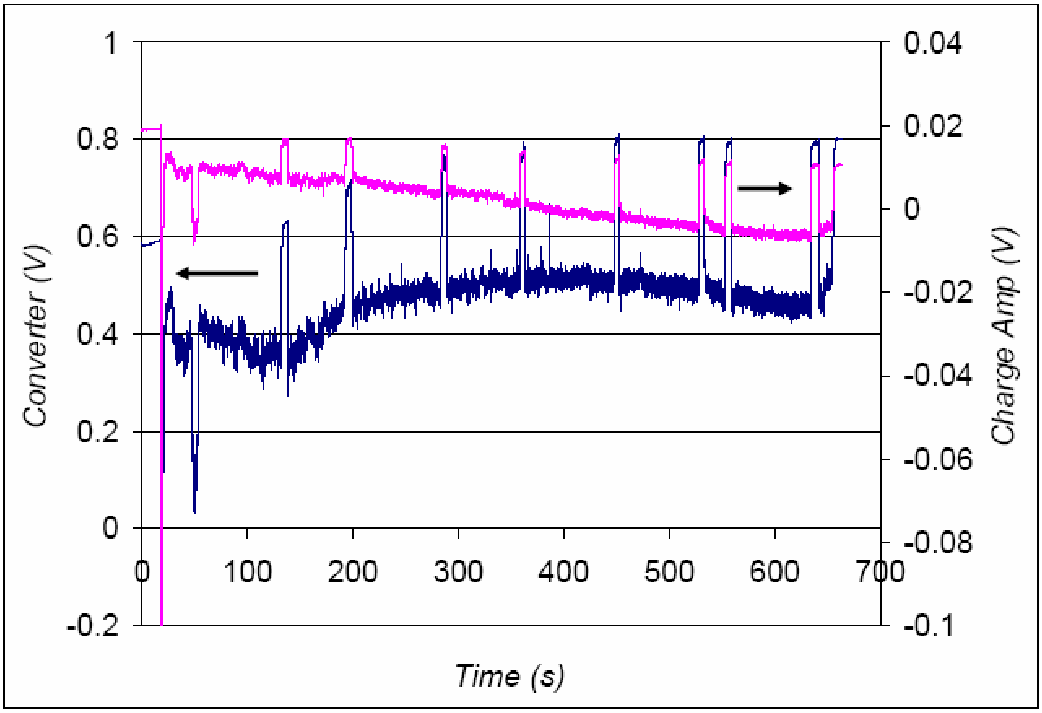

Figure 3.28: Drift in the baseline level of two sensors during continuous operation at 60% of full load in a PVC pipe

During some runs hot air was blown across the BNC connections of the sensor with a heat gun. The hot air had very little effect on the sensor signal or the baseline as shown in Figure 3.29. Heating up of the sensor connections over time was thus ruled out as a possible reason for the drift.

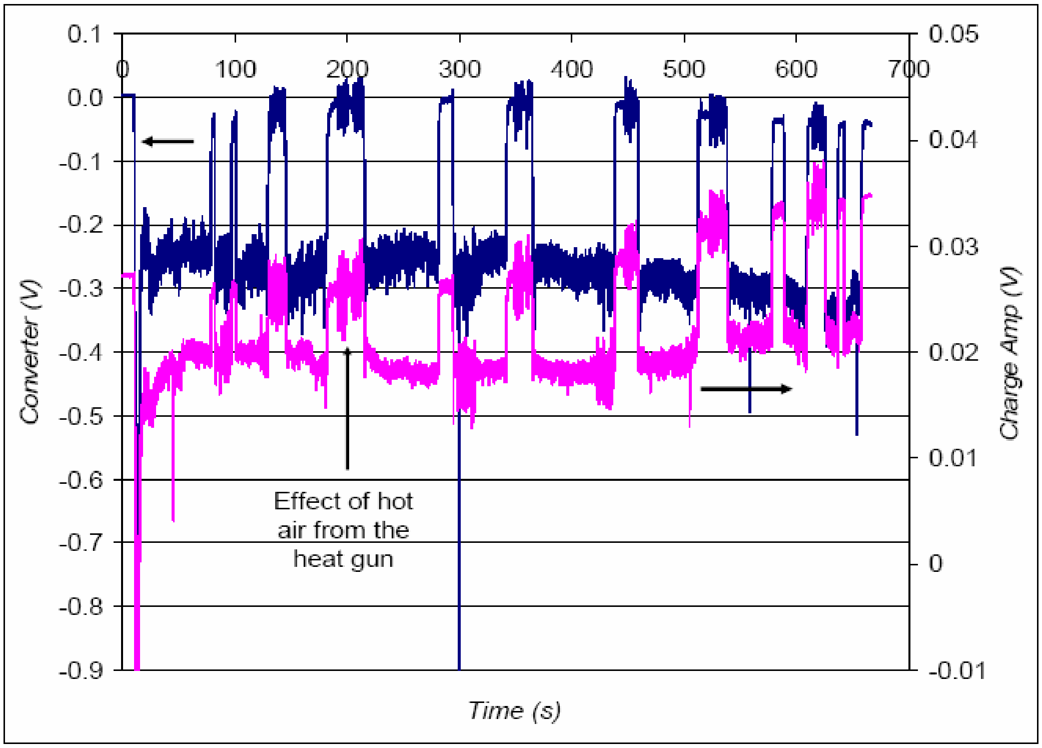

Figure 3.29: Effect of hot air flow across the sensor on the signal and baseline level

Cooling the charge amplifier and the current to voltage converter with a window AC unit had no effect on the baseline drift. The power to the amplifier and the converter was left on for 2-3 days. This reduced the drift somewhat, but during continuous operation in the engine exhaust the baseline level still drifted over time.

The baseline level was monitored with the sensor mounted in the exhaust but with no exhaust flow. It was observed that even without exhaust flow across the sensor electrodes the baseline level drifted over time as shown in Figure 3.30. This effect was observed for both the charge amplifier and the current to voltage converter. It is thus believed that the drift in the baseline level is due to the electronics and not the sensor itself.

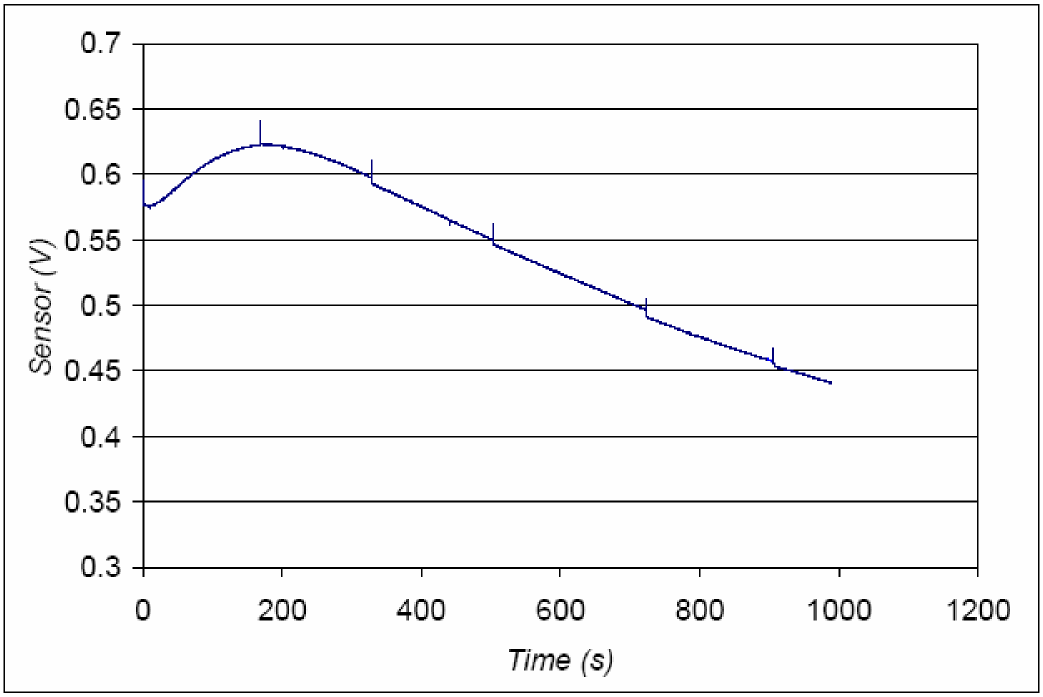

Figure 3.30: Drift in the sensor baseline with no exhaust flow past the electrodes

In this study, the drift in the baseline level was not a major problem since it occurred during continuous operation over long durations, while for most runs the sensor signal was recorded for 1-2 minutes. However, this drift in the baseline level will have to be eliminated before the sensor can be used for production applications. A possible solution is to modify the sensor electronics to record the signal magnitude, the difference between the baseline and the signal level, which remained fairly consistent. This strategy will require monitoring of the sensor baseline level in real- time.

Chapter 4: Performance Characteristics & Principle of Operation

This chapter presents the results of an experimental study of various parameters that affect the performance of the electronic sensor. Parameters considered included sensor electrode length, diameter, electrode spacing, applied bias voltage, bulk flow velocity across the sensor electrodes, and the concentration of carbonaceous particulate matter in engine exhaust. The sensor was tested in the exhaust of a single cylinder diesel engine. A correlation was developed to predict the sensor signal under any engine operating condition and values of these parameters. This correlation could be used to develop control strategies for the sensor for on-board operation in a production vehicle. The experiments also provided insight into the physical mechanism governing sensor behavior, regarding the charge transport between the two electrodes of the sensor. A 1-D model was developed to support the hypothesis for the physical mechanism governing sensor behavior.

4.1 Performance Characteristics

4.1.1 Effect of Electrode Spacing

The first set of experiments was conducted using three sensors with electrodes of the same material, diameter and similar length but different electrode spacing. The geometric specifications of the three sensors are given in Table 2. A photograph of the three sensors is shown in Figure 4.1.

Table 2: Specifications for sensors with different electrode spacing

	Close Spacing	**Medium Spacing**	**Wide Spacing**
Spacing (mm)	1.6	3.2	5.6
Length (mm)	23.8	23.8	26
Diameter (mm)	1.65	1.65	1.65

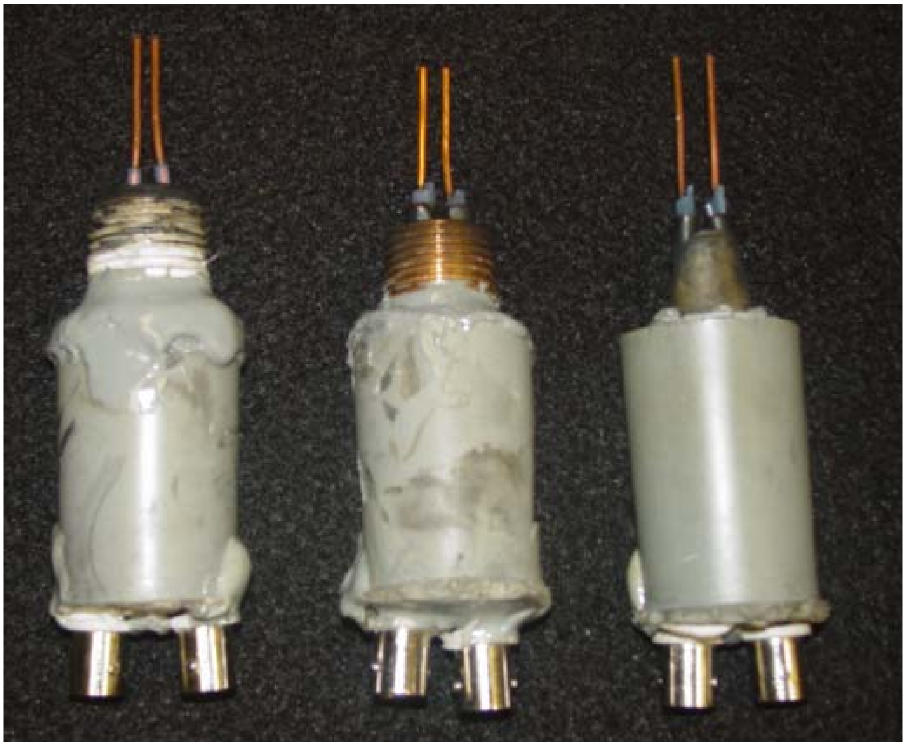

Figure 4.1: Photograph of the three sensors with different electrode spacing

The experiments were performed at a constant engine speed of 1250 RPM while the load was varied to change the level of particulate matter in the exhaust. Testing was done at five load conditions ranging from idle to 90% of full load. To check for repeatability, at least four separate runs were performed for each sensor geometry, and on different days. Figure 4.2 represents the sensor signal averaged over all the runs, showing the absolute mean sensor output as a function of electrode spacing for increasing load at a constant speed of 1250 RPM. The error bars represent +/- 1 standard deviation. A least squares power law fit was applied to the data for each load condition. Overall a good correlation is observed with an R^2 value of at least 0.97. It can be seen from the data that the sensor signal had an inverse power dependence on the spacing between the two electrodes. The least square power values for the five engine load conditions are shown in Figure 4.3. A power law exponent of 1.28, which was the average of the five values, was used to develop the correlation relating signal output to PM concentration.

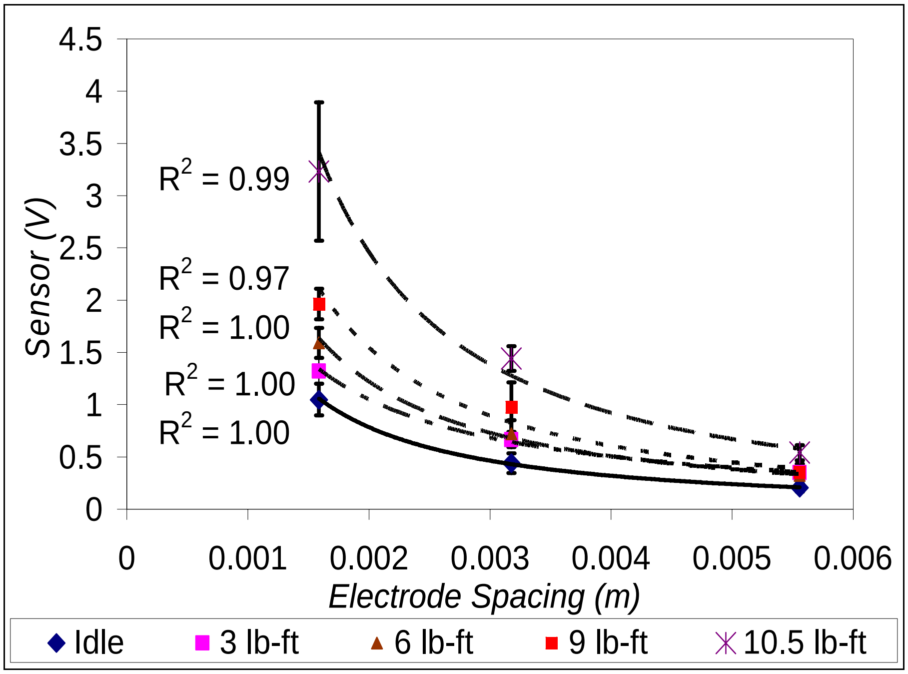

Figure 4.2: Effect of electrode spacing on sensor signal for five engine load conditions

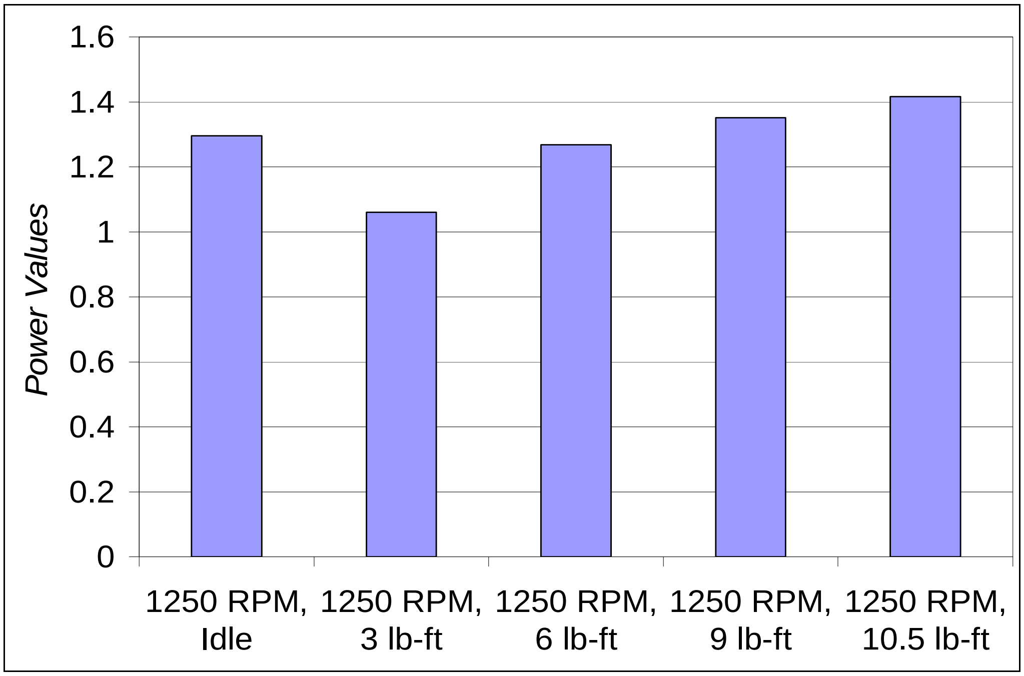

Figure 4.3: Power values for five engine load conditions

4.1.2 Effect of Electrode Length

To examine the effect of electrode length on the sensor signal a set of experiments was performed using three different sensors with electrodes of the same material, diameter and similar spacing between the electrodes but different lengths. Two of the sensors had electrodes that were straight while the third had electrodes that were bent into a “U” shape for compactness. The design specifications of the three sensors are given in Table 3. A photograph of the “U” shaped sensor is shown in Figure 4.4.

Table 3: Specifications for sensors of different electrode lengths

	Sensor 1 (Straight)	**Sensor 2 (Straight)**	**Sensor 3 (U shape)**
Spacing (mm)	1.6	1.6	1.6
Length (mm)	13.7	23.8	39.7
Diameter (mm)	1.65	1.65	1.65

Figure 4.4: Photograph of the “U” shaped sensor

The experiments were performed at a constant engine speed of 1250 RPM and two load conditions of idle and 25% of full load. At least three separate runs were performed for each sensor geometry. Figure 4.5 represents the sensor signal averaged over all the runs, showing the absolute mean sensor output as a function of electrode length for the two load conditions at a constant speed of 1250 RPM. The error bars represent +/- 1 standard deviation. A least squares fit was applied to the data for each load condition. The R^2 value is at least 0.97. It can be observed from the data that the sensor signal varies linearly with electrode length.

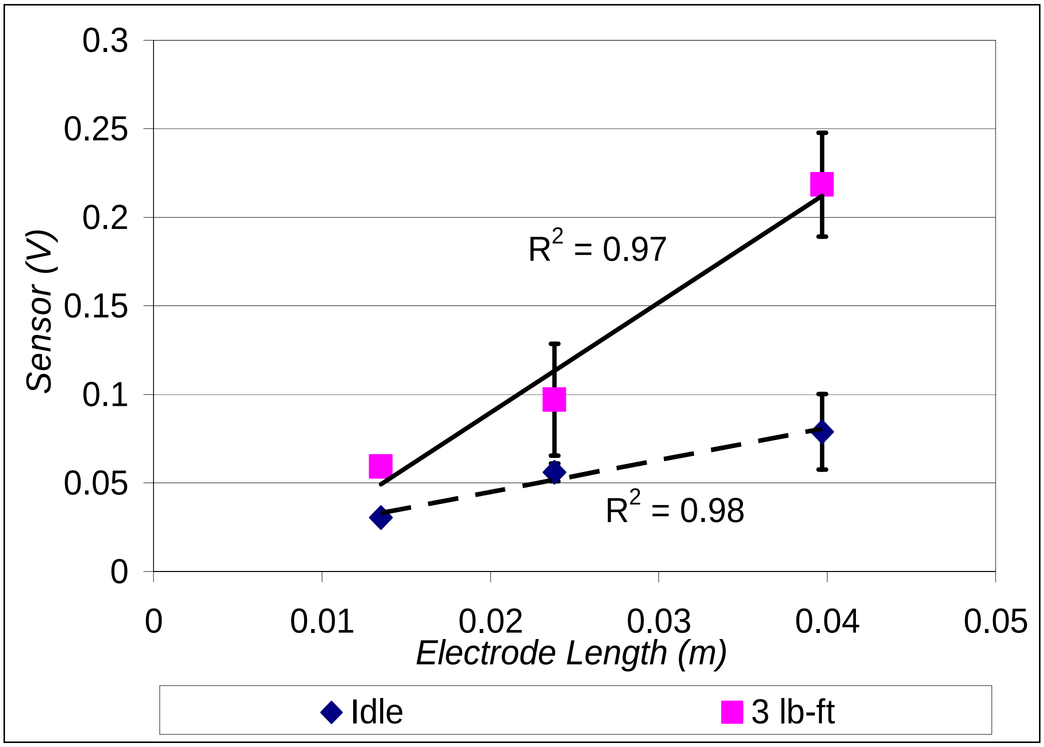

Figure 4.5: Effect of electrode length on sensor signal for two engine load conditions

4.1.3 Effect of Applied Voltage

To study the effect of the applied voltage bias on the sensor signal, experiments were performed at engine idle and two engine speeds of 1250 and 1500 RPM. The applied bias voltage was varied from 500 V to 1200 V. At least three separate runs were performed for each value of the bias voltage. Figure 4.6 represents the sensor signal averaged over all the runs, showing the absolute mean sensor output as a function of the applied voltage for the two engine operating conditions. The error bars represent +/- 1 standard deviation. A least squares fit was applied to the data for each condition. The R^2 value of the fit is at least 0.95. The sensor signal varies linearly with the applied bias voltage.

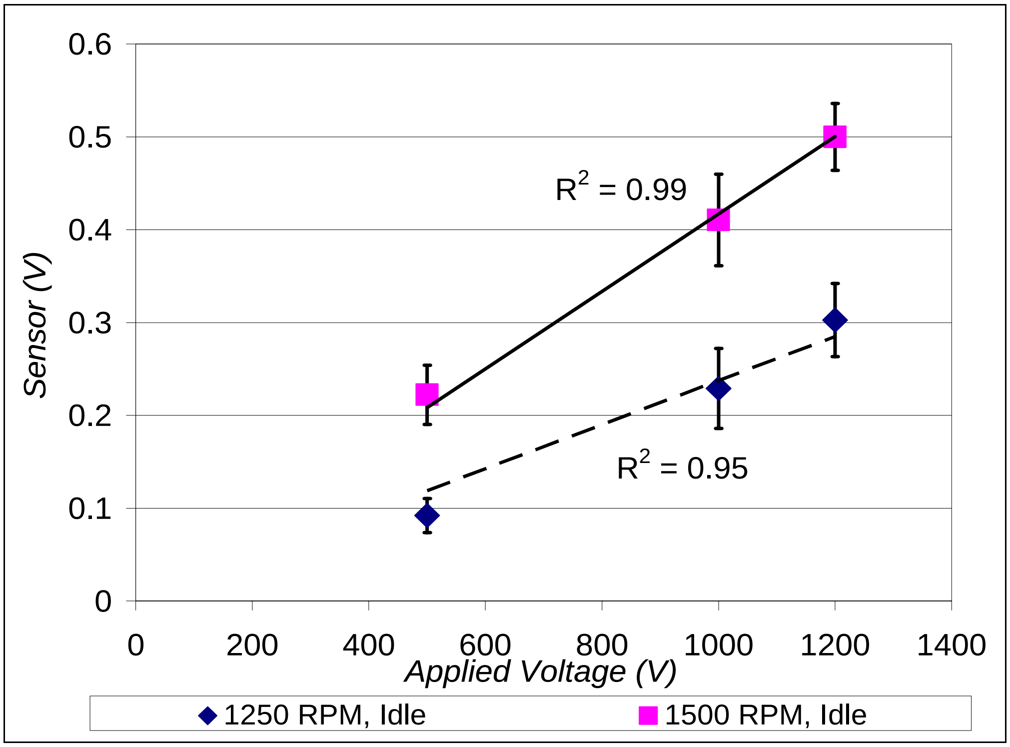

Figure 4.6: Effect of applied voltage on the sensor signal

4.1.4 Effect of Flow Velocity

To examine the effect of the bulk flow velocity on the sensor signal a set of experiments was performed using four sensors of different designs at engine idle and three different engine speeds of 1250, 1500 and 2000 RPM. At each engine speed the flow velocity across the sensor electrodes was varied by using two PVC pipes of diameters 2 and 3 inches in addition to the stock exhaust of 1.5 inch diameter. At least three separate runs were performed for each sensor and flow velocity. The design specifications of the four sensors are given in Table 4. The calculated flow velocities for different engine speeds and pipe diameters are given in Table 5.

Table 4: Design specifications for the different sensors

	Sensor 1	**Sensor 2**	**Sensor 3**	**Sensor 4**
Spacing (mm)	1.2	2.8	1.6	2.4
Length (mm)	19	7.1	7.1	6.4
Diameter (mm)	2.3	0.6	0.6	2.0

Table 5: Flow velocities for different engine speeds and pipe diameters

	1250 RPM	1500 RPM	2000 RPM
1.5 inches (stock)	4.2 m/s	5.2 m/s	7.1 m/s
2 inches	2.3 m/s	2.8 m/s	3.9 m/s
3 inches	1.0 m/s	1.2 m/s	1.7m/s

Figure 4.7, 4.8 4.9 & 4.10 represent the sensor signal averaged over all the runs, showing the absolute mean sensor output as a function of flow velocity for the four sensor designs and three engine speeds of 1250, 1500 and 2000 RPM. The error bars represent +/- 1 standard deviation. A least squares fit was applied to the data for each speed condition. Overall a good correlation is observed with an R^2 value of at least 0.9.

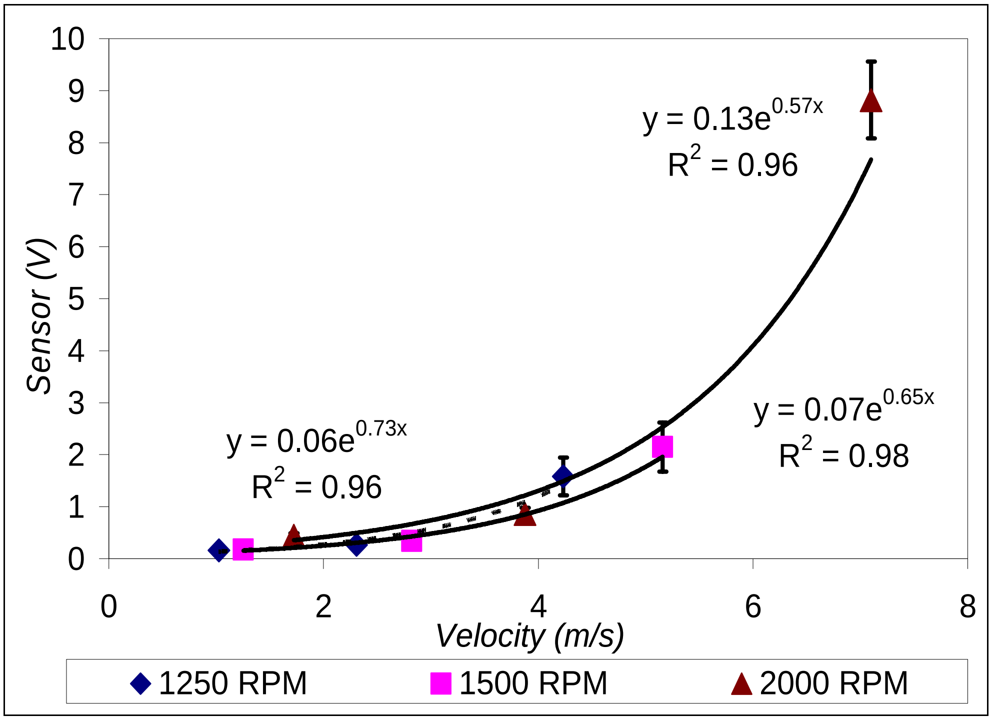

Figure 4.7: Effect of flow velocity on the signal magnitude of sensor 1

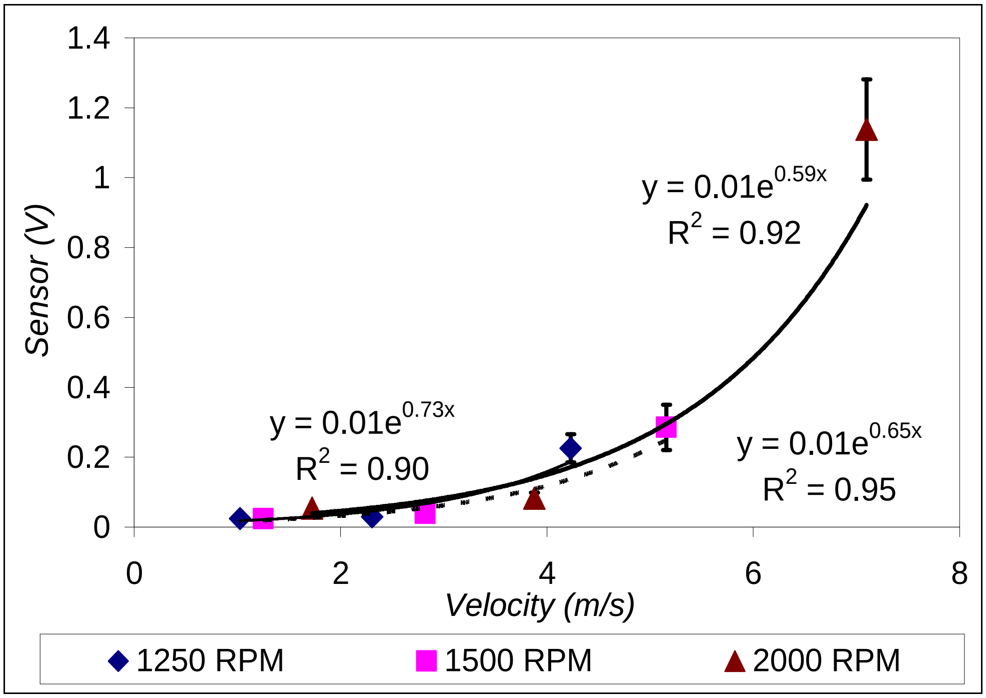

Figure 4.8: Effect of flow velocity on the signal magnitude of sensor 2

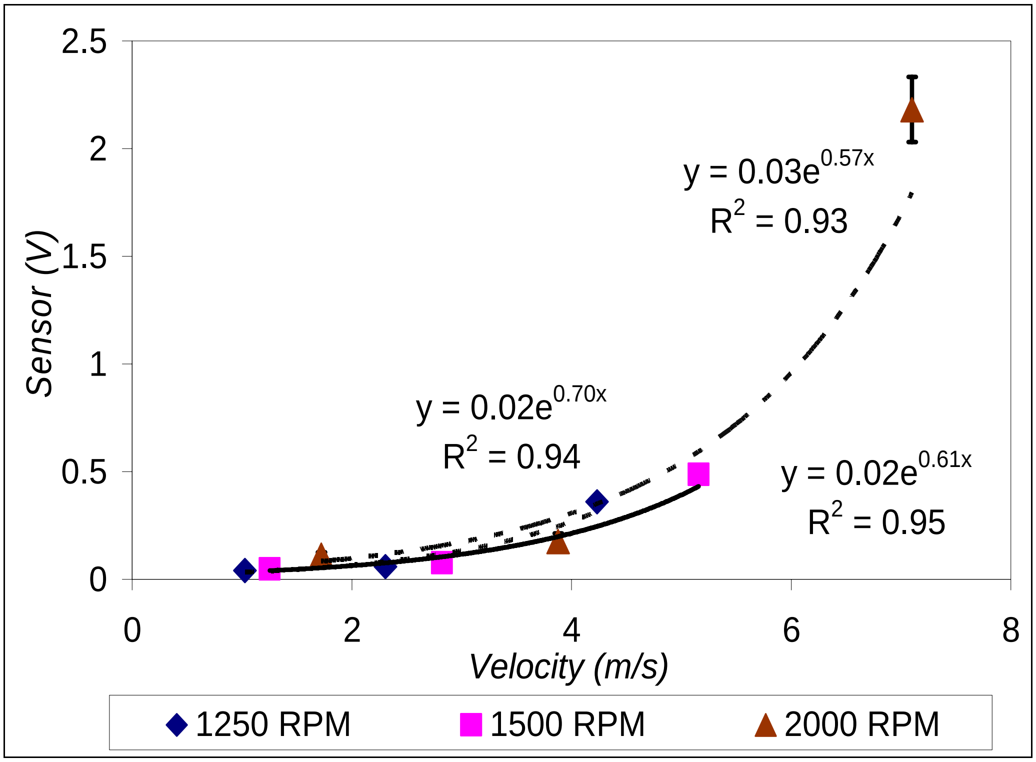

Figure 4.9: Effect of flow velocity on the signal magnitude of sensor 3

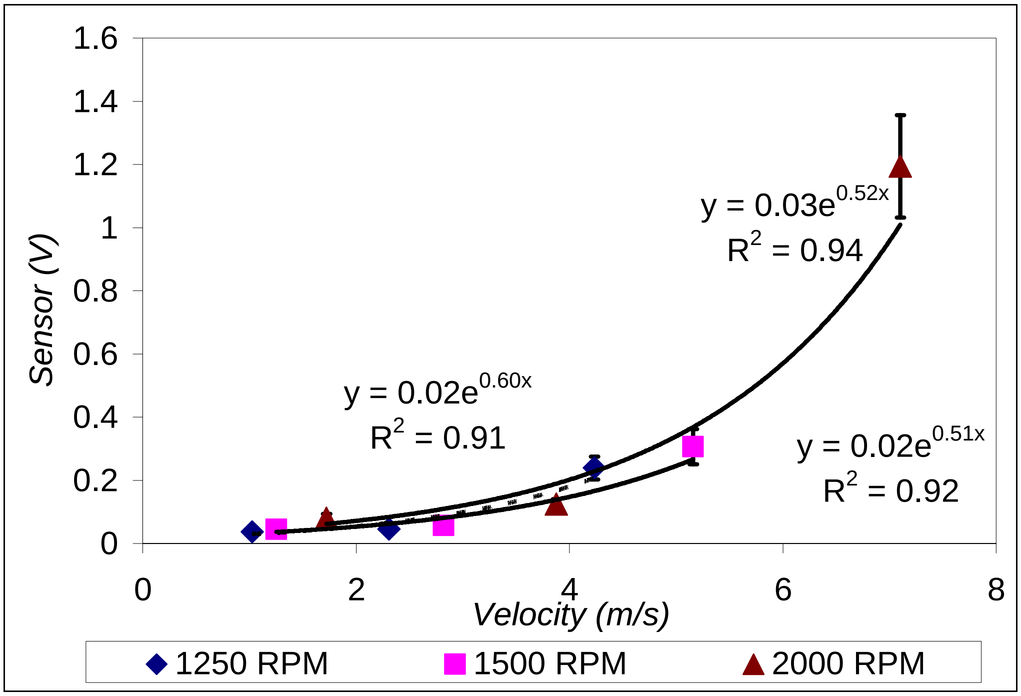

Figure 4.10: Effect of flow velocity on the signal magnitude of sensor 4

The sensor signal, thus, varies exponentially with the bulk flow velocity across the sensor electrodes. The sensitivity of the sensor signal to the bulk flow velocity is not clearly understood. It is interesting to note, that there might have been variations in the composition of PM at different engine speeds, resulting in different exponent power values for the least squares fit to the data. This can be explored further to gain more insights into the dependence of the sensor signal on the flow velocity. A power value of 0.62, which was the mean value for the four sensor designs, was used to develop the correlation.

4.1.5 Effect of Carbon Mass Concentration

A set of experiments was conducted using three sensors of different designs to correlate the sensor signal with particulate mass accumulated on filters. The geometric parameters of the three sensors are given in Table 6. The experiments were performed at a constant engine speed of 1250 RPM while the load was varied to change the level of particulate matter in the exhaust. Testing was done at five load conditions ranging from idle to 90% of full load. At each load condition the engine was allowed to stabilize for 30-45 seconds. The sensor signal was then recorded for one minute. Simultaneously an exhaust sample was drawn through the filter paper by a vacuum pump to correlate the sensor signal to the mass of particulates accumulated on filters. While the recording of the sensor output was stopped after one minute, exhaust was allowed to pass through the filter for five minutes to ensure sufficient accumulation. To check for repeatability, at least four separate runs were performed for each sensor geometry and on different days. At the end of each day of testing the filter papers were heated on electrical hot plates for 24 hours to evaporate water and soluble organic fractions (SOF). Since the sensor is sensitive to only to the carbonaceous fraction of particulate matter, it was necessary to remove the SOFs from the filter so that the sensor signal could be correlated to only the carbonaceous component of particulate matter. The filters were weighed using a microbalance, which had a resolution of 0.1 mg, to measure the accumulation of carbonaceous particulate matter.

Table 6: Specifications for the different sensors

	Sensor 1	**Sensor 2**	**Sensor 3**
Spacing (mm)	1.6	2.0	3.2
Length (mm)	23.8	24.6	23.8
Diameter (mm)	1.65	6.35	1.65

Figure 4.11, 4.12 & 4.13 represent the data for the three sensors along with a least squares fit to the data that was forced through the zero. Overall, a good correlation between the sensor and filter mass is observed. The mean sensitivity of a typical sensor, based on the fit to the data, was 0.015 g/m^3 per volt. The lowest PM levels measured were at engine idle where the PM concentration was about 0.01 g/m^3. This level is still well above the noise level of the sensor so lower PM levels are resolvable.

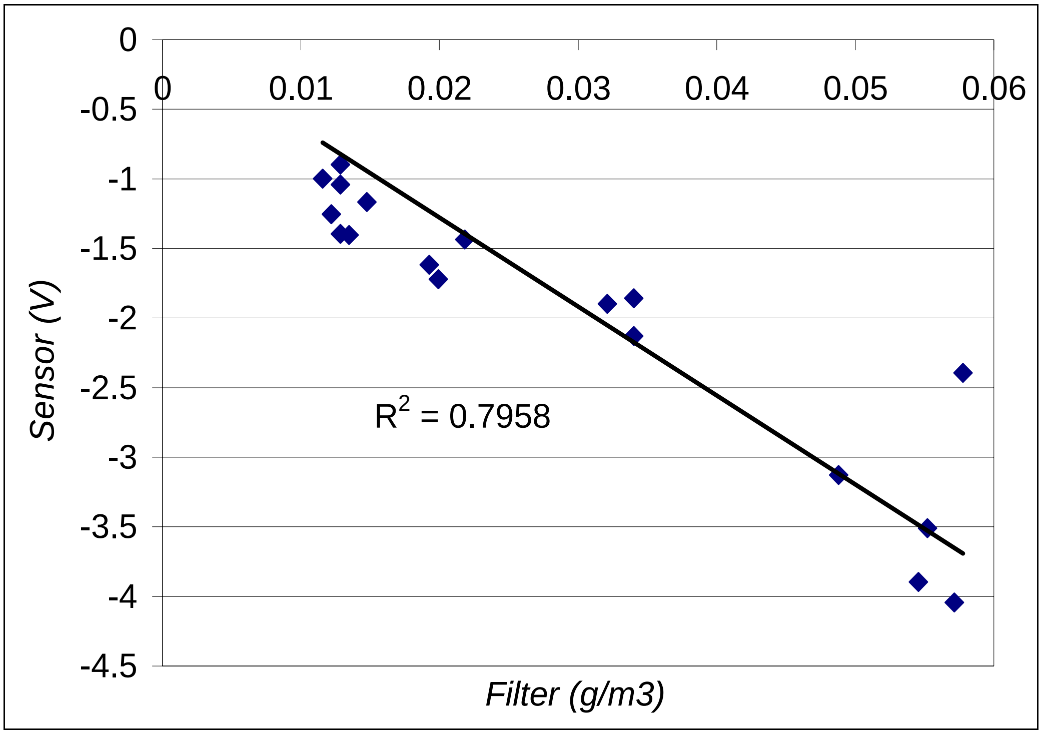

Figure 4.11: Correlation between the sensor signal and filter mass loading for sensor 1

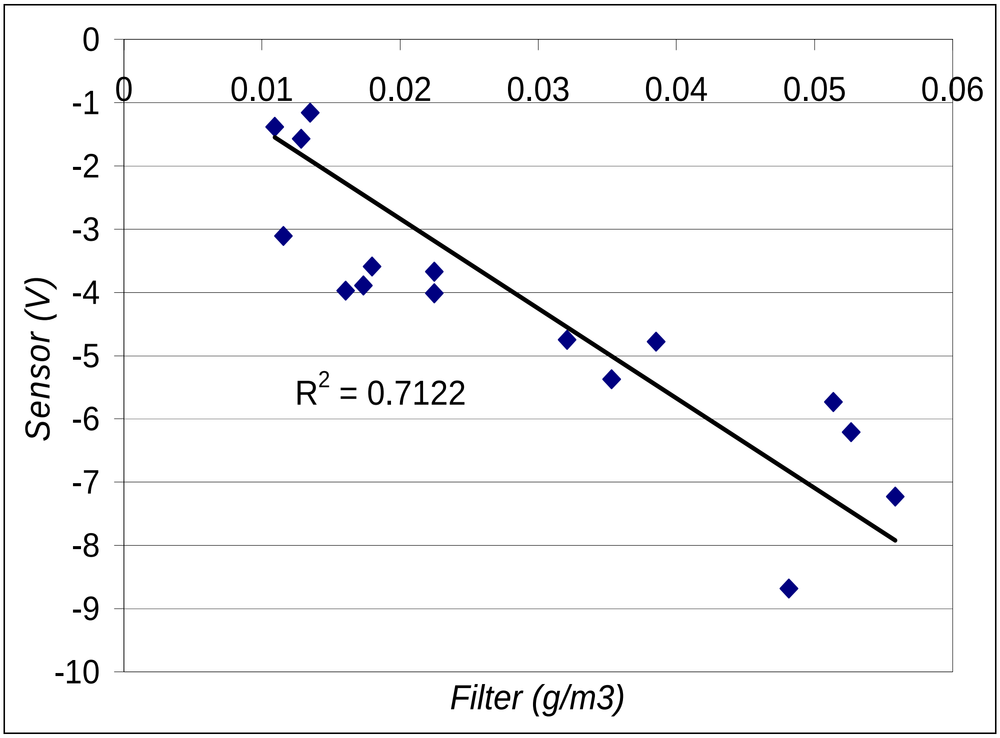

Figure 4.12: Correlation between the sensor signal and filter mass loading for sensor 2

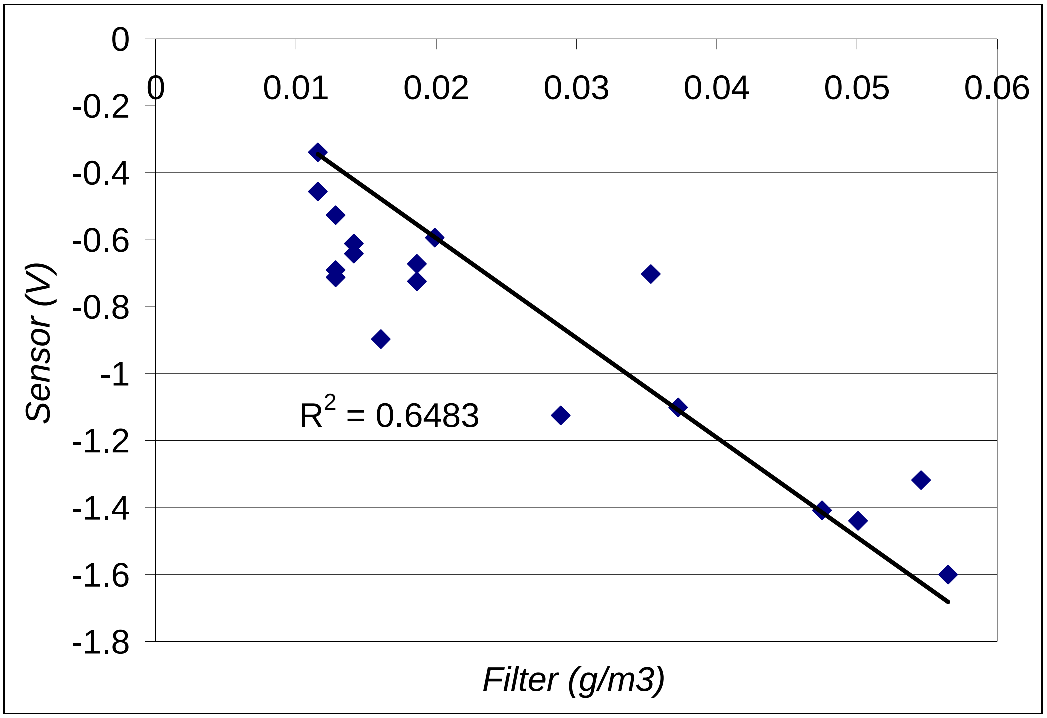

Figure 4.13: Correlation between the sensor signal and filter mass loading for sensor 3

It was found that electrode diameter did not have a significant effect on the sensor signal. Based on this study of design parameters a correlation was developed to predict the sensor signal for any engine operating condition and sensor geometry. The correlation can be expressed as follows

$$Sensor(V) = 5.75 * 10^{-05} CV_o e^{0.62U} \frac{L}{S^{1.28}} \qquad (4.1)$$

where C is the mass concentration of carbonaceous PM in the exhaust in g/m^3, V_o is the applied bias voltage in volts, U is the exhaust velocity in m/s, L is the electrode length and S is the spacing between the electrodes in meters. This correlation could be used to develop control strategies for the sensor for on-board operation in a production vehicle. Alternatively, the dry soot concentration in the exhaust for any engine operating condition and sensor geometry can be expressed as follows

$$C(g/m^3) = \frac{Sensor(V) * S^{1.28}}{5.75 * 10^{-05} L V_o e^{0.62U}} \tag{4.2}$$

For one particular sensor geometry, a comparison was made between the measured sensor voltage and the sensor voltage predicted by the correlation based upon the PM concentration measured in the exhaust with filters. Figure 4.14 shows this comparison which was performed at a constant engine speed of 1250 RPM and five load conditions. Overall, the predicted signal values calculated from the correlation compare well with the experimental signal values. The largest difference between the two was 25%.

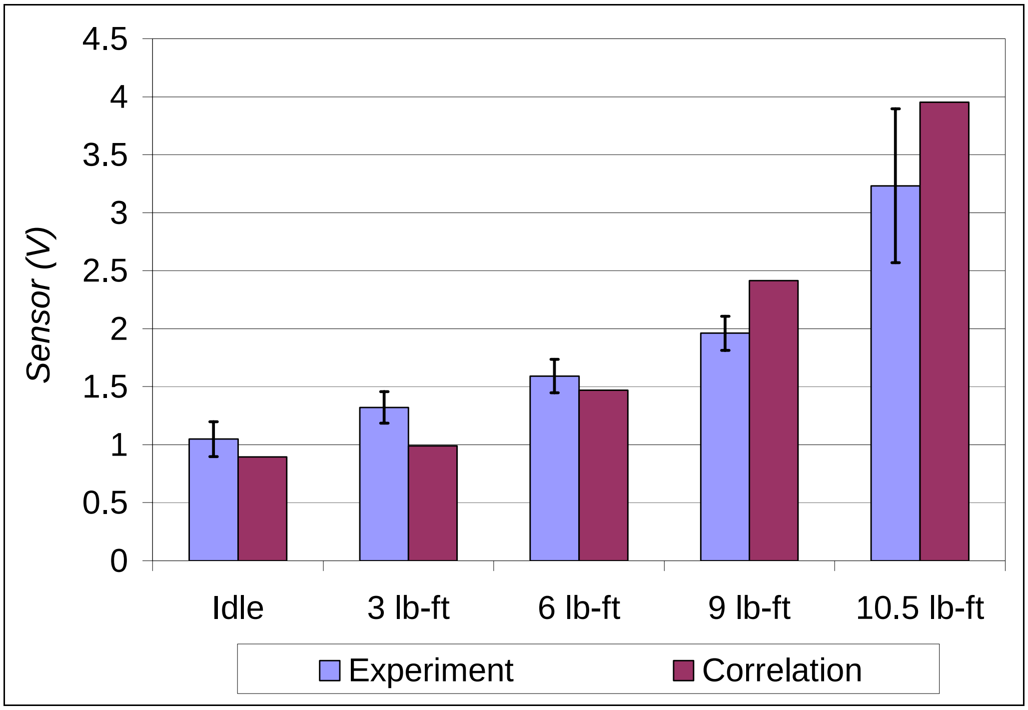

Figure 4.14: Comparison of experimental sensor signal to the correlation at constant engine speed of 1250 RPM and variable load

Figure 4.15 shows a similar comparison between measured and predicted signal voltages for experimental data taken at engine idle at speeds of 1250, 1500, and 2000 RPM. The signal calculated from the correlation compares well with the experimental signal level. The maximum difference between the two is 34%.

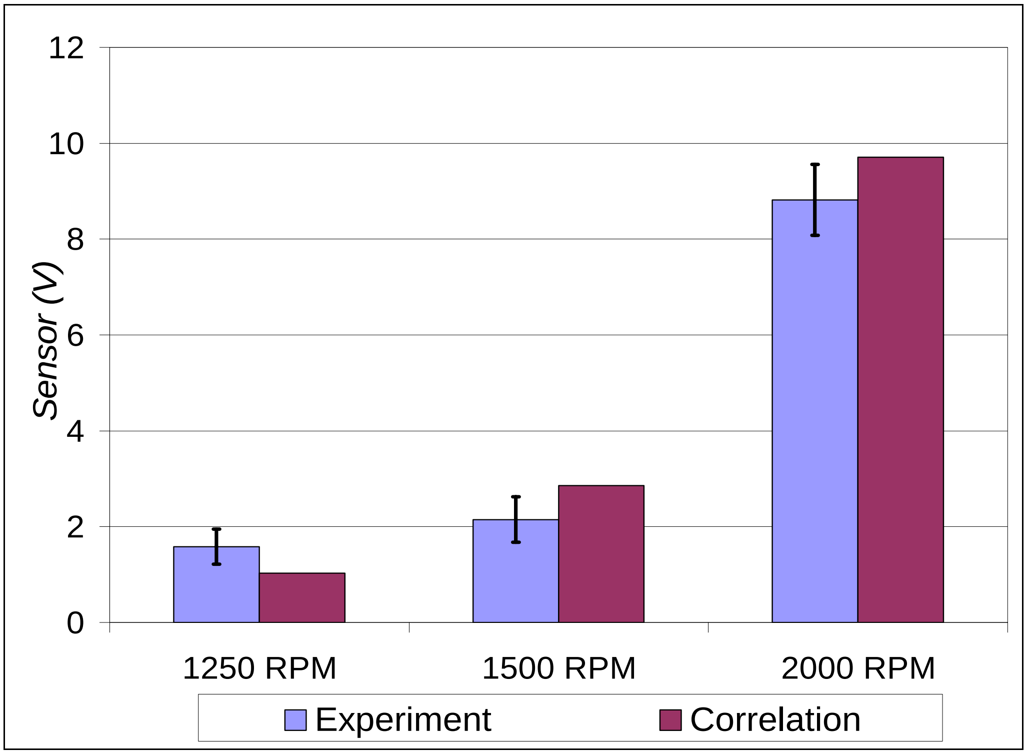

Figure 4.15: Comparison of experimental sensor signal to the correlation at engine idle and speeds of 1250, 1500 and 2000 RPM

Figure 4.16 shows a similar comparison between measured and predicted signal voltages for experimental data taken at engine idle at speeds of 1250, 1500, 1750 and 2000 RPM. The comparison was made at a new engine speed of 1750 RPM since this operating condition was not used in the development of the correlation. The signal calculated from the correlation compares well with the experimental signal level. The average deviation between the two was 26%.

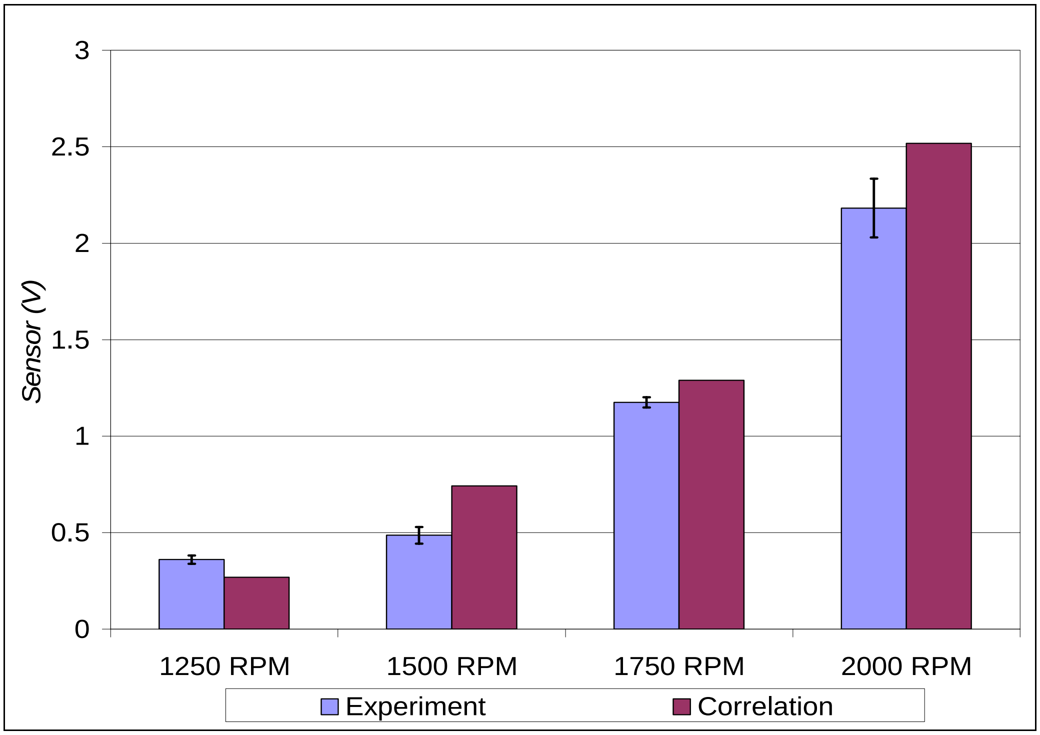

Figure 4.16: Comparison of experimental sensor signal to the correlation at engine idle and speeds of 1250, 1500, 1750 and 2000 RPM

4.2 Mechanism Governing Sensor Behavior

The initial hypothesis for the physical mechanism governing sensor behavior was that the carbonaceous fraction of particulate matter in engine exhaust forms a conducting channel between the two electrodes of the sensor thereby enabling current flow. This hypothesis had to be refined further to determine the exact mechanism of charge transport. Several insights were gained from this study of design parameters regarding the charge transport between the two electrodes of the sensor. The inverse power dependence of the sensor signal on the spacing (Equation 4.1) between the electrodes suggested a diffusion mechanism. If the two electrodes were line sources the diffusion of electrons between them would not be 1-Dimensional and would take place in a domain defined by a solid angle, which scales as the square of the distance between them. Being of finite diameter, the two electrodes were not line sources, alternatively, the projected area of an electrode was not big enough for purely 1-Dimensional transport. A power of 1.28 to the electrode spacing, therefore, indicated that formation of a conductive channel between the two electrodes of the sensor had some 2-dimensional effects and could be explained by a charge diffusion mechanism. The weak dependence of the sensor signal on the electrode diameter suggested that the transport of charge by diffusion between the two electrodes was not entirely ballistic but had a drift component along the electric field lines of force. The presence of a high positive voltage (1000 V) causes the charged particles to move along the electric field lines towards the unbiased signal electrode. If the diffusion were purely ballistic, then electrode diameter would have had a stronger effect. A drift-diffusion hypothesis was proposed to explain the mechanism governing sensor behavior. As per this hypothesis, there are three possible pathways for charged particles to reach the signal electrode. First, positively charged particles are created by the collision of charge neutral particles with the positive high voltage electrode. Charge, then propagates among particles through particle-particle collisions. Second, the naturally charged particles in the diesel exhaust diffuse towards the signal electrode due to concentration gradients between the two sensor electrodes. Finally, charge transport occurs between the two electrodes because of the drift of charged particles in the exhaust due to the applied bias voltage of 1000 V. Electrons are extracted when these charged particles collide with the signal electrode.

The drift-diffusion mechanism can thus be outlined as shown in Figure 4.17.

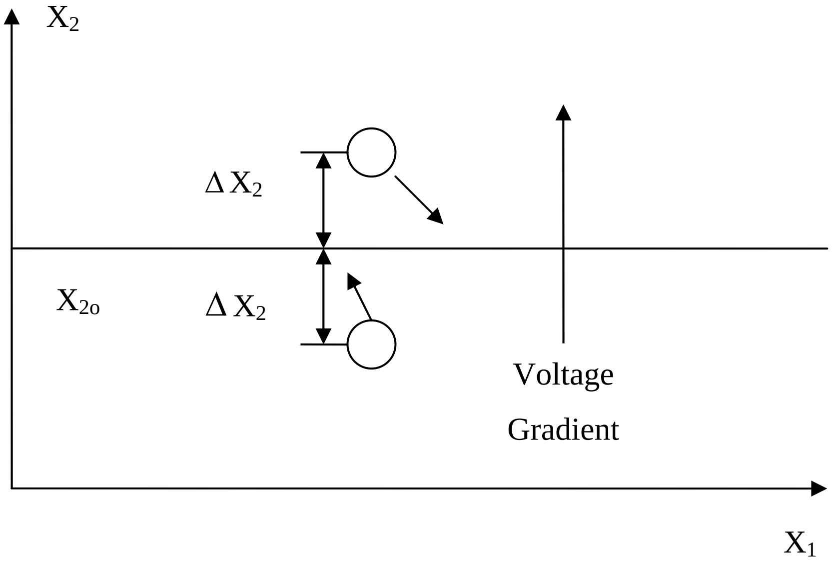

Figure 4.17: Schematic of the sensor mechanism

The net flux of charge due to diffusion can be expressed as

$$\Lambda_{diffusion} = u\left[n_c\left(X_{2o} - \Delta X_2\right) - n_c\left(X_{2o} + \Delta X_2\right)\right] \qquad (4.3)$$

where n_c is the number density of charged particles and u is the velocity of the particles due to Brownian motion. The movement of each particle can be described by the Langevin equation

$$m\frac{du}{dt} = -\zeta u + F(t) \qquad (4.4)$$

where u is the instantaneous velocity of the particle. The term ζu gives the Stokes' law drag force, $\zeta = 6\pi\mu R$ where R is the radius of the particle and μ is the viscosity of air [40, 41]. Using Taylor series in Equation 4.3

$$n_c\left(X_{2o} - \Delta X\right) = n_c\left(X_{2o}\right) - \frac{dn_c}{dX_2}\Delta X_2$$

$$n_c\left(X_{2o} - \Delta X\right) = n_c\left(X_{2o}\right) + \frac{dn_c}{dX_2}\Delta X_2$$

$$\therefore \left[n_c\left(X_{2o} - \Delta X\right) - n_c\left(X_{2o} + \Delta X\right)\right] = -2\frac{dn_c}{dX_2}\Delta X_2$$

$$\therefore \Lambda_{diffusion} = -2\frac{dn_c}{dX_2}\cdot \Delta X_2 \cdot u \tag{4.5}$$

$\Delta X \approx \lambda$, where λ is the mean free path of the charged particles i.e. the average distance a charged particle travels before collision with another particle. The diffusion component can be expressed as

$$\Lambda_{diffusion} = -\beta_c u \lambda \frac{dn_c}{dX_2} \tag{4.6}$$

The drift component can be expressed as

$$\Lambda_{drift} = -\mu_C n_c E \tag{4.7}$$

where E is the electric field strength, n_c is the number density of charged particles and μ_C is the electrical mobility of charged particles [41]. The total flux of charged particles is

$$\Lambda_{Total} = \Lambda_{diffusion} + \Lambda_{drift} \tag{4.8}$$

$$\therefore \Lambda_{Total} = -\beta_c u \lambda \frac{dn_c}{dX_2} - \mu_C n_c E \tag{4.9}$$

The linear dependence of the sensor signal on the electrode length might be due to the increase in ‘collection’ area for the charged particles reaching the signal electrode. The linear dependence on concentration could be due to the increase in charge carriers. The linear dependence on the applied bias voltage could be explained from the governing equation (Equation 4.7) for the drift of charged particles in an electric field. The electric field strength is defined as

$$E = \frac{V_o}{S} \tag{4.10}$$

where V_o is the applied bias voltage and S is the spacing between the electrodes. The sensitivity of the sensor signal to the bulk flow velocity is not clearly understood.

To obtain more evidence in support of this hypothesis the existing data from the parametric design study were analyzed further and another set of experiments was performed with different sensor geometries. The experimental data for the three sensors described in Table 2 were analyzed further. The three sensors described in Table 2 had electrodes of the same material, diameter and similar length but different electrode spacing. They were tested at a constant engine speed of 1250 RPM and five load conditions ranging from idle to 90% of full load. The amount of carbonaceous particulate matter accumulated on filters was measured at each load condition. In all these experiments the sensor was connected to a custom built current to voltage converter. The sensor output underwent further signal conditioning, through the voltage follower and low pass filter, and was finally recorded by a NETDAQ FLUKE data acquisition system. The current to voltage converter had a gain of

$$V_c = -1V/nA \tag{4.11}$$

where V_c is the output voltage of the converter. The measured sensor output voltage, averaged over one minute, was converted to a current signal using Equation 4.11.

The resistance of the conducting channel between the two electrodes was obtained using Ohm’s law

$$V_o = IR \tag{4.12}$$

where V_o is the applied bias voltage of 1000V, I is the current obtained from Equation 4.11 and R is the resistance of the conducting channel formed by soot particles between the two electrodes of the sensor. The resistivity (ρ) of the channel was determined as follows

$$\rho = \frac{RA}{S} \tag{4.13}$$

where A is the projected area of the sensor electrode (Diameter x Length) and S is the spacing between the two electrodes. The electrical conductivity (σ) of the channel is

$$\sigma = \frac{1}{\rho} \tag{4.14}$$

This definition of electrical conductivity was modified to include the concentration of soot particles in the exhaust. Since electron transport between the two sensor electrodes occurred through these soot particles, it was their concentration that determined the conductance of the channel. This normalized, mass specific, electrical conductance ($\sigma^{'}$) was defined as

$$\sigma' = \frac{S}{RA * C} \tag{4.15}$$

where C is the concentration, in g/m^3, of the carbonaceous fraction of PM in the exhaust as determined by the filter paper measurements.

Figure 4.18 shows the normalized conductance data for the three sensor designs. The data are represented along with least squares fit to the data.

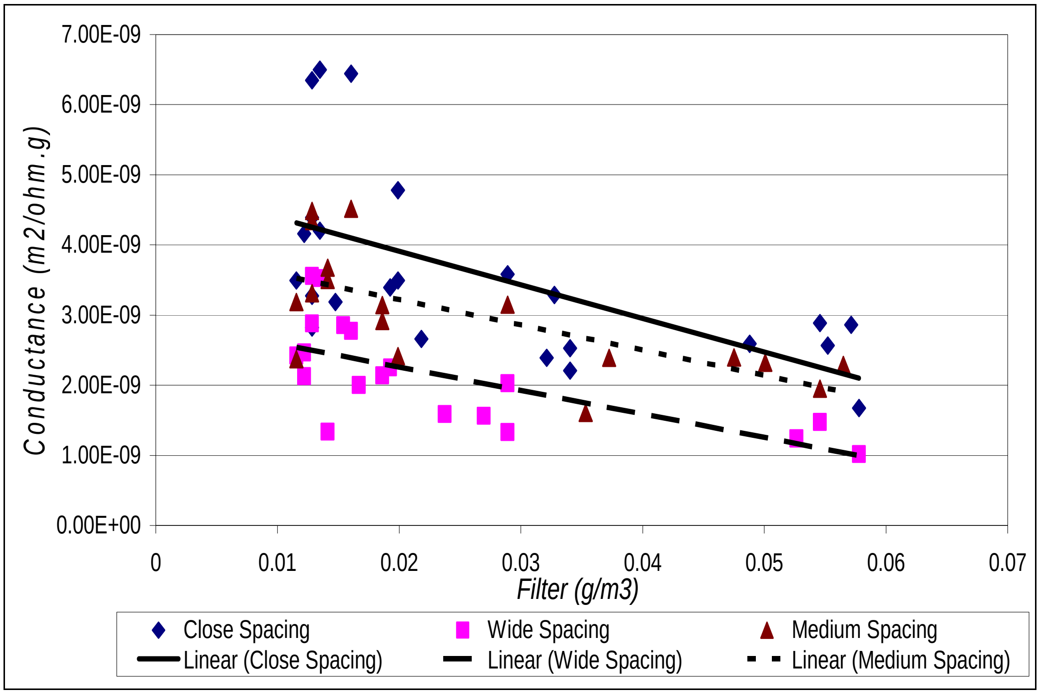

Figure 4.18: Normalized Conductance (σ') vs. Filter mass loading for the three sensor designs

Several insights were obtained from Figure 4.18. Since the conductance was normalized by the soot concentration, the three curves should have had zero slope when plotted against the filter mass loading, but they did not. This indicated that the increase in sensor signal with engine load was smaller than the soot concentration increase, which suggested a diffusion mechanism, since charge transport by diffusion scales inversely with concentration. With increase in concentration one would expect charge transport by diffusion to increase, but the increase in the number of particle-particle collisions inhibits transport, resulting in a net reduction in diffusion of charge to the signal electrode. The data seemed to indicate that the increase in soot concentration with engine load inhibited the diffusion of electrons between the two sensor electrodes due to increase in particle-particle collisions. Hence, the increase in sensor signal did not scale exactly with the increase in soot concentration resulting in a non-zero slope for the three curves.

Another observation was that the data for the three sensor designs should have converged to a single curve since the conductance was normalized by the projected area of the electrode and the spacing between them. The three curves collapsed on to each for a power value of 1.4 applied to the electrode spacing as shown in Figure 4.19 which was within 10% of the value used in the correlation (Equation 4.1).

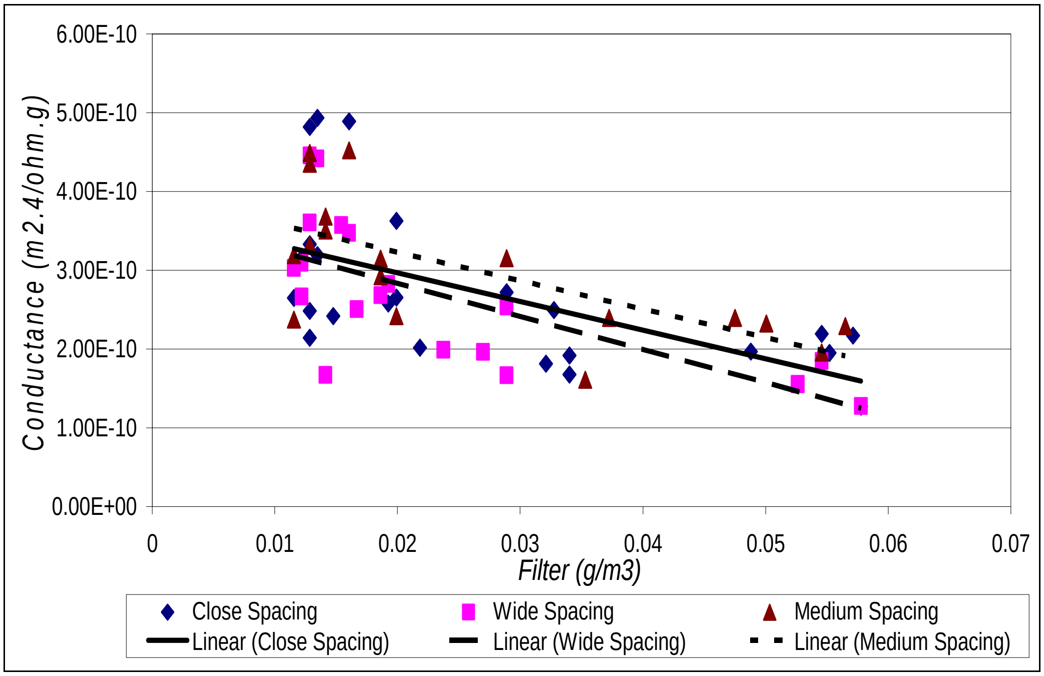

Figure 4.19: Normalized Conductance (σ') vs. Filter mass loading for electrode spacing raised to power 1.4

This gave further credence to the hypothesis that the electron transport by diffusion for these sensor designs was not 1-Dimensional but had some 2-Dimensional effects. To test whether this hypothesis was right, the projected electrode area could be made big enough so that the charge diffusion between the two electrodes would be 1-Dimensional. To investigate this, a new sensor design was constructed. This sensor had electrodes shaped in the form of plates. The specifications of this sensor are given in Table 7. A photograph of the sensor is shown in Figure 4.20. Measurements were made for an initial electrode spacing of 2.0 mm, which was subsequently increased to 3.2 mm. The sensor was tested at the same five operating conditions as before. Multiple runs were carried out to ensure repeatability.

Table 7: Specifications for two configurations of the ‘plate’ sensor

Plate Shaped Electrodes	**Close Spacing**	**Medium Spacing**
Spacing (mm)	2.0	3.2
Length (mm)	24.6	24.6
Width (mm)	6.35	6.35

Figure 4.20: Two views of the sensor with plate shaped electrodes

The normalized electrical conductance data for the two values of electrode spacing are shown in Figure 4.21. The data are represented along with least squares fit to the data. The two curves had a non-zero slope which was consistent with the diffusion hypothesis. The conductance data collapsed to a single curve for an electrode spacing power value of 1 as expected. This gave additional evidence in support of the drift-diffusion mechanism.

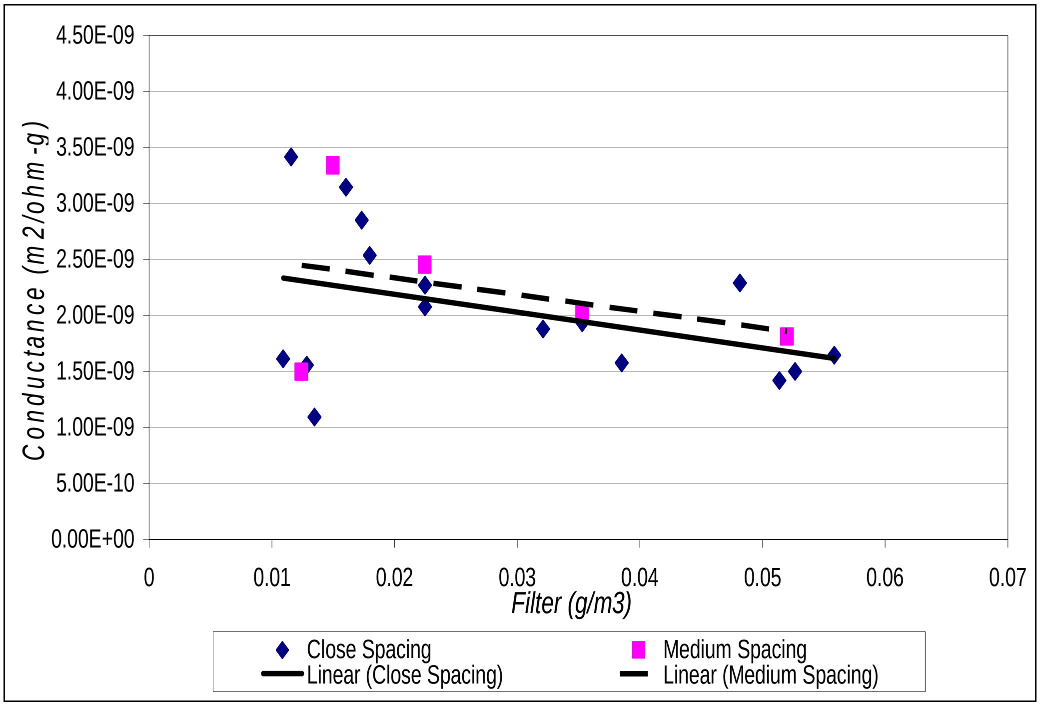

Figure 4.21: Normalized Conductance (σ') vs. Filter mass loading for two different electrode spacing values of the plate shaped sensor geometry

By the same logic, if the sensor electrodes were made of very thin wires they would approximate line sources. Two new sensors were, therefore, constructed with electrodes made of thin wires. The specifications of the two sensors are given in Table 8. A photograph of the two sensors is shown in Figure 4.22. The two sensors were tested at the same five operating conditions discussed before. Multiple runs were done to ensure reproducibility.

Table 8: Specifications of the sensors with thin electrodes

	Close Spacing	**Medium Spacing**
Spacing (mm)	1.4	2.2
Length (mm)	23	23.8
Diameter (mm)	0.635	0.635

Figure 4.22: Photograph of the two sensors with thin wires

The two curves, which are least squares fit to the data, collapsed on to each other for an electrode spacing power of 1.6 as shown in Figure 4.23. For an ideal line source this value would have been 2. The electrodes, though made of thin wires, are not line sources and should thus have a value close to 2, which they did. This gave more evidence in support of a drift-diffusion mechanism.

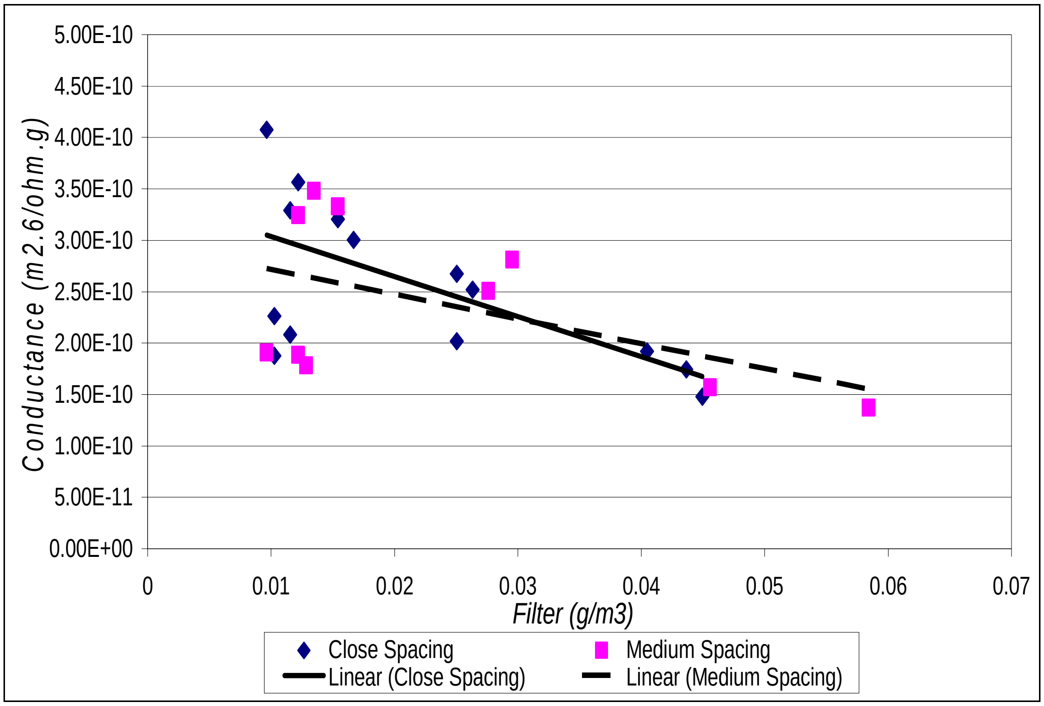

Figure 4.23: Normalized Conductance (σ') vs. Filter mass loading for two sensors with small diameter electrodes.

It was known that electrode diameter had a very weak effect on the sensor signal. More data analysis was carried out to investigate this further. The electrode diameter was eliminated from the definition of normalized electrical conductance (Equation 4.15) and a power of 1.6 was used for the electrode spacing for all sensor designs. This produced a very good correlation between the sensors of diameters 1.65 mm and 0.635 mm as shown in Figures 4.24 and 4.25 respectively. It is important to note that the scales on both plots are the same. The electrode length was retained in the equation since it was known from Equation 4.1 that the sensor signal varied linearly with electrode length.

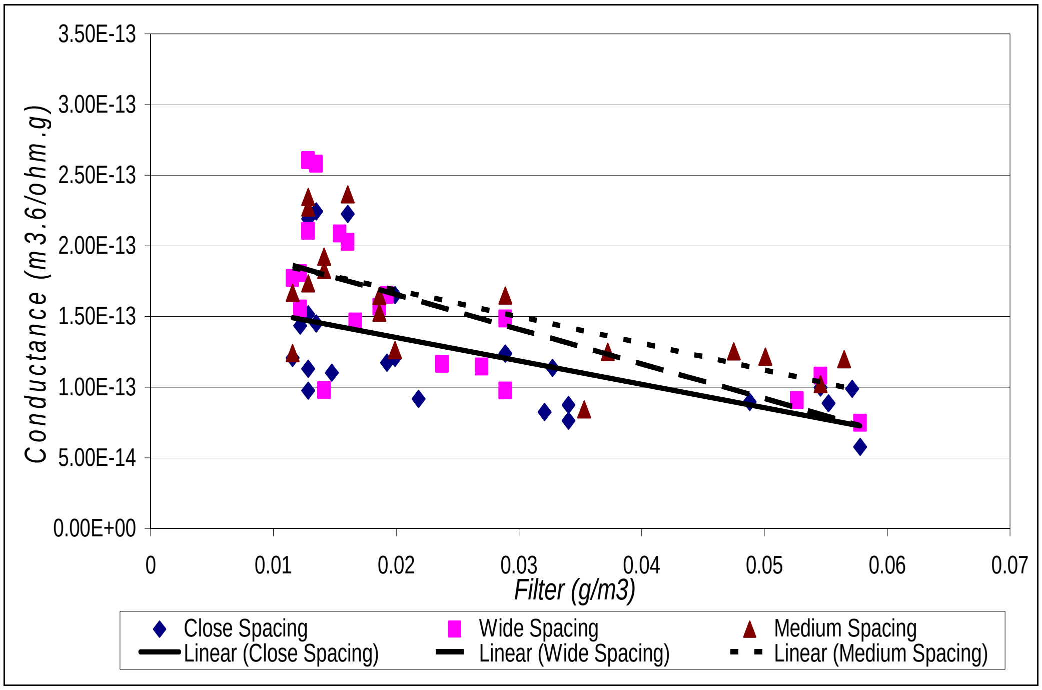

Figure 4.24: Normalized Conductance (σ') without electrode diameter vs. Filter mass loading for the sensors with electrode diameter of 1.65 mm

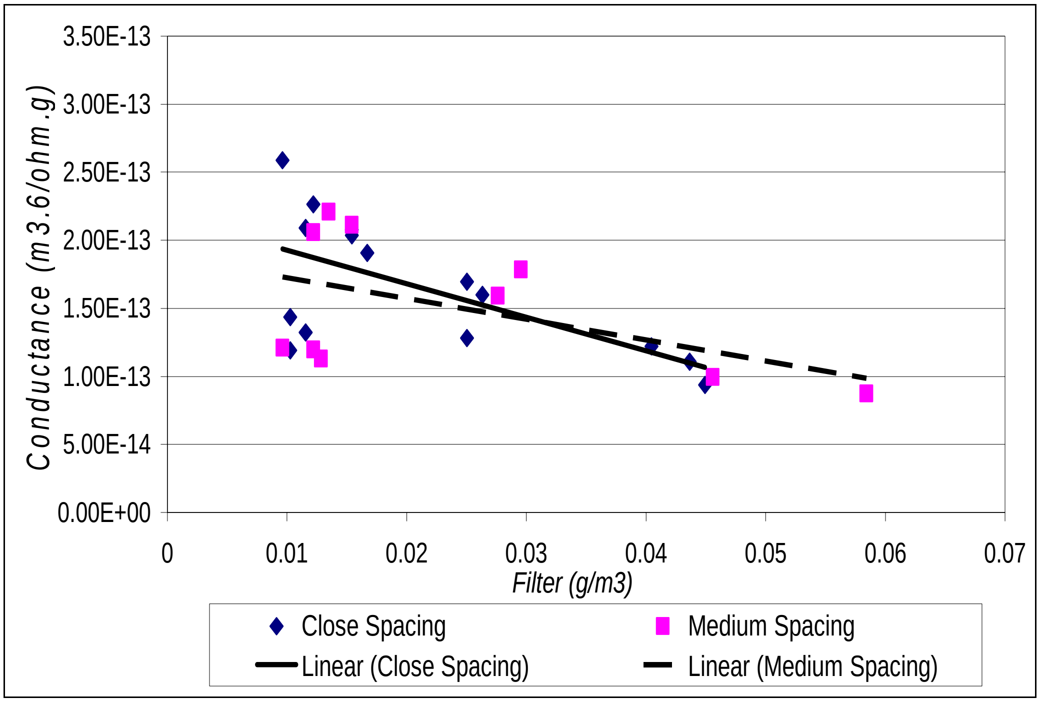

Figure 4.25: Normalized Conductance (σ') without electrode diameter vs. Filter mass loading for the sensors with electrode diameter of 0.635 mm

Using a power value of 1.6 instead of 1.4 for the sensor designs with electrode diameter 1.65 mm not only produced a good correlation between the three sensors but also with the sensors made of smaller diameter electrodes. This indicated that mechanics of charge transport were the same for both sensor designs irrespective of the electrode diameter. Electrode diameter, thus, had a weak effect on charge propagation. The same procedure was used to normalize the electrical conductance data of the sensor with plate electrodes. The data are represented along with the least squares fit to the data in Figure 4.26.

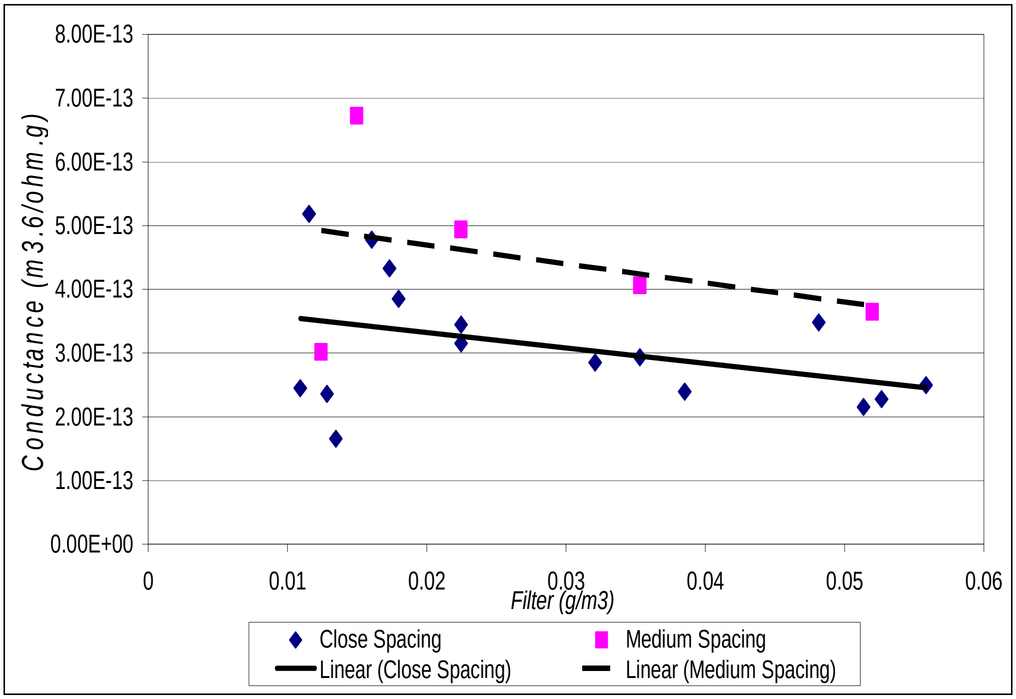

Figure 4.26: Normalized Conductance ($\sigma^{'}$) without electrode width and electrode spacing of power 1.6 vs. Filter mass loading for the sensor with plate shaped electrodes

Though the width of the plate shaped electrodes was almost an order of magnitude greater than the smallest diameter electrode, the normalized electrical conductance was on the same order of magnitude as the other two sensor designs, when the plate width was eliminated from the equation, proving that the electrode diameter had a very weak effect on the sensor signal. It also led to the conclusion that the transport of charge by diffusion between the two electrodes was not entirely ballistic but had a drift component along the electric lines of force. Presence of a high positive voltage (1000 V) causes the charged particles to move along the electric field lines towards the unbiased signal electrode. If the diffusion were purely ballistic, then electrode diameter would have had a stronger effect. The experimental data and analysis indicated that the overall propogation of charge had two components – diffusion and drift along the electric field lines. The average of the three power values (1.4, 1.6 and 1) used in this analysis was 1.33, which was within 4% of the value used in the correlation (Equation 4.1).

All the experimental data and analysis suggested that the mechanism governing sensor behavior is the drift-diffusion of charged particles between the two sensor electrodes. Charge (current) propogates via collisions of the individual, originally charge neutral particles with the positive high voltage electrode, followed by particle-particle collisions and particle collision with the unbiased signal electrode where electrons are extracted or due to the diffusion of the naturally charged particles in the exhaust towards the signal electrode. Another initiating mechanism for charge transport is the drift of the charged particles due to the applied bias voltage of 1000 V. The presence of a high positive voltage (1000 V) causes the charged particles to move along the electric field lines towards the unbiased signal electrode. Electrons are extracted from the signal electrode when these charged particles reach the signal electrode through any of the above mentioned pathways.

There are other mechanisms that might contribute to the sensor signal. The electric field lines might pull in charged particles from regions surrounding the two sensor electrodes. The sensitivity of the sensor signal to the flow velocity suggests that convective transport of particles and impaction effects might be important. The electric field might induce a dipole on the neutral particles in the exhaust. The charges induced by the electric field on the closest sides of the neighboring particles are of opposite sign. These particles experience an attractive force which can lead to collisions between particles causing agglomeration [42]. This could affect the evolution of particle size and charge distributions between the two sensor electrodes, thereby influencing the current flow between them.

4.3 1-D Drift-Diffusion Model

A 1-D drift-diffusion model was developed to support the hypothesis for charge transport between the two electrodes of the sensor. The governing equation for the model was

$$U\frac{\partial n}{\partial y} = D\frac{\partial^2 n}{\partial x^2} + C_E\frac{\partial n}{\partial x} \tag{4.16}$$

where U is the bulk flow velocity, n is the number concentration of particles, D is the coefficient of diffusion and C_E is the migration or drift velocity in the electric field. The computational domain is shown in Figure 4.27.

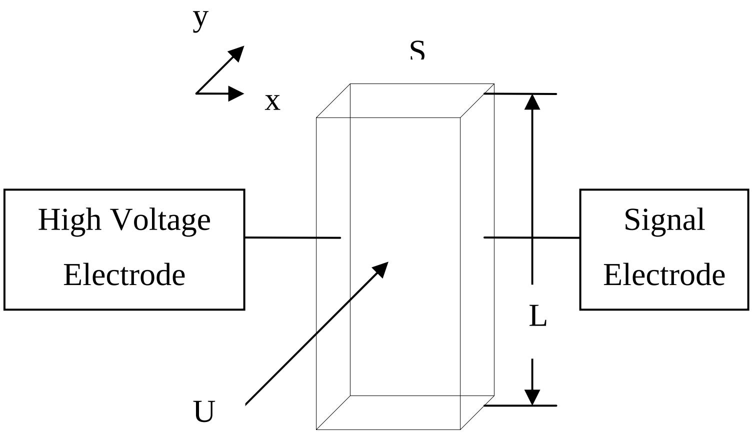

Figure 4.27: Computational domain for the model

The diffusion coefficient is given by the Stokes-Einstein expression

$$D = \frac{kT}{3\pi\mu d_p} \tag{4.17}$$

where k is the Boltzmann constant, T is the temperature of the exhaust, µ is the fluid viscosity, and d_p is the diameter if of the particle [40, 41]. In this model it was assumed that the average diameter of the particles in the exhaust was 100 nm and the viscosity of air was used in Equation 4.17. The drift velocity in the electric field is given by a balance between the force field and the drag on the particle. The force on a particle carrying n_e elementary units of charge in an electric field of intensity E is given by

$$F = n_e eE \tag{4.18}$$

where e is the electronic charge $1.6x10^{-19}$ coulombs [43]. In this model n_e was assumed to be 50, which is a value commonly reported in the literature for cigarette smoke [42]. This is an important assumption. No useful data was available in the literature for charge carried by soot particles in diesel exhaust. The current values predicted by the model scaled as n_e^2, while it's sensitivity to the charge carried by the particles scaled as n_e. Hence the current values predicted by the model will change significantly if a different value is assumed for n_e. It was further assumed that both the naturally charged particles in the exhaust and the neutral particles that collide with the high voltage electrode carry 50 positive elementary charges. Charge exchange between particles due to particle-particle collisions was neglected. A balance between the electrical force and the drag yields a steady migration velocity

$$C_E = \frac{n_e eE}{f} \tag{4.19}$$

where f is the modified Stokes friction coefficient [43]. The modified Stokes friction coefficient is given by

$$f = \frac{3\pi\mu d_p}{C} \tag{4.20}$$

where C is the slip correction factor

$$C = 1 + \frac{2l}{d_p}\left(A_1 + A_2 \exp\frac{-A_3 d_p}{l}\right) \tag{4.21}$$

A_1, A_2 and A_3 are constants and l is the mean free path of the particle. Values of the constants based on experimental measurements of the drag on small particles are $A_1 = 1.257, A_2 = 0.4, A_3 = 0.55$ [43].

A numerical code written by Upadhyay and co-workers [44] was used to solve Equation 4.16. A zero flux boundary condition was imposed on the high voltage electrode since the deposition of positively charged particles on this electrode by drift-diffusion was unlikely. A uniform concentration profile was assumed at the entry to the control volume. Plug flow was assumed through the computational domain and the flow-field effects were neglected. The profile at the exit of the control volume after a residence time determined by the flow velocity was computed using the code. The difference between the two particle concentration profiles gave the number of charged particles deposited on the signal electrode and thus the current. Figure 4.28 shows the current values computed by the model along with the experimentally measured values for an engine speed of 1250 RPM and five different particle concentrations corresponding to engine loads ranging from idle to 90% of full load. The current values predicted by the simple 1-D drift diffusion model are comparable to the experimentally measured values.

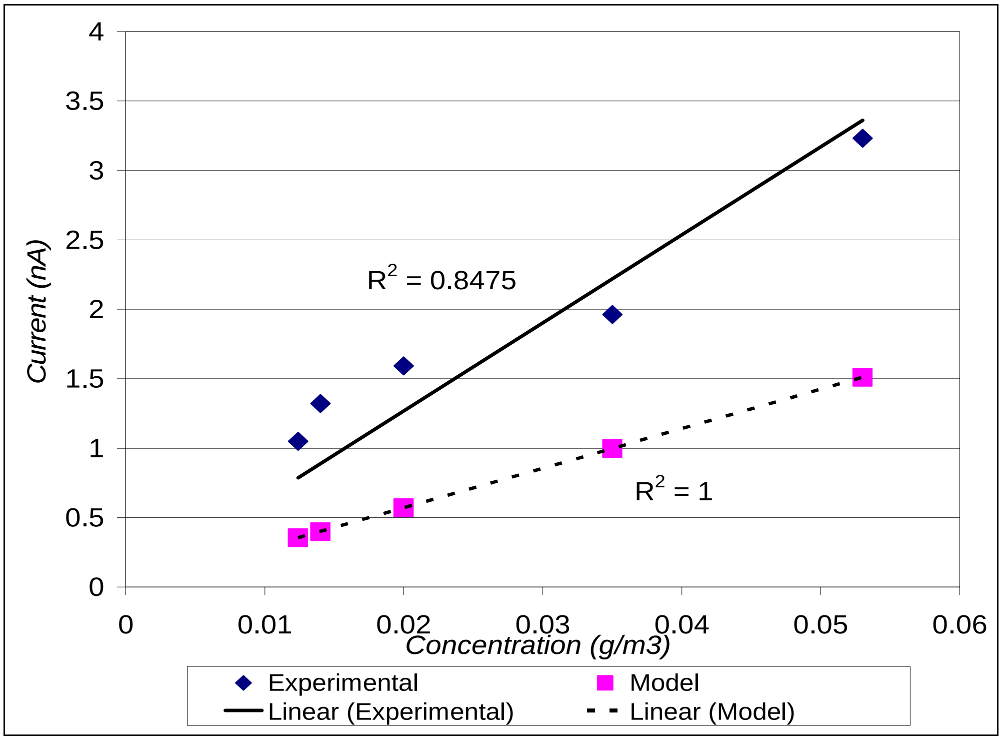

Figure 4.28: Current values predicted by the model and measured experimentally

The model was used to evaluate the effect of electrode spacing on the current between the two electrodes for particle concentration corresponding to 50% of full load at 1250 RPM as shown in Figure 4.29. The spacing between the electrodes had a very weak effect on the current compared to experimental trends.

As discussed earlier the sensor signal was experimentally found to have a power dependence of 1.28 on the electrode spacing.

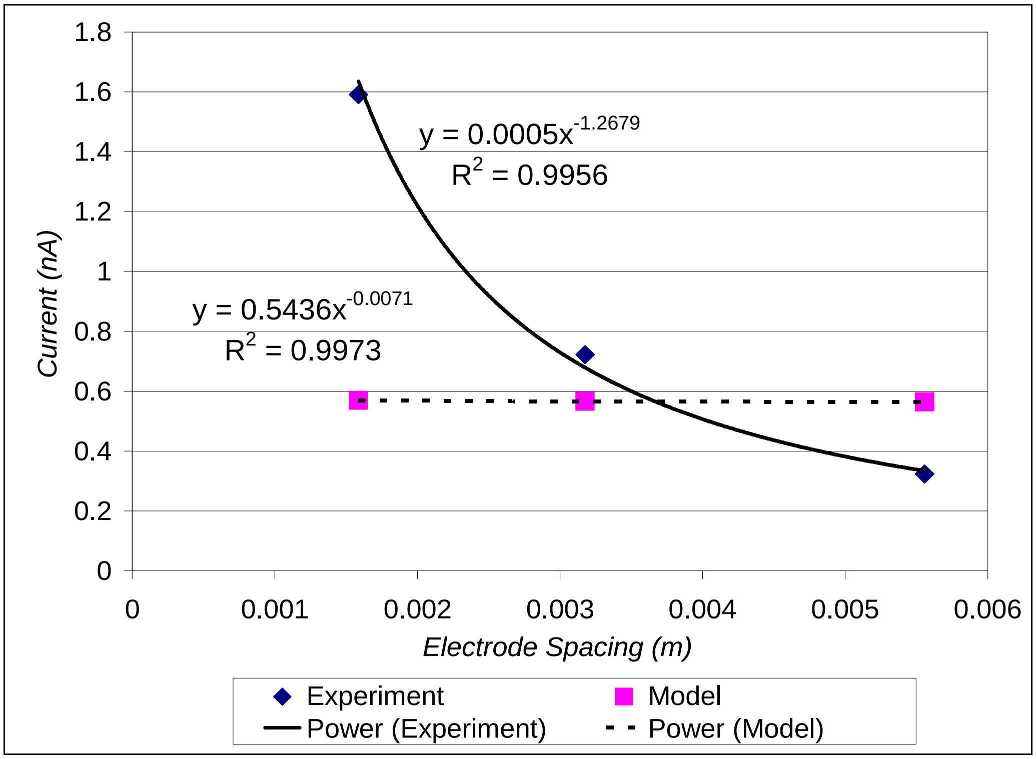

Figure 4.29: Effect of electrode spacing evaluated by the model and measured experimentally at 1250 RPM and 50% of full load

The difference between the model and experimental trends is not exactly clear. One possible reason for this difference could be that the diffusion component in the model is very weak compared to the drift component. External fluid flow effects, which were neglected in this model, might also have some effect on the transport of charged particles between the two sensor electrodes. In the model, the residence time of the particles between the two electrodes decreases with increasing flow velocity resulting in a decrease in the sensor current signal, since the drift or migration velocity is significantly lower than the bulk flow velocity (~0.01 m/s compared to ~5 m/s). Experimentally, it was found that the sensor signal increased exponentially with the bulk flow velocity. This suggests that flow field effects on the sensor signal will have to be considered. Other possible mechanisms discussed earlier could also be important.

Chapter 5: Results and Discussion

This chapter presents the results of experiments done in the exhaust flows of a single cylinder diesel engine and a steady-state acetylene diffusion flame. Steady-state measurements in engine exhaust were done over a range of speed and load conditions while transient measurements were performed during engine starts and accelerations. The sensor output was compared to gravimetric filter measurements, a light-scattering nephelometer and an aerodynamic particle sizer.

5.1 Acetylene Flame

The sensor was tested in the PM laden exhaust of a steady-state acetylene diffusion flame. Figure 5.1 shows the output of a typical sensor for increasing height of the acetylene flame in the flow tunnel. Only a few seconds of data are shown for clarity. The sensor signal increased with increasing flame height. The sensor was able to resolve the differences in particle concentration for the different flame heights which varied from about 2 to 8 cm. Large spikes were observed in the sensor signal for high flow rates of acetylene, and are thought to be the result of intermittent interaction with the highly agglomerated particles that were visually observed in the flow at high flame heights.

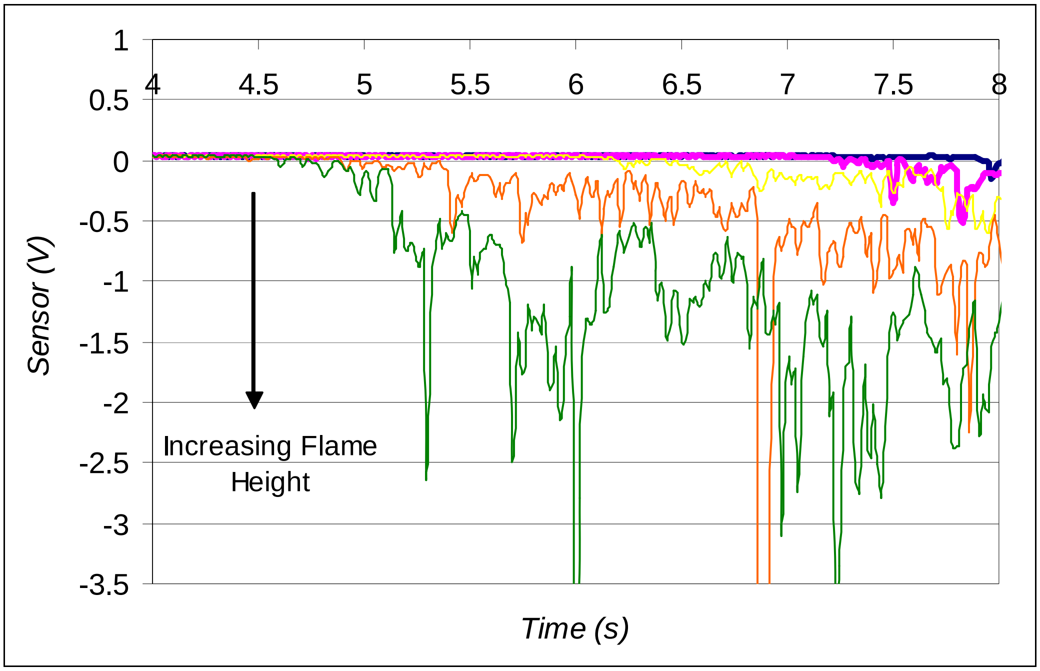

Figure 5.1: Sensor output for different flame heights in flow tunnel

Figure 5.2 shows the output of the sensor for a pulsed acetylene flame. The rotameter, used to control the flow rate of acetylene, was alternatively set to full-scale reading for 4-5 seconds and then to zero-level for 2-3 seconds. This process was repeated for approximately one minute. The sensor reacted to the increase in particle concentration when the rotameter was set to full-scale reading and returned to the zero-baseline level when the flow of acetylene was reduced to near zero levels. The sensor signal was steady at about -1.5 V, while the rotameter was set to full-scale reading, as shown in Figure 5.3. It could resolve the transient fluctuations in particle concentration.

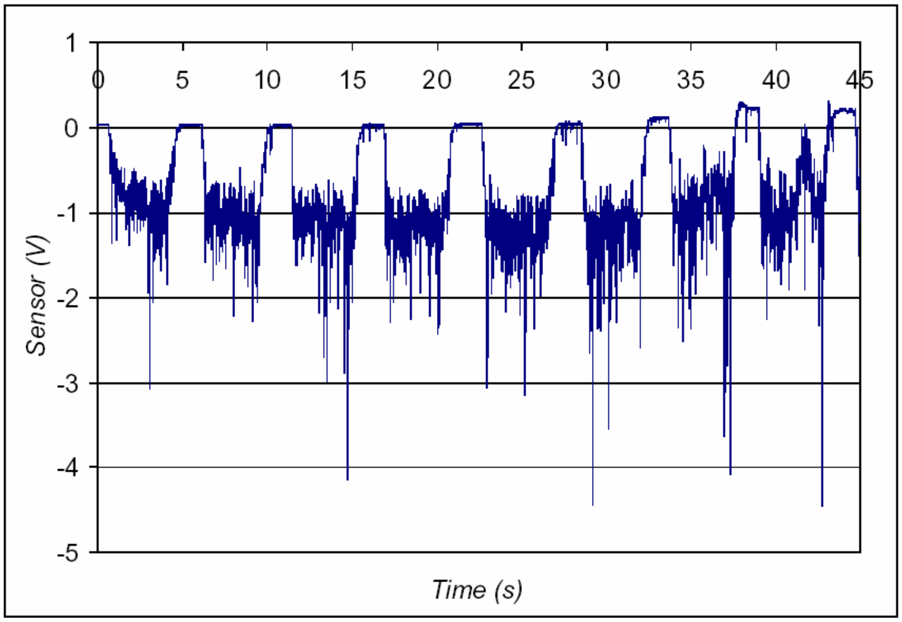

Figure 5.2: Sensor output for a pulsating acetylene flame

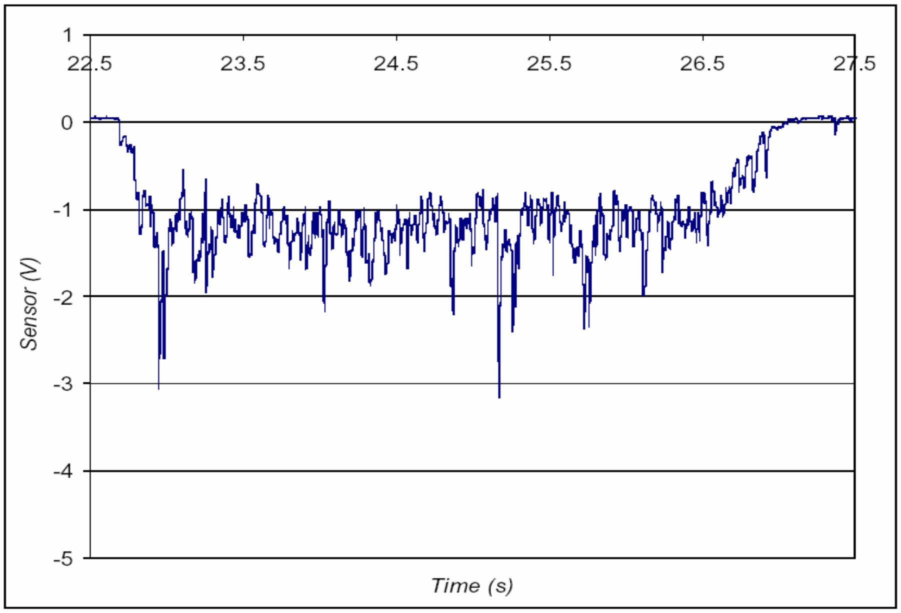

Figure 5.3: Sensor output when the rotameter is set to full-scale reading

5.2 Diesel Engine

5.2.1 Transient Measurements

The sensor was tested in the exhaust of the single cylinder diesel engine. Transient measurements with the sensor were performed during engine starts and accelerations. Opacity meter and sensor response were recorded for over a hundred engine starts and accelerations. Figure 5.4 shows the output of a typical sensor and exhaust opacity for an engine start followed by two accelerations. The sensor response compares very well with exhaust opacity. The relative heights of the peaks are different for the opacity meter and the electronic sensor because unlike the sensor the opacity meter is sensitive to all components of PM. Unlike the data presented in Figure 3.17, there is no phase difference between the opacity meter and the sensor, since both are installed in the main exhaust system.

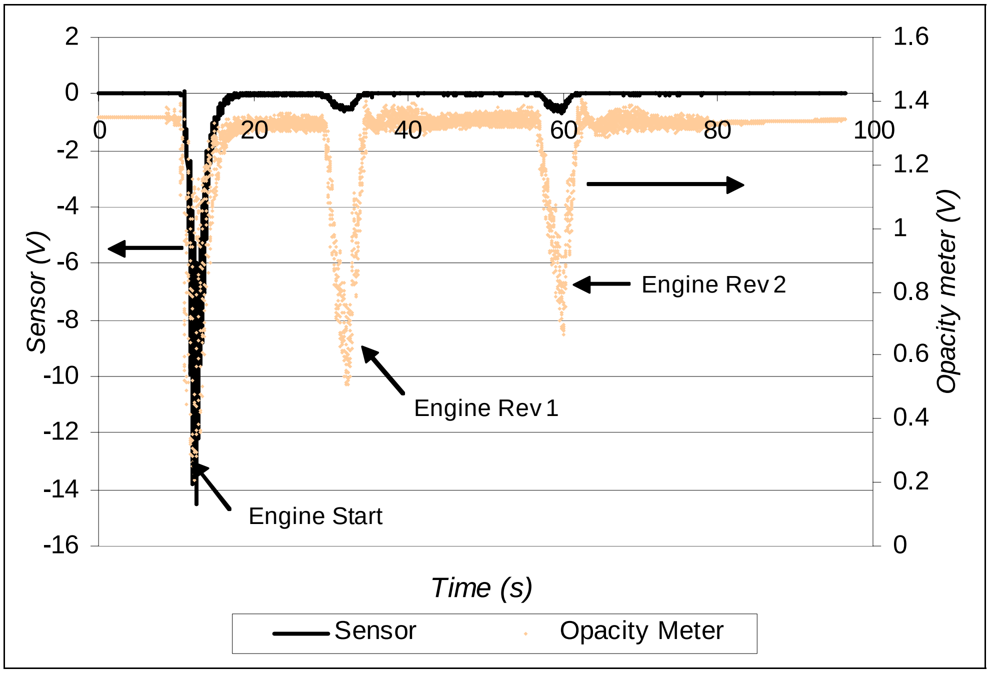

Figure 5.4: Sensor output and exhaust opacity for an engine start followed by two accelerations

Figure 5.5 shows the response of the sensor and the exhaust opacity for a typical engine start-up. The PM emissions from the engine were much greater during the first 5 s of start-up than for either acceleration transients or for steady state operation at any speed/load condition. The sensor output correlates very well with the opacity measurements. The periodic oscillations in the signals result from the purge air of the opacity meter clearing the exhaust pipe between exhaust events. The phase difference between the two signals is a function of the distance between the two sensors, and the purge-air flow rate. At high purge-air flow rates the oscillations came into phase with each other as shown in Figure 5.6.

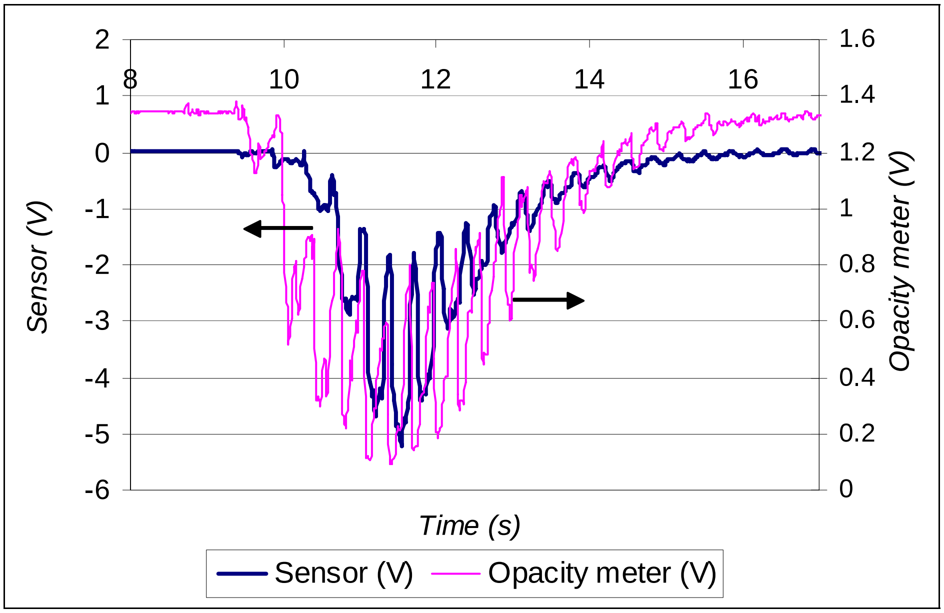

Figure 5.5: Sensor and opacity during engine start-up

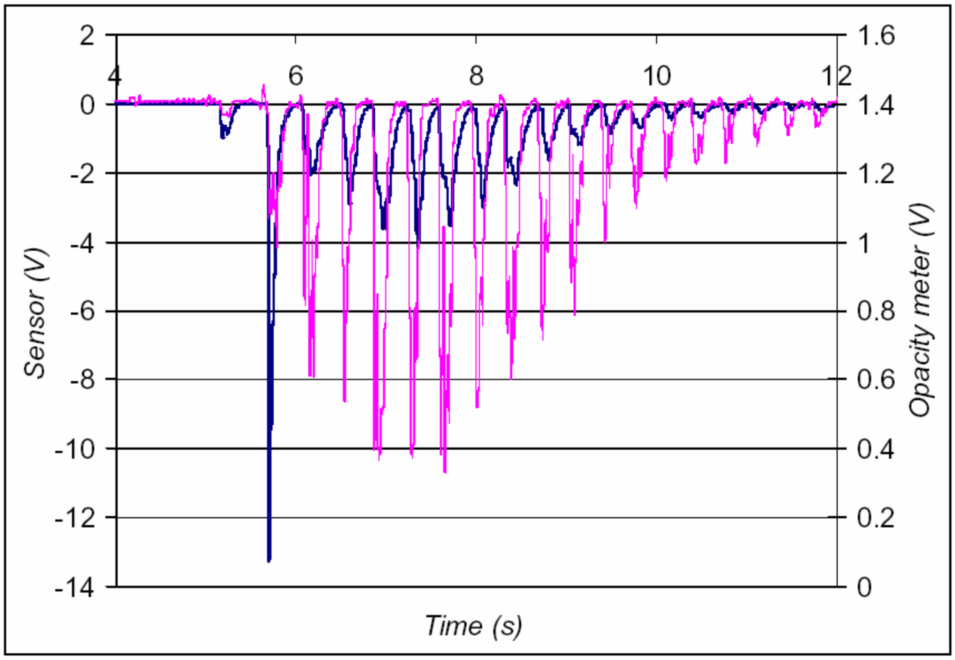

Figure 5.6: Sensor and opacity for high flow-rate of purge air

5.2.1 Steady-State Measurements

Steady-state measurements with the sensor were performed at a constant engine speed of 1250 RPM while the load was varied to change the level of particulate matter in engine exhaust. Tests were performed at five load conditions ranging from idle to 90% of full load. At each load condition the engine was allowed to stabilize for 30-45 seconds. The sensor signal was then recorded for one minute. Simultaneously an exhaust sample was drawn through the filter paper by a vacuum pump to correlate the sensor signal to the mass of particulates accumulated on filters. While the recording of the sensor output was stopped after one minute, exhaust was allowed to pass through the filter for five minutes to ensure sufficient accumulation. At the end of each day of testing the filter papers were heated on electrical hot plates for 24 hours to evaporate water and soluble organic fractions (SOF). Since the sensor is sensitive to only to the carbonaceous fraction of particulate matter, it was necessary to remove the SOFs from the filter so that the sensor signal could be correlated to only the carbonaceous component of particulate matter. At least three separate runs were performed at each load condition on different days. Figure 5.7 and 5.8 show the output of two typical sensor designs for the five load conditions at a constant engine speed of 1250 RPM. The sensor was able to resolve the differences in particle concentration for increasing load. There was greater variation in the sensor signal at the high load condition compared to operation at low and medium loads. The sensor reacted to the change in load imposed at the end of each run and went back to its baseline level once the engine was shut off.

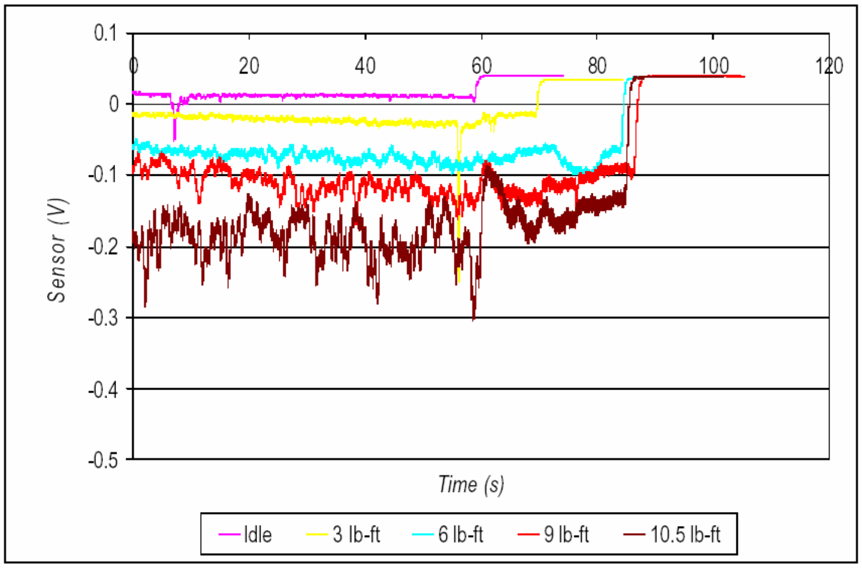

Figure 5.7: Sensor output of a typical geometry for increasing engine load at a constant speed of 1250 RPM

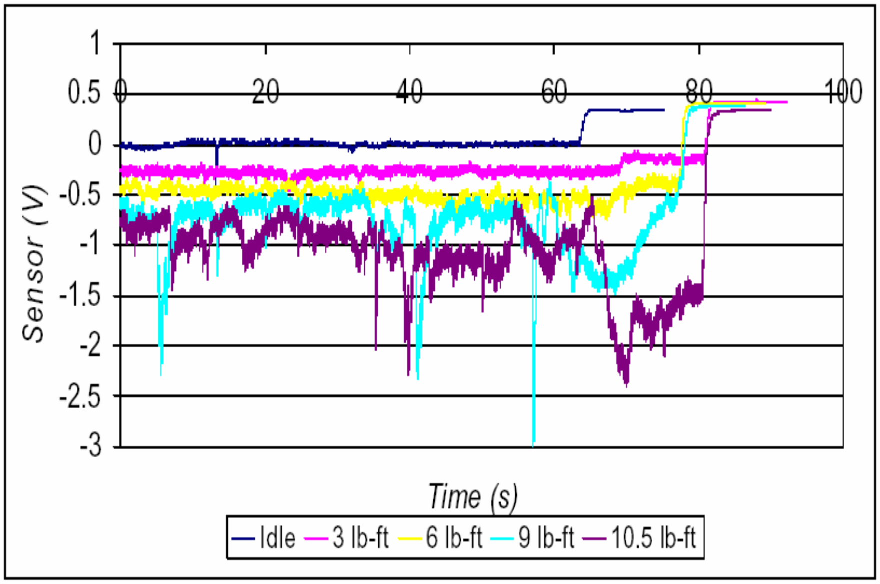

Figure 5.8: Sensor output of another design for increasing engine load at a speed of 1250 RPM

Figures 5.9, 5.10, 5.11, 5.12 and 5.13 show the absolute value of the mean sensor signal, calculated over a one minute interval, along with the filter mass loading expressed in g/m^3 for multiple runs under the five load conditions ranging from idle to 90% of full load. The filter mass loading values have been multiplied by a factor of 30 to represent them on the same scale as the sensor. The sensor signal is very reproducible at low and medium loads. There was somewhat greater run-to-run variation in the signal under high load operation. The standard deviation of the mean sensor signal normalized by its mean value was about +/- 14% for the runs. The variation in the filter measurements was about +/- 7%.

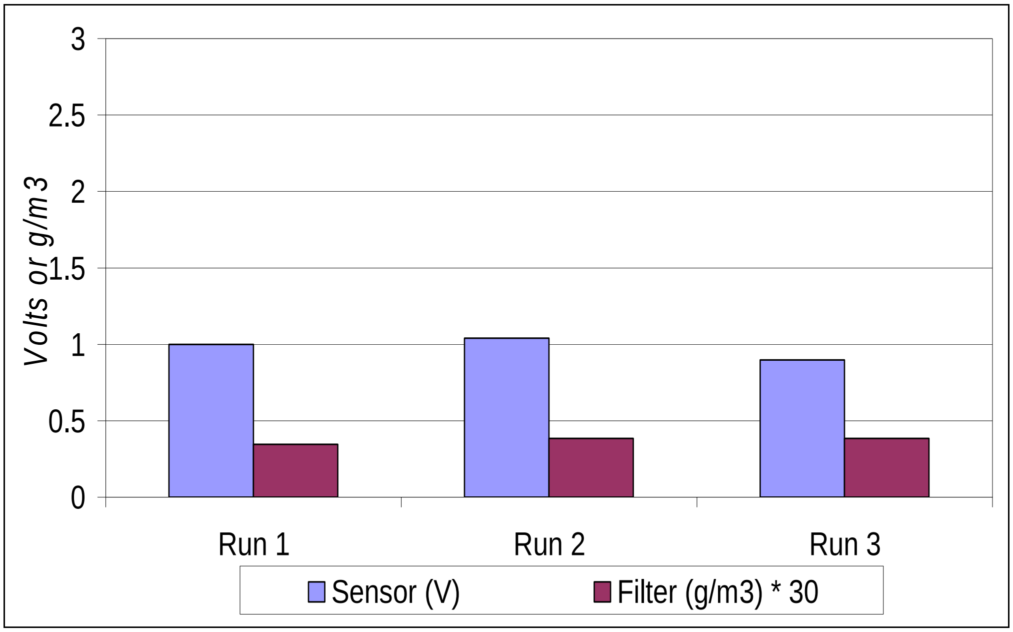

Figure 5.9: Reproducibility of sensor signal and filter mass loading at engine idle

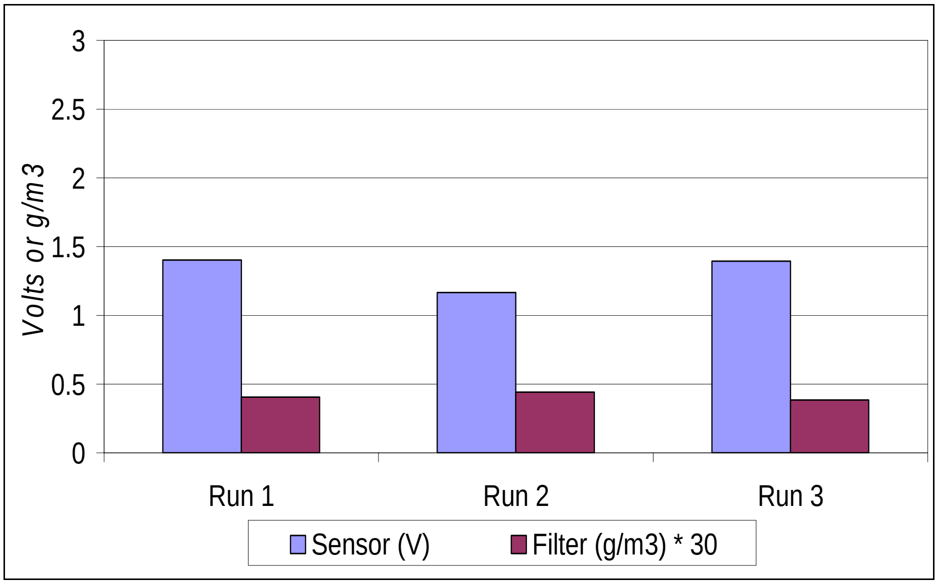

Figure 5.10: Reproducibility of sensor signal and filter mass loading at 25% of full load

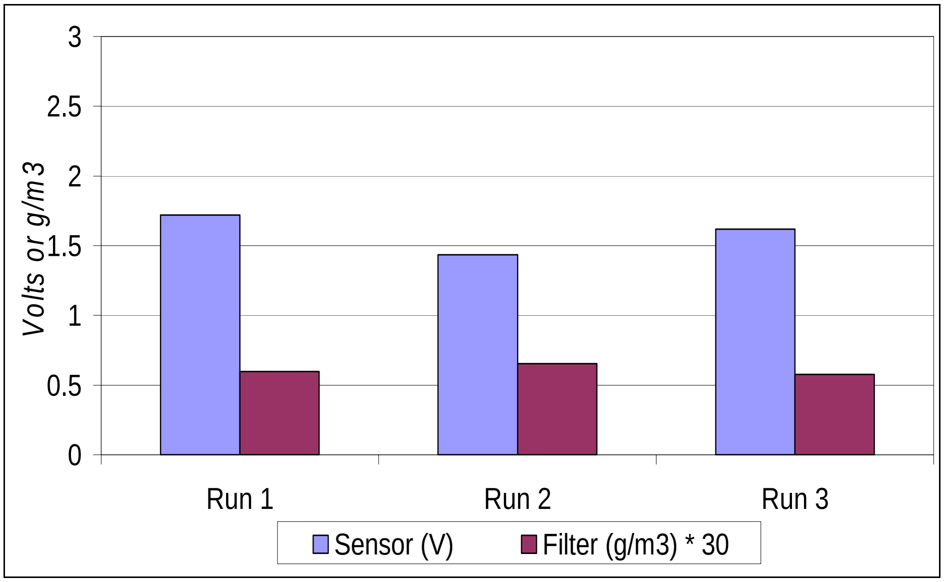

Figure 5.11: Reproducibility of sensor signal and filter mass loading at 50% of full load

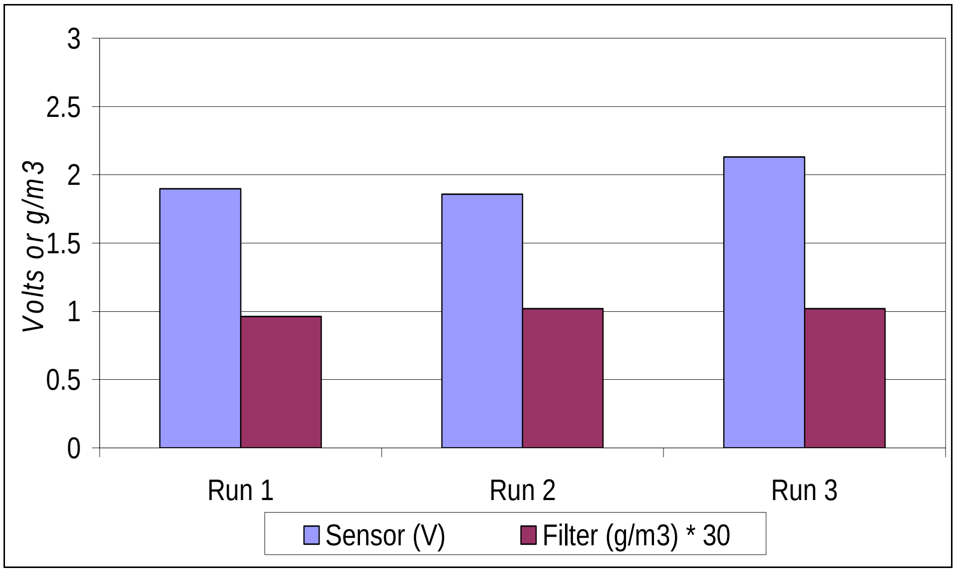

Figure 5.12: Reproducibility of sensor signal and filter mass loading at 75% of full load

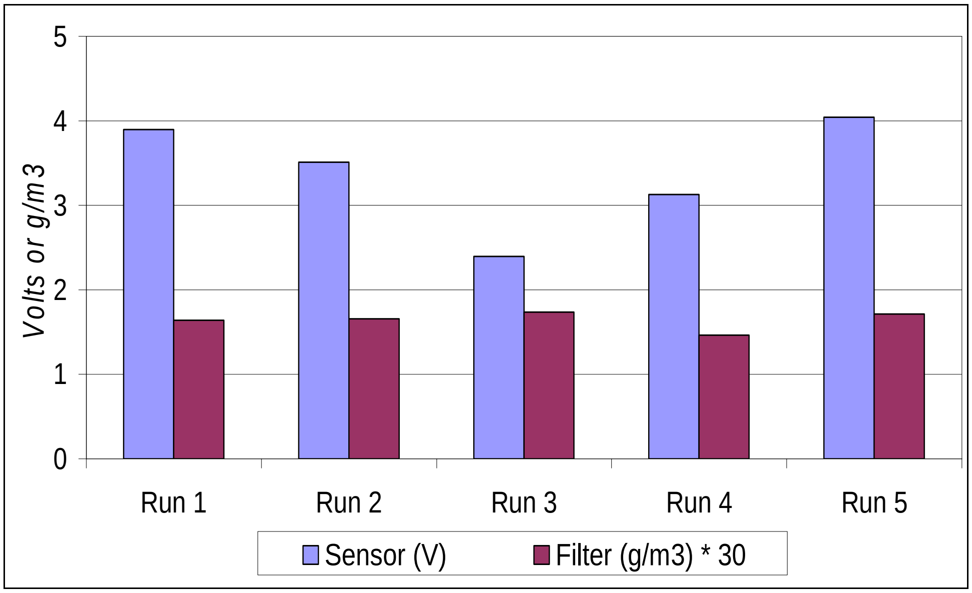

Figure 5.13: Reproducibility of sensor signal and filter mass loading at 90% of full load

Figure 5.14 presents the data averaged over all the runs, showing the absolute mean sensor output and the mean filter mass for increasing load at a constant speed of 1250 RPM. The error bars represent +/- 1 standard deviation. The filter mass loading values have been multiplied by a factor of 30 for representation. Overall, a good correlation between the sensor and filter mass is observed. Both the filter loading and the sensor signal increase with increasing load. The lowest PM levels measured were at engine idle where the PM concentration was about 0.01 g/m^3. This level is still well above the noise level of the sensor so lower PM levels are resolvable.

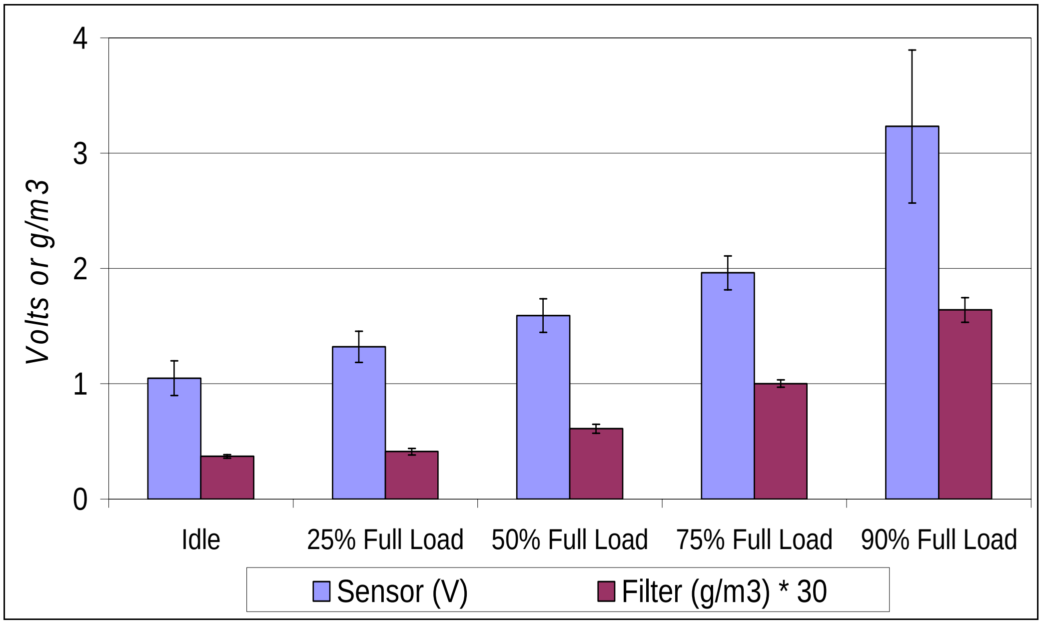

Figure 5.14: Summary of mean sensor output and mean filter mass loading for different loads at a constant engine speed 1250 RPM

Figure 5.15 shows the absolute mean sensor output as a function of the filter mass loading along with a least squares fit to the data that was forced through zero. Overall a good correlation is observed between the sensor and the filter mass loading with an R^2 value of 0.85.

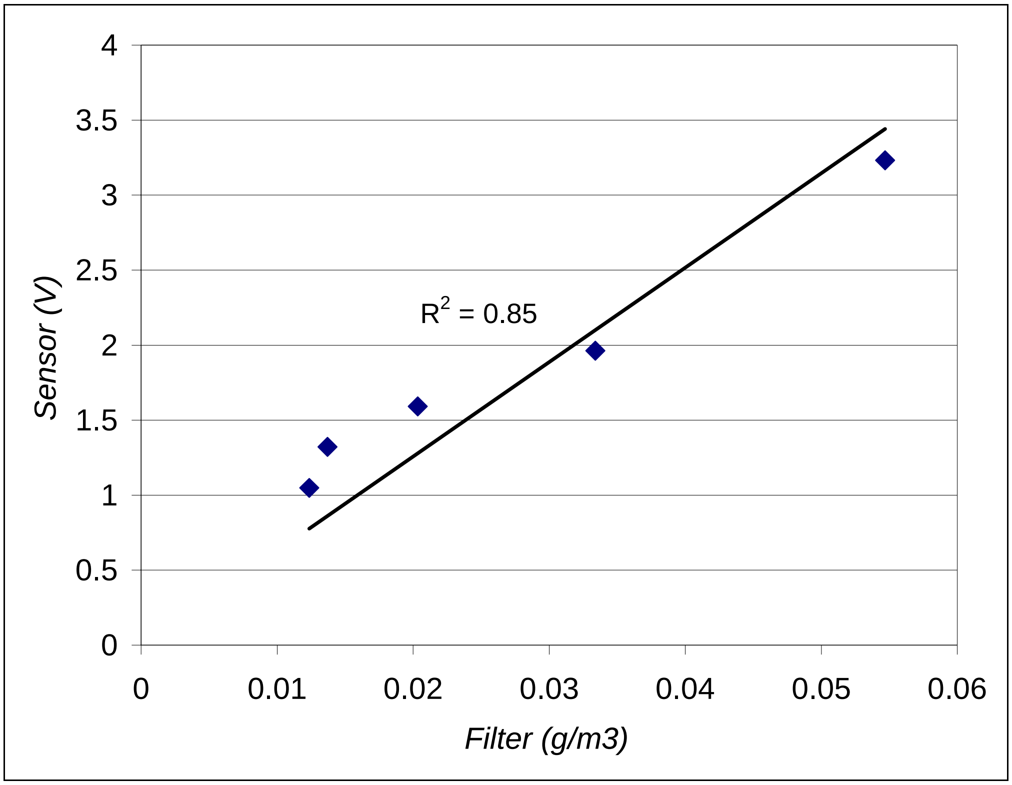

Figure 5.15: Correlation between the mean sensor output and filter mass loading

It was observed that there was a very small increase in the mass loading, as determined by the filter measurements, when the load was increased from idle to 25% of full load. The filter papers used to collect an exhaust sample at 25% of full load were visibly 'darker', indicating a greater accumulation of carbonaceous particles, than the filters used at engine idle. Yet the average difference in their weights was less than 9%. A photograph of the two filters is shown in Figure 5.16. There was no change in the weights of the filters even after heating them continuously for 48 hours.

Figure 5.16: Photograph of filters used at idle and 25% of full load

There was a significant difference between the heated and the unheated filters as shown in Figure 5.17. Figure 5.17 presents data averaged over at least three different runs at each load condition. The error bars represent +/- 1 standard deviation. Heating the filters for 24 hours removed most of the SOFs and sulfates accumulated on the filters. The unheated filters were allowed to dry for 24 hours before weighing, which allowed the moisture on the filters to evaporate but not the SOFs and sulfates. The average difference in the weights of the unheated filters used at engine idle and 25% of full load was about 39%, which was much greater than the average weight difference of 9% between heated filters used at the same two load conditions.

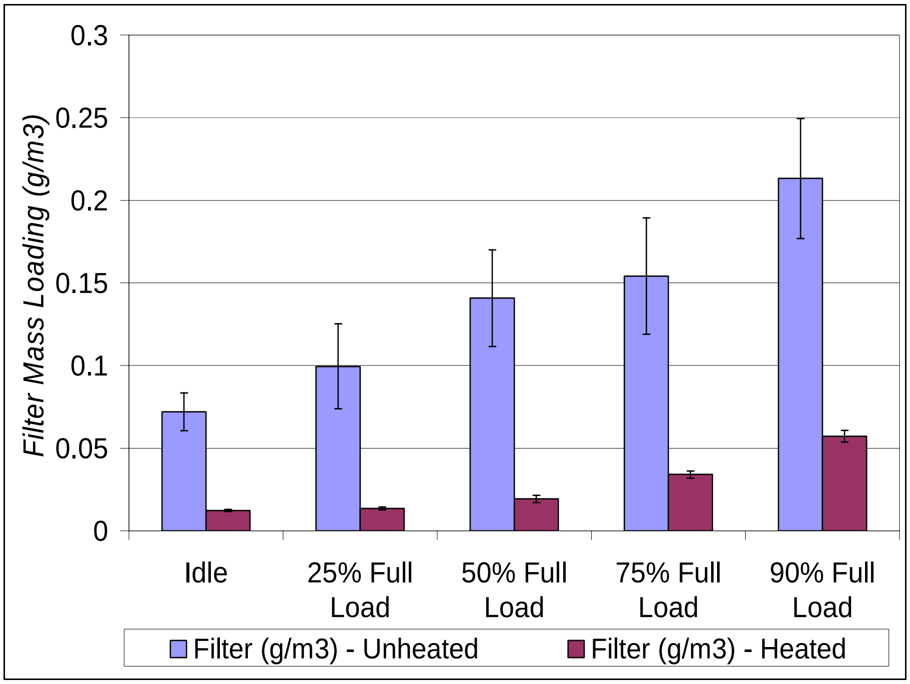

Figure 5.17: Difference between heated and unheated filters at five load conditions

The chemical composition of the filters used at all five load conditions was analyzed using Energy Dispersive X-ray Spectroscopy to estimate the accumulation of carbon. Energy dispersive x-ray spectroscopy (EDS) is a chemical microanalysis technique performed in conjunction with a scanning electron microscope (SEM). The technique utilizes x-rays that are emitted from the sample during bombardment by the electron beam to characterize the elemental composition of the analyzed volume. Features or phases as small as about 1µm can be analyzed. When the sample is bombarded by the electron beam of the SEM, electrons are ejected from the atoms comprising the sample's surface. A resulting electron vacancy is filled by an electron from a higher shell, and an x-ray is emitted to balance the energy difference between the two electrons. The EDS x-ray detector measures the number of emitted x-rays versus their energy.

The energy of the x-ray is characteristic of the element from which the x-ray was emitted. A spectrum of the energy versus relative counts of the detected x-rays is obtained and evaluated for qualitative and quantitative determinations of the elements present in the sampled volume. Figure 5.18 shows the spectra obtained for the filters used at all five engine load conditions, an unused ‘blank’ filter and a carbon tape for comparison. It can be seen from the spectra that the amount of carbon accumulated on the filters increased with engine load, which supports the increase in sensor signal. Hence, it is believed that the heating process did not evaporate all the SOF and sulfate components at engine idle. As a result, though there was an increase in the carbonaceous fraction from idle to 25% of full load as per the EDS measurements, the filter weights did not vary significantly.

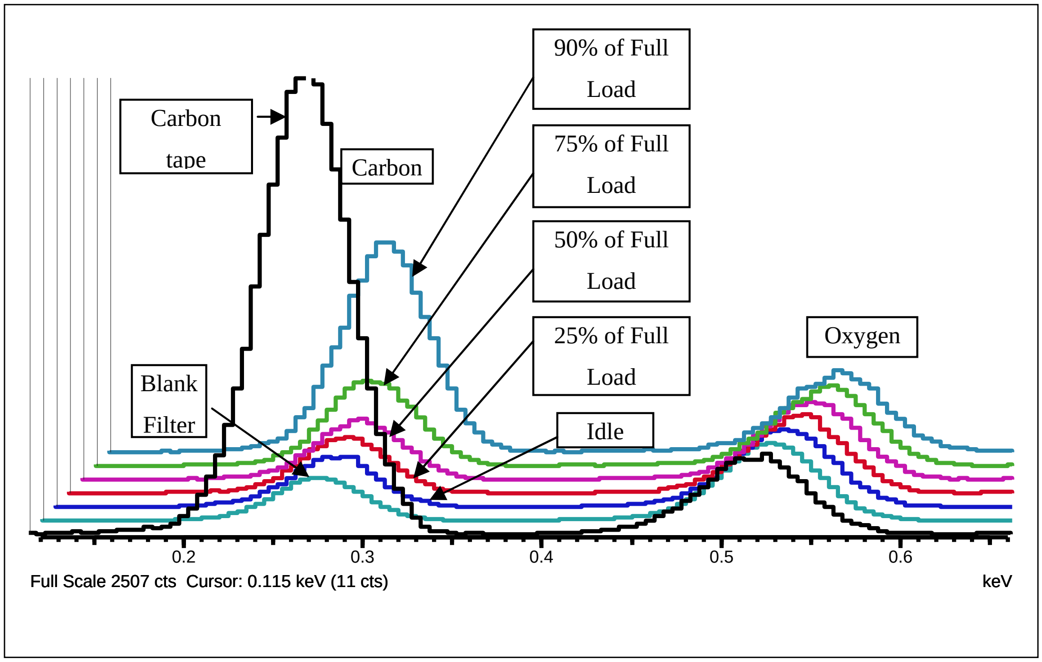

Figure 5.18: EDS spectra for filters at the five engine load conditions

Figure 5.19 shows the SEM photo of a particle deposited on the filter paper during idling. The strands of the filter paper are clearly visible in the background. A line scan was done to determine the elemental composition of the particle as shown in Figure 5.20 and Figure 5.21. It was observed that the particle was composed of both carbon and a significant amount of sulfur. The sulfur content of the particles is derived from the sulfur present in the diesel fuel. The diesel fuel used in the study had about 500 ppm of sulfur.

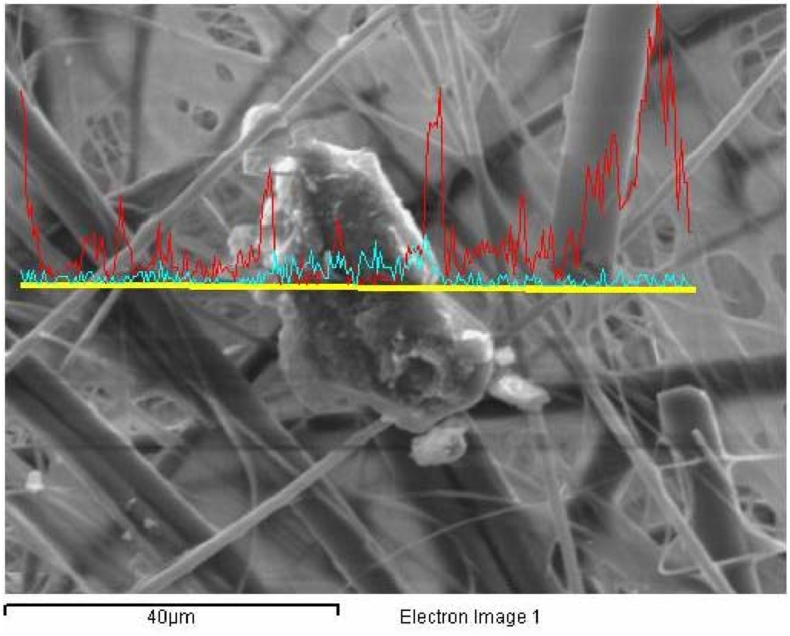

Figure 5.19: SEM photo of a particle deposited on the filter paper

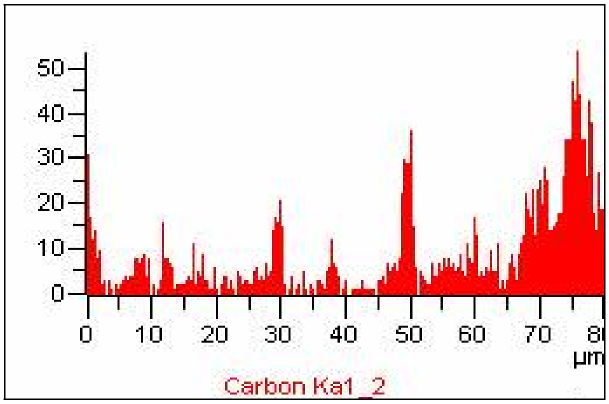

Figure 5.20: Carbon composition along the yellow line

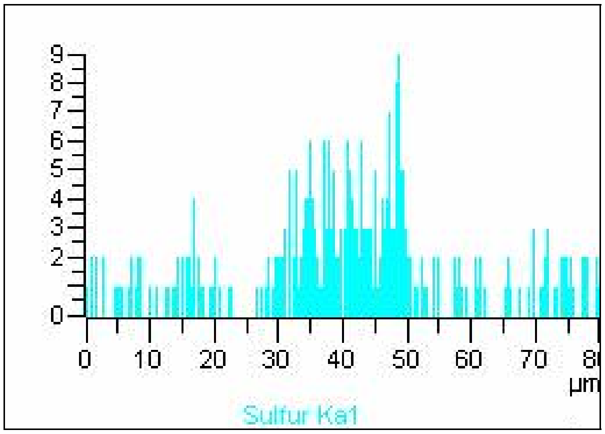

Figure 5.21: Sulfur composition along the yellow line

5.2.3 Crank-Angle Resolved Measurements

To measure the crank-angle resolved response of the sensor experiments were performed at three engine speeds of 1250, 1500 and 2000 RPM at idle. Figures 5.22 and 5.23 show the output of the sensor for 1 second at two engine speeds of 1250 and 2000 RPM. The sampling rate of the data acquisition device was set to 5 ms. It was observed from the data that the sensor was reacting once per engine cycle i.e. during every exhaust stroke.

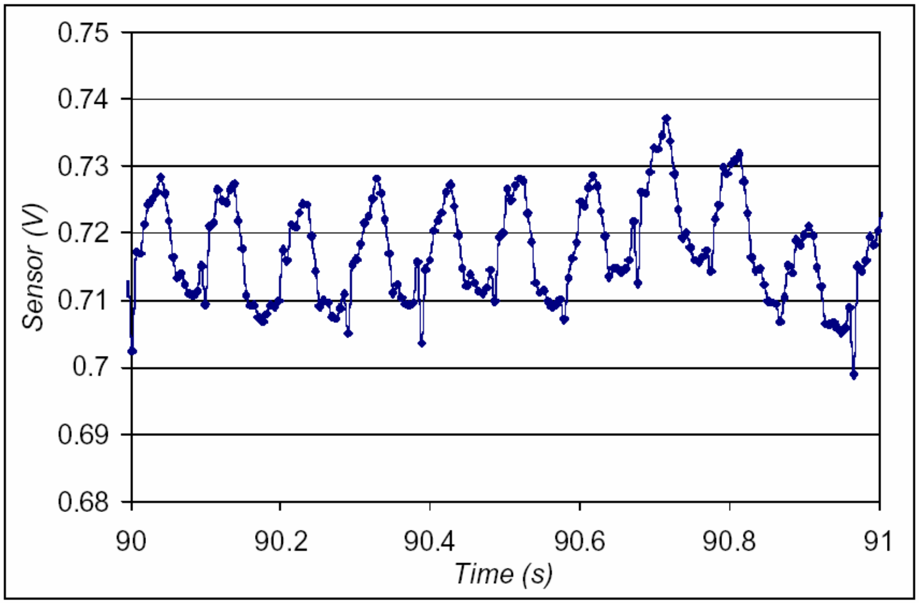

Figure 5.22: Sensor output for 1 second at 1250 RPM

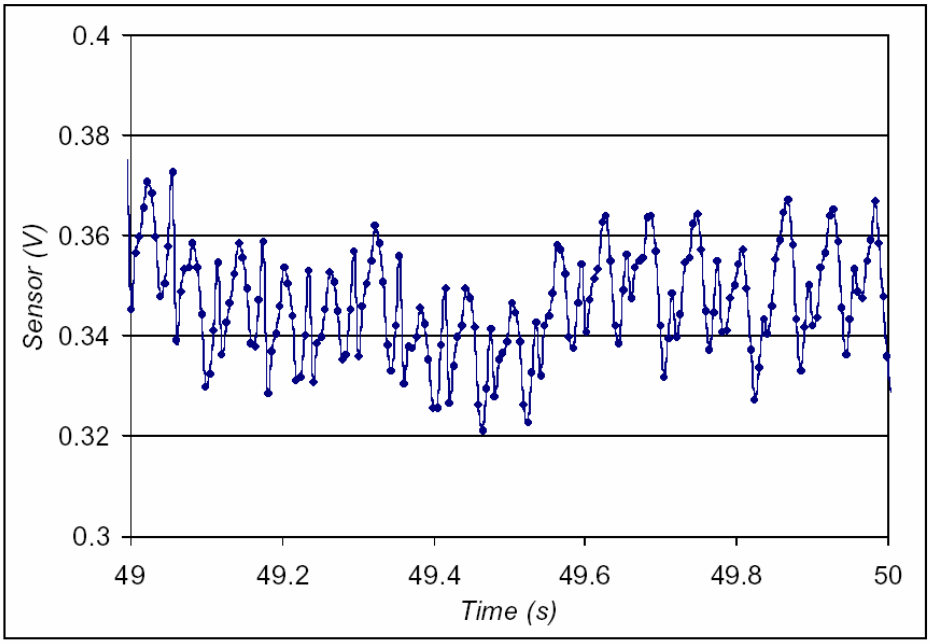

Figure 5.23: Sensor output for 1 second at 2000 RPM

To correlate the sensor signal with the crank angle position a phototransistor optical interrupter switch was installed. A small piece of metal shim stock was attached to the pulley, connected to the engine crankshaft, at approximately top dead center (TDC) of exhaust. The output signal of the switch was recorded with the data acquisition system along with the sensor and opacity meter. The sampling rate was set to 1 ms. The engine was run at a speed of 1250 RPM and 75% of full load to produce sufficient particle concentrations. A sampling rate of 1 ms corresponds to 7.5 crank-angle degrees at 1250 RPM. Figure 5.24 shows the crank-angle resolved output of a typical sensor, opacity meter and the optical switch for one engine cycle. The sensor output is reported in terms of mass loading (g/m^3) based on the correlation (Equation 4.2).

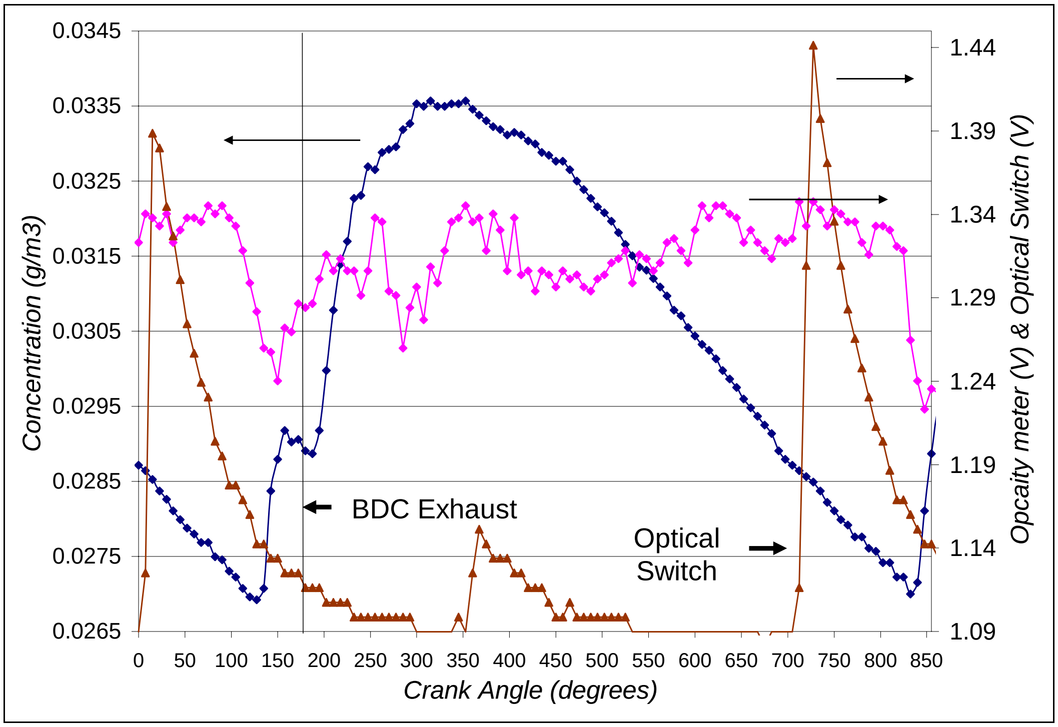

Figure 5.24: Crank-angle resolved output of the sensor, opacity meter and optical switch for one engine cycle

It was observed from the data that the sensor could resolve the differences in concentration during exhaust blow-down and during the exhaust stroke. The sensor output correlated well with exhaust opacity. It is believed that the useful part of the signal is till the TDC of exhaust. It is expected that the purge air supplied to the opacity meter clears out most of the particles in between exhaust events. The sensor output after TDC of exhaust decreased gradually to an intermediate level until the next exhaust event. This gradual decrease in the sensor signal after TDC of exhaust could be due to the sensitivity to the flow velocity and not due to variations in particle concentration. Wagner and co-workers [45] reported crank-angle resolved 'smoke' or particle density measurements for a four cylinder diesel engine using a Diesel Particle

Scatterometer (DPS) as shown in Figure 5.25. The photomultiplier voltage is effectively a measure of 'smoke' or particle density. Particulates from each cylinder event can be clearly seen.

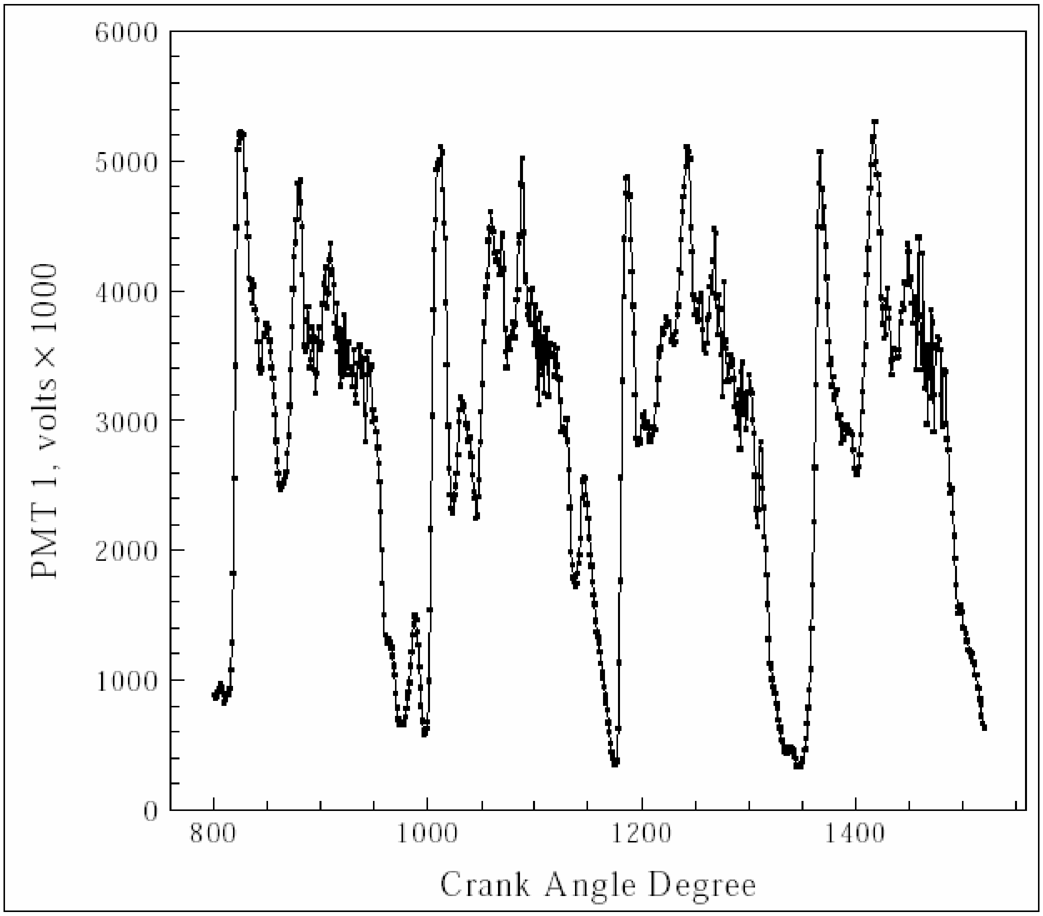

Figure 5.25: Crank-angle resolved signal from the DPS [45]

There are differences between the sensor signal and their data. They observed a sharp peak in particle density during blow-down followed by an increase in particle density during the exhaust stroke. The opacity meter on the other hand had a similar response during blow-down, but not during the rest of the exhaust stroke. It was expected that the crank-angle resolved response of both instruments would be similar though the engines used in the tests were quite different. The reasons for the differences between both measurements are not clearly understood.

Figure 5.26 shows the crank-angle resolved output of the sensor, opacity meter and the optical switch over an engine cycle for a high flow-rate of purge air, which was used to keep the optics of the opacity meter clean. The sensor signal was similar to Figure 5.24. Though the opacity meter returned to its baseline level in between exhaust events, the sensor signal did not return to the baseline level but decreased gradually to an intermediate level. The signal magnitude was somewhat lower due to dilution by the purge air.

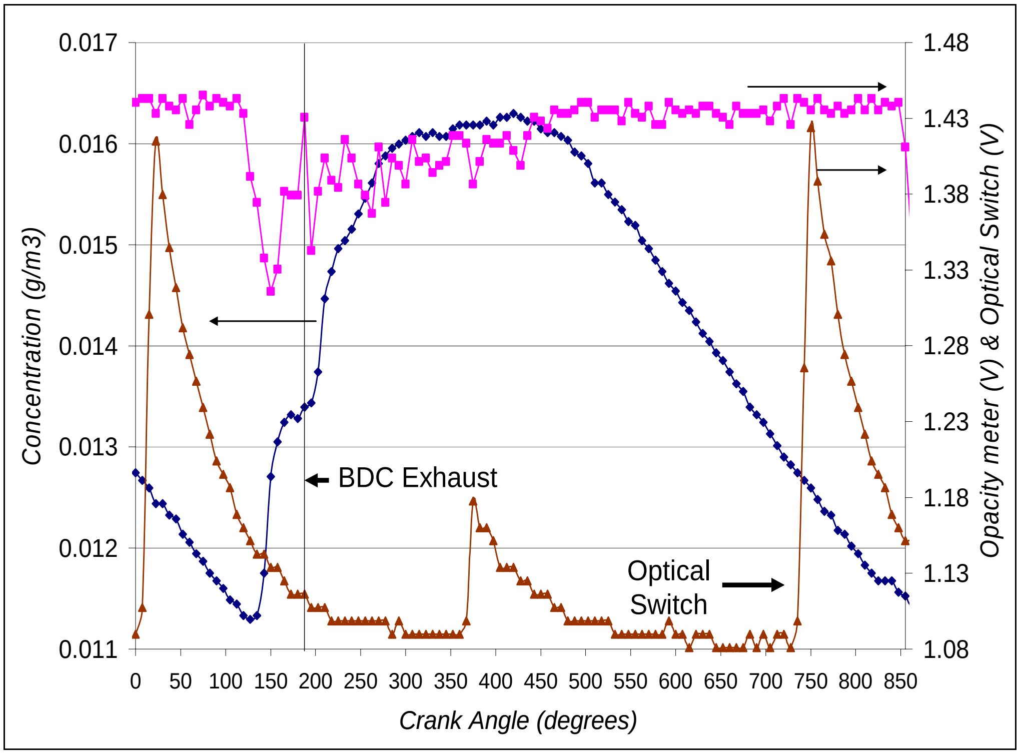

Figure 5.26: Crank-angle resolved output of the sensor, opacity meter and optical switch for one engine cycle with high purge air flow rate

Figure 5.27 shows the output of the sensor and a pressure transducer mounted in the exhaust manifold. The exhaust blow-down event can be clearly observed from the pressure transducer signal. A good correlation was observed between the sensor and the pressure transducer during blow-down, indicating that the signal phasing with crank-angle was correct.

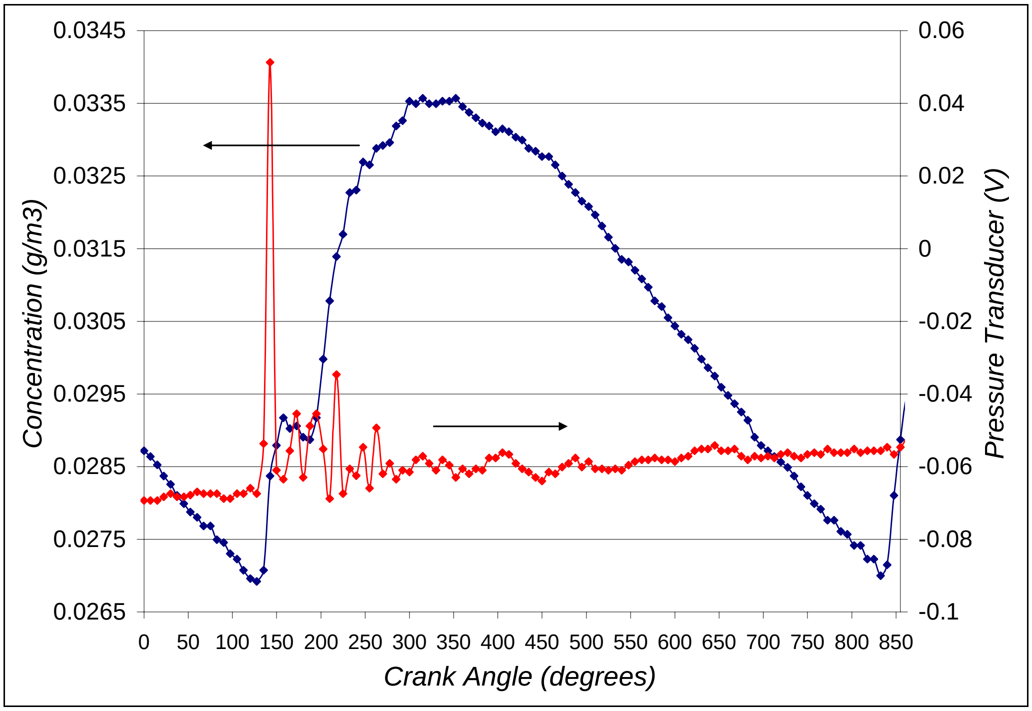

Figure 5.27: Crank-angle resolved output of the sensor and pressure transducer signal for one engine cycle

5.3 Nephelometer Comparison

The sensor output was compared to a light scattering nephelometer. The nephelometer, developed at The University of Texas at Austin, is capable of real-time measurement of PM emissions from direct-injection spark-ignition and diesel engines. While the sensor detects the concentration of carbonaceous particles, the nephelometer measures the mean size and mass loading of all particulate matter i.e. carbonaceous fraction, SOFs and sulfates in real time. It was thus interesting to compare the mass loadings measured by both instruments in diesel engine exhaust. Figure 5.28 shows the output of the sensor, the mass loading determined from unheated filters and the PM concentration measured by the nephelometer at 1250 RPM and five load conditions ranging from idle to 90% of full load. Mass loading data from unheated filters was used because the nephelometer, as mentioned before, detects not only the carbonaceous fraction but SOF's and sulfates as well. Multiple runs were done to ensure repeatability. The error bars represent +/- 1 standard deviation. The sensor signal has been multiplied by 0.2 for representation.

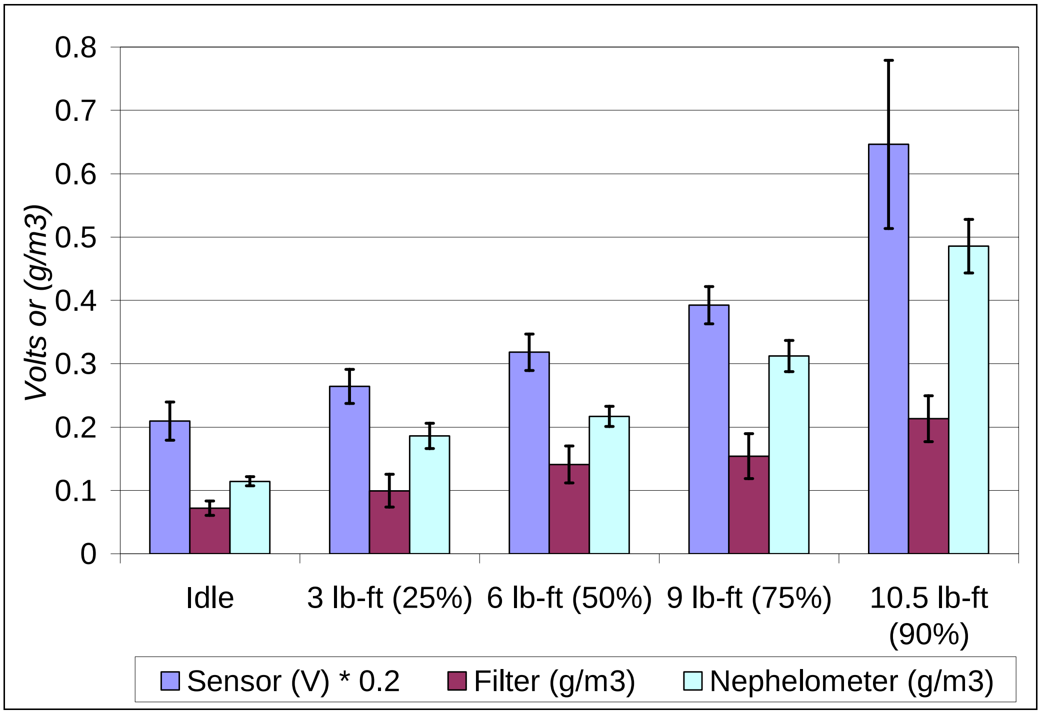

Figure 5.28: Sensor output and mass loading measured by unheated filters and nephelometer for five engine load conditions at 1250 RPM

Similar trends were observed in the sensor signal and the nephelometer measurements. Both the sensor signal and the mass loadings measured by the nephelometer increased with engine load. Figure 5.29 shows the absolute mean sensor output as a function of the PM concentration measured by the nephelometer along with a least squares fit to the data that was forced through zero. Overall a good correlation is observed with an R^2 value of 0.96. The linear dependence of the sensor signal on concentration is consistent with the correlation (Equation 4.1).

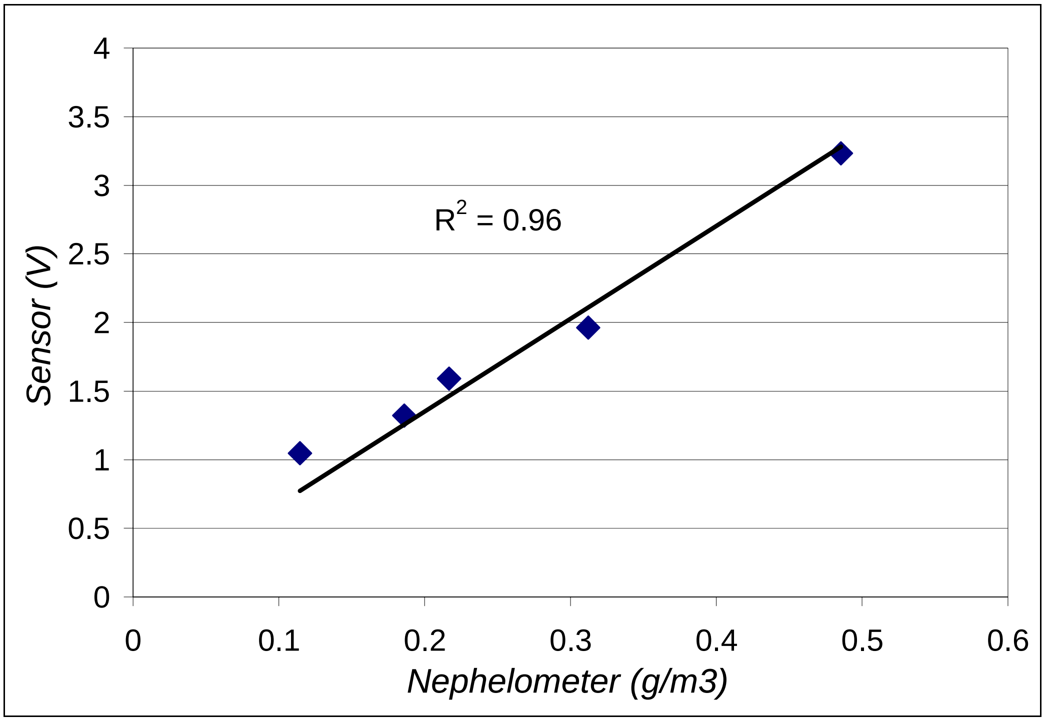

Figure 5.29: Correlation between sensor output and mass loading measured by nephelometer

The PM concentrations determined by the filters and the nephelometer exhibited similar trends but varied quantitatively. Of all the species in the exhaust, PM emissions are the most difficult to measure accurately. Particulate concentrations are affected by both the measurement and sampling techniques.

The quantitative variations between the filter and nephelometer mass loading may, thus, be due to the different measurement techniques.

The sensor signal was converted to concentration data using the correlation discussed before (Equation 4.2). The data are shown in Figure 5.30 along with the mass loadings determined by the nephelometer and the unheated filters.

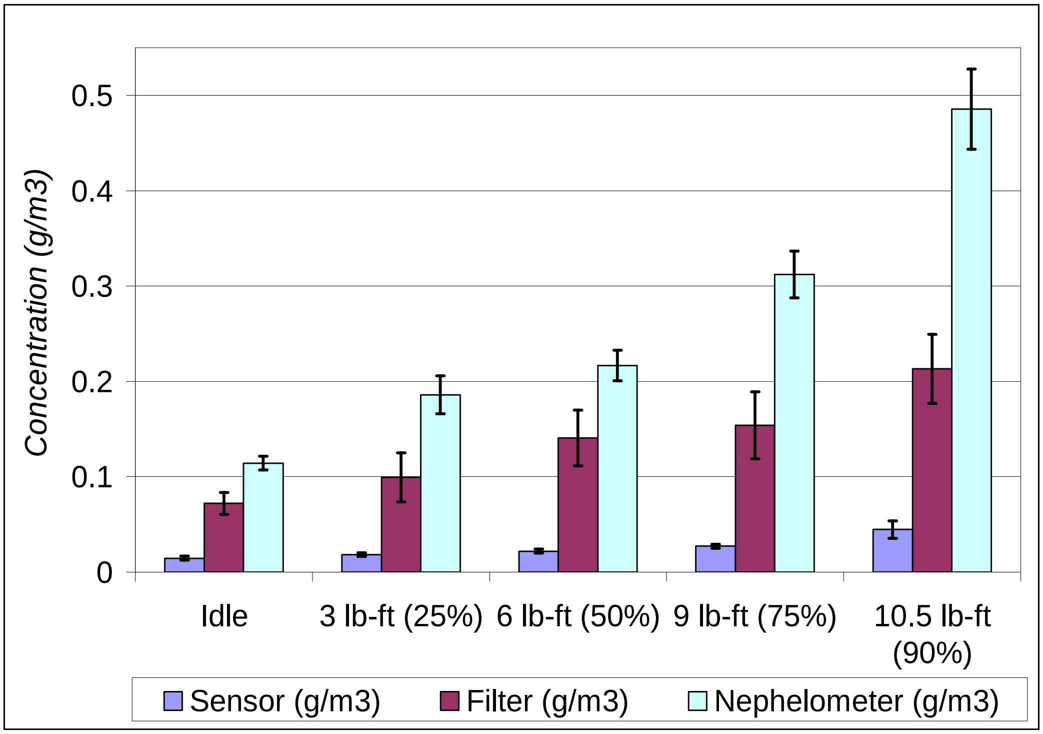

Figure 5.30: Mass loading determined by the sensor, unheated filters and nephelometer for five engine load conditions at 1250 RPM

The particle concentrations measured by the sensor were significantly lower than those measured by the unheated filters and the nephelometer. This was to be expected since the sensor is sensitive only to the carbonaceous fraction unlike the nephelometer. Overall similar trends were observed.

5.4 Aerodynamic Particle Sizer

A qualitative comparison was made between the sensor and an Aerodynamic particle Sizer (APS) to further validate the trends in sensor signal over the range of speed and load conditions tested. The APS measures number concentration of particles in the sample. The APS is capable of counting and sizing particles with aerodynamic diameters in the range of 0.5 to 20 µm. All particles with diameters below 0.5 µm are represented with a diameter of 0.3 µm. To make a qualitative comparison with the senor output it was assumed that the SOF and sulfate components of engine-out PM was composed of particles with diameters below 0.5 µm while the carbonaceous particles were in the range of 0.5 to 1 µm. The number concentrations of particles above 1 µm were close to the noise level of the APS and were thus neglected. The APS was used to measure the number concentration at five load conditions ranging from idle to 90% of full load at a constant engine speed of 1250 RPM. Figure 5.31 shows the particle concentration measured by the APS at 1250 RPM and 50% of full load. The number concentration of particles with diameters below 0.5 µm, in the exhaust sample, was significantly greater than particles with diameters in the range of 0.5 to 20 µm. This was observed to be true at all five load conditions.

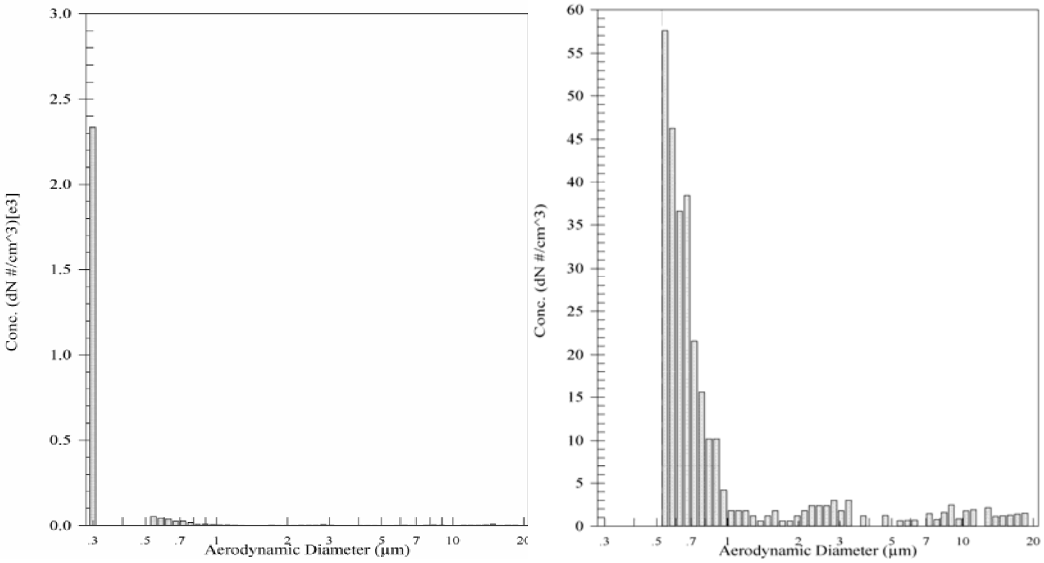

Figure 5.31: Number concentration measured by the APS at 1250 RPM and 50% of full load

The ratio of the number concentrations of the carbonaceous particles and the SOF/sulfate components were used to make a qualitative comparison with the sensor signal at an engine speed of 1250 RPM and five load conditions as shown in Figure 5.32. The C/SOF ratio has been multiplied by 5 for representation. Overall similar trends are observed between the sensor signal and the C/SOF ratio determined by the APS measurements. With increase in load the engine-out PM emissions are dominated by carbonaceous particles [7, 9, 10]. As a result the C/SOF ratio increases with engine load.

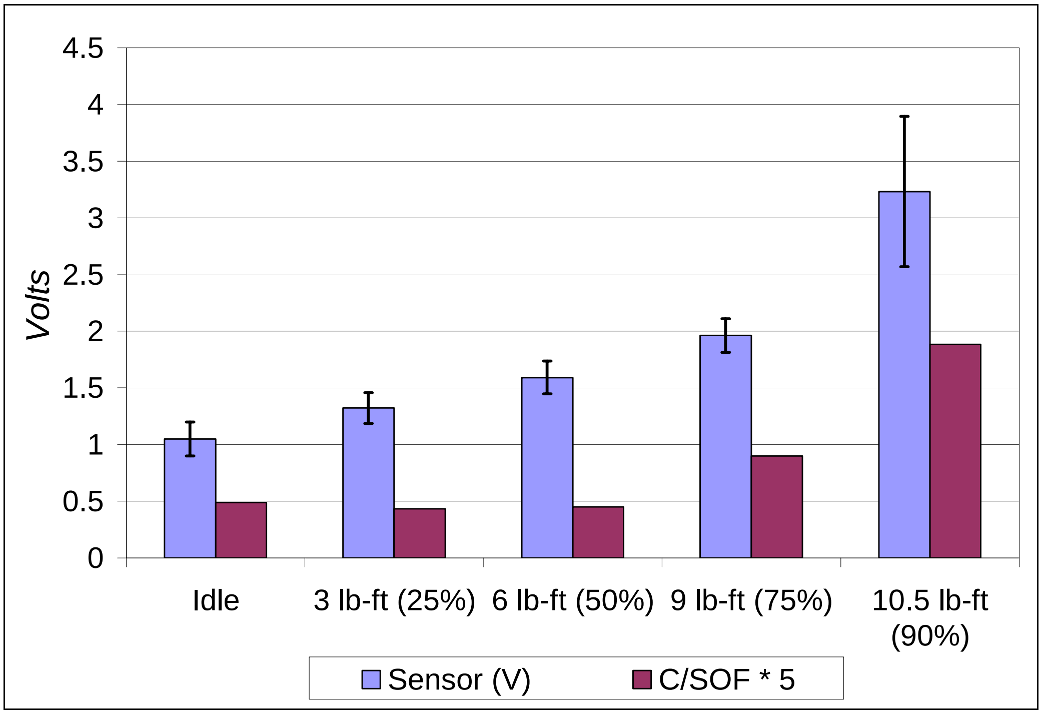

Figure 5.32: Sensor output and C/SOF ratio determined from APS measurements for five load conditions at 1250 RPM

Figure 5.33 shows the C/SOF for typical engine start. The C/SOF ratio was much greater during the first few seconds of start-up than for steady state operation at any speed/load condition. Similar trends were observed in the sensor signal and the exhaust opacity. The sensor signal and exhaust opacity during start-up were significantly greater than for either acceleration transients or for steady state operation at any speed/load condition. A big puff of 'black smoke' i.e. carbonaceous particles was observed during start-up.

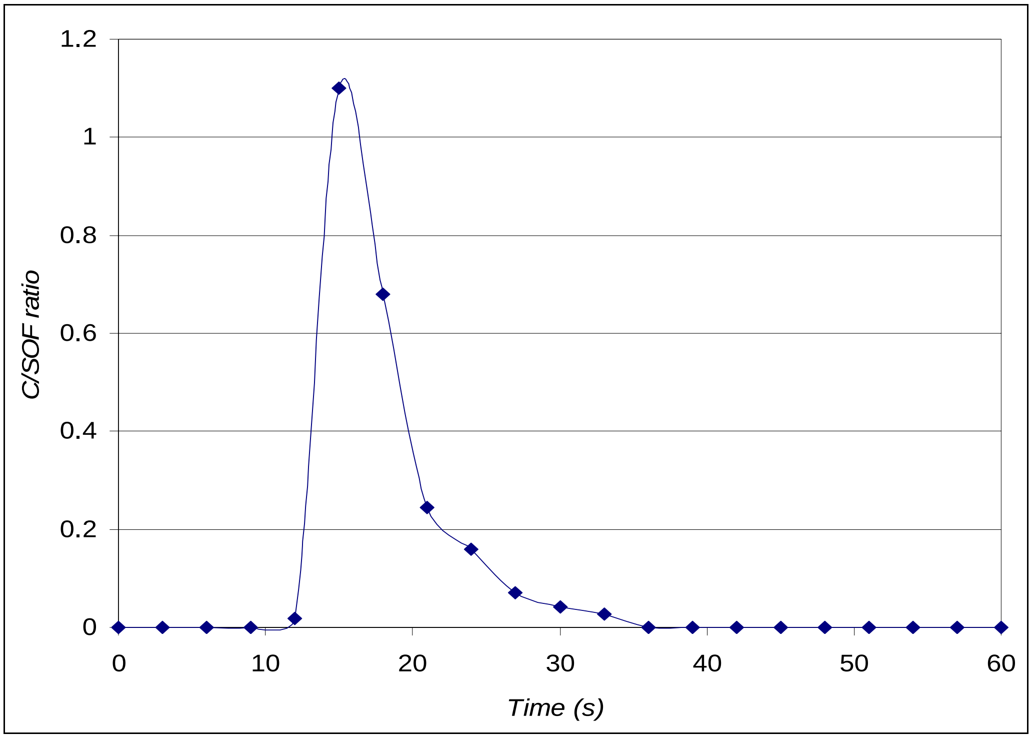

Figure 5.33: C/SOF ratio during engine start-up

Chapter 6: Conclusions and Recommendations for Future Research

A new electronic sensor for detecting particulate carbon mass emissions from engines has been developed based on the formation of an electrically conducting channel between two electrodes by the carbonaceous particles in the exhaust. The sensor is approximately the size of a standard automotive spark-plug or lambda sensor and can be mounted directly in the engine exhaust. The sensor is capable of providing cycle-resolved (or even crank-angle resolved) feedback on the carbonaceous PM concentration in the exhaust to the engine control unit (ECU), thereby enabling real-time control of engine operating parameters to lower PM emissions.

The sensor was able to resolve the differences in particulate concentration for tests carried out over a range of speed and load conditions on a diesel engine and for varying flame heights of a steady-state acetylene diffusion flame. The sensor was easily able to resolve the lowest concentrations that approached $0.01 g/m^3$. The sensor was also able to resolve transient variations in PM concentration during engine starts and accelerations. The output of the sensor compared well with exhaust opacity for the transient measurements and to filter mass loading and nephelometer for the steady-state tests. The sensor was able to detect the natural charge on particles in diesel engine exhaust, as reported in the literature, when operated without any applied bias voltage.

An experimental study of various parameters that affect the performance of the electronic sensor was conducted. Parameters considered included sensor electrode length, diameter, electrode spacing, applied bias voltage, bulk flow velocity across the sensor electrodes, and the concentration of carbonaceous particulate matter in engine exhaust. The sensor signal varied linearly with the carbon mass concentration in the exhaust, the applied bias voltage and electrode length; it varied exponentially with the bulk flow velocity, and had an inverse power dependence on the spacing between the electrodes. Electrode diameter did not have a significant effect on the sensor signal.

A correlation was developed to indicate the carbonaceous PM concentration in the exhaust in g/m^3 from the sensor output voltage under any engine operating condition and for values of the relevant design parameters. Over a range of speed and load conditions the PM concentration predicted by the sensor agreed well with filter measurements of carbonaceous PM mass emissions. The average deviation between the two was 26% for the sets of conditions examined.

Charge transport between the two electrodes was explained by a drift-diffusion mechanism. Charge (current) propogates via collisions of the individual, originally charge neutral particles with the positive high voltage electrode, followed by particle-particle collisions and particle collision with the unbiased signal electrode where electrons are extracted or due to the diffusion of the naturally charged particles in the exhaust towards the signal electrode. Another initiating mechanism for charge transport is the drift of the naturally charged particles due to the applied bias voltage of 1000 V. The presence of a high positive voltage (1000 V) causes the charged particles to move along the electric field lines towards the unbiased signal electrode. Electrons are extracted from the signal electrode when these charged particles reach the signal electrode through any of the above mentioned pathways. A 1-D electrophoresis model was developed to support this hypothesis. The current values predicted by the model compared well with the experimental measurements.

6.1 Recommendations for future work

A detailed model should be developed to gain further insights into the mechanism governing sensor behavior and to understand the dependence of the sensor signal on the bulk flow velocity. The results from the model could be compared to experiment and to a commercial modeling package like FEMLAB. FEMLAB is a modeling package for the simulation of any physical process that can be described with partial differential equations (PDEs). It offers a complete multi-physics modeling environment where the user can simultaneously solve any combination of physics. Based on the finite element method, FEMLAB provides speed and accuracy for multi-physics applications through its high-performance solvers.

On-board measurements with the sensor should be performed in the exhaust of a production vehicle equipped with a diesel engine. The sensor should be tested over different emission test cycles.

The sensor design could be further optimized to prevent sensor fouling and enhance durability. The sensor should be tested for durability by operating it in the exhaust of a diesel engine for several hours. Techniques to eliminate the drift in the sensor baseline level over time should be investigated.

Appendix A Engine Specifications

Table A.1. Yanmar L100EE Specifications (yanmar.com)

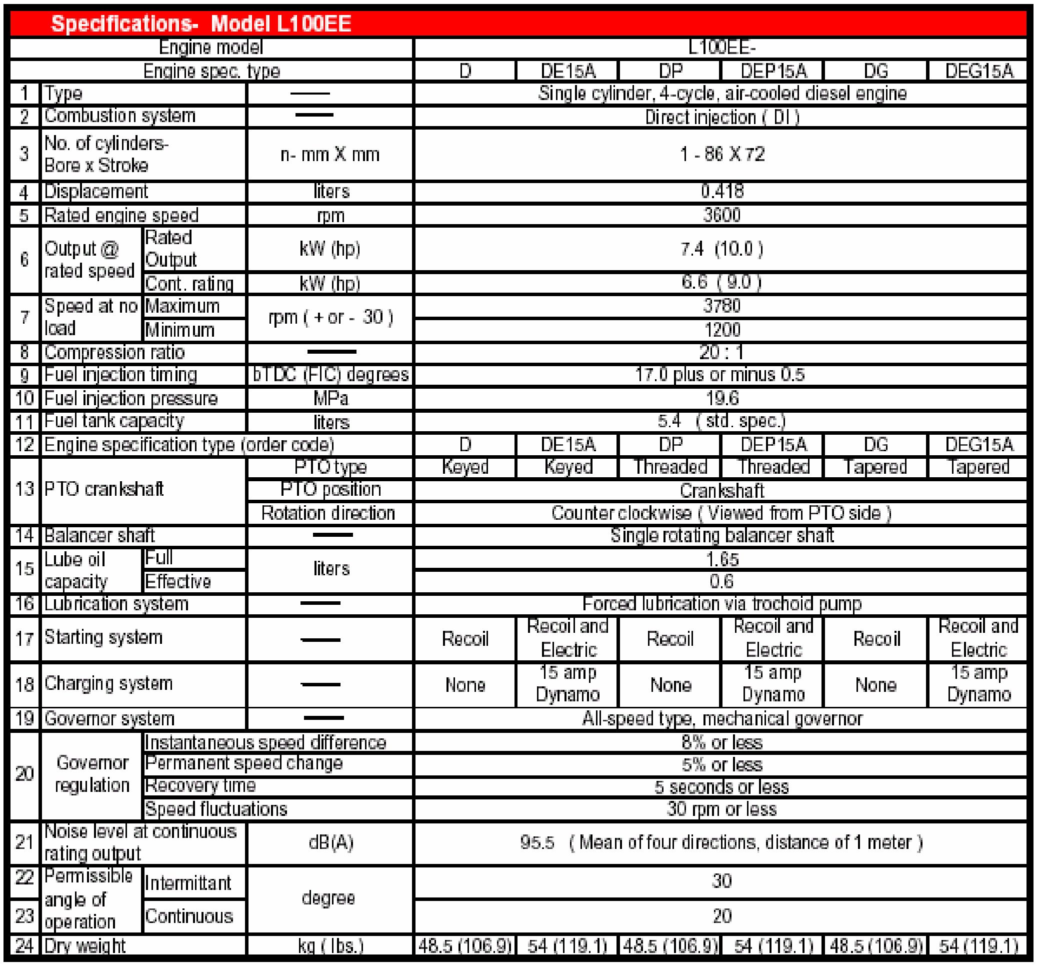

Specifications- Model L100EE

	Engine model			L100EE-					
	Engine spec. type			D	DE15A	DP	DEP15A	DG	DEG15A
1	Type		—	Single cylinder, 4-cycle, air-cooled diesel engine					
2	Combustion system		—	Direct injection (DI)					
3	No. of cylinders- Bore x Stroke		n- mm X mm	1 - 86 X 72					
4	Displacement		liters	0.418					
5	Rated engine speed		rpm	3600					
6	Output @ rated speed	Rated Output	kW (hp)	7.4 (10.0)					
		Cont. rating	kW (hp)	6.6 (9.0)					
7	Speed at no load	Maximum	rpm (+ or - 30)	3780					
		Minimum		1200					
8	Compression ratio		—	20 : 1					
9	Fuel injection timing		bTDC (FIC) degrees	17.0 plus or minus 0.5					
10	Fuel injection pressure		MPa	19.6					
11	Fuel tank capacity		liters	5.4 (std. spec.)					
12	Engine specification type (order code)			D	DE15A	DP	DEP15A	DG	DEG15A
13	PTO crankshaft		PTO type	Keyed	Keyed	Threaded	Threaded	Tapered	Tapered
			PTO position	Crankshaft					
			Rotation direction	Counter clockwise (Viewed from PTO side)					
14	Balancer shaft		—	Single rotating balancer shaft					
15	Lube oil capacity	Full	liters	1.65					
		Effective		0.6					
16	Lubrication system		—	Forced lubrication via trochoid pump					
17	Starting system		—	Recoil	Recoil and Electric	Recoil	Recoil and Electric	Recoil	Recoil and Electric
18	Charging system		—	None	15 amp Dynamo	None	15 amp Dynamo	None	15 amp Dynamo
19	Governor system		—	All-speed type, mechanical governor					
20	Governor regulation	Instantaneous speed difference		8% or less					
		Permanent speed change		5% or less					
		Recovery time		5 seconds or less					
		Speed fluctuations		30 rpm or less					
21	Noise level at continuous rating output		dB(A)	95.5 (Mean of four directions, distance of 1 meter)					
22	Permissible angle of operation	Intermittant	degree	30					
23		Continuous		20					
24	Dry weight		kg (lbs.)	48.5 (106.9)	54 (119.1)	48.5 (106.9)	54 (119.1)	48.5 (106.9)	54 (119.1)

Appendix B Error and Uncertainty Analysis

In determining the performance characteristics of the sensor a least-squares fit was applied to the sensor signal data for varying design parameters. In general, the polynomial found by least-squares technique will not fit every data point exactly. There will exist some deviation between the data point and the polynomial. The standard deviation, based on the deviation of each data point and the fit, can be defined as

$$S_{yx} = \sqrt{\frac{\sum_{i=1}^{N}\left(y_i - y_{ci}\right)^2}{\nu}} \tag{B.1}$$

where ν is the degrees of freedom of the fit, $\nu = N - (m+1)$, and m is the order of the polynomial. S_{yx} is referred to as the standard error of the fit and is the measure of the precision with which a polynomial describes the behavior of the data set [46].

B.1 Electrode Spacing

The equation describing the effect of electrode spacing on the sensor signal is as follows

$$Sensor(V) = \frac{K}{S^{1.28}} \qquad \text{(B.2)}$$

where K is a constant and S is the spacing between the two electrodes of the sensor. The equation can be transformed into

$$\log\left[Sensor(V)\right] = \log(K) - 1.28\log(S) \qquad \text{(B.3)}$$

which has the linear form

$$Y = B - 1.28X \qquad \text{(B.4)}$$

The standard error of the fit can be found using Equation B.1 at each of the five engine load conditions shown in Figure 4.2.

N = 3, m =1, $\therefore \nu = 1$

Table B.1: Standard error of fit for varying electrode spacing under five load conditions at 1250 RPM

Load @ 1250 RPM	S_{yx}
Idle	0.17
3 lb-ft (25% of full load)	0.35
6 lb-ft (50% of full load)	0.12
9 lb-ft (75% of full load)	0.61
10.5 lb-ft (90% of full load)	0.58

B.2 Electrode Length

The equation describing the effect of electrode length on the sensor signal is as follows

$$Sensor(V) = K \cdot L \tag{B.5}$$

where K is a constant and L is the length of the electrodes. The standard error of the fit can be found using Equation B.1 at each of the two engine load conditions shown in Figure 4.5.

N = 3, m =1, $\therefore \nu = 1$

Table B.2: Standard error of fit for varying electrode length under two load conditions at 1250 RPM

Load @ 1250 RPM	S_{yx}
Idle	0.08
3 lb-ft (25% of full load)	0.04

B.3 Applied Bias Voltage

The equation describing the effect of the applied bias voltage on the sensor signal is as follows

$$Sensor(V) = K \cdot V_o \tag{B.6}$$

where K is a constant and V_o is the applied voltage. The standard error of the fit can be found using Equation B.1 at idle and each of the two engine speeds shown in Figure 4.6.

N = 3, m =1, $\therefore \nu = 1$

Table B.3: Standard error of fit for different values of the applied bias voltage at two engine speeds of 1250 and 1500 RPM

Idle	S_{yx}
1250 RPM	0.16
1500 RPM	0.04

B.4 Flow Velocity

The equation describing the effect of flow velocity on the sensor signal is as follows

$$Sensor(V) = K\,e^{0.62U} \qquad \text{(B.7)}$$

where K is a constant and V is the flow velocity. The equation can be transformed into

$$\ln\left[Sensor(V)\right] = \ln(K) + 0.62U \qquad \text{(B.8)}$$

which has the linear form

$$Y = B + 0.62U \qquad \text{(B.9)}$$

The standard error of the fit can be found using Equation B.1 for the four sensor designs described in Table 4 at idle and engine speeds of 1250, 1500 and 2000 RPM.

N = 3, m =1, $\therefore \nu = 1$ at each engine speed.

Table B.4: Standard error of fit for ‘Sensor 1’

Engine Speed (RPM)	S_{yx}
1250	0.55
1500	0.79
2000	1.0

Table B.5: Standard error of fit for ‘Sensor 2’

Engine Speed (RPM)	S_{yx}
1250	0.09
1500	0.09
2000	0.12

Table B.6: Standard error of fit for ‘Sensor 3’

Engine Speed (RPM)	S_{yx}
1250	0.09
1500	0.27
2000	0.38

Table B.7: Standard error of fit for ‘Sensor 4’

Engine Speed (RPM)	S_{yx}
1250	0.1
1500	0.09
2000	0.16

B.5 Carbon Mass Concentration

The equation describing the effect of the carbon mass concentration in the exhaust on the sensor signal is as follows

$$Sensor(V) = K \cdot C \qquad \text{(B.10)}$$

where K is a constant and C is the concentration of carbonaceous particles in the exhaust.. The standard error of the fit was computed using Equation B.1 for ‘Sensor 1’ and Sensor 3’ described in Table 5. The experiments were performed at a constant engine speed of 1250 RPM and five load conditions ranging from idle to 90% of full load.

For both sensors, N = 18, m =1, $\therefore \nu = 16$

Table B.8: Standard error of fit for the two sensors

	S_{yx}
Sensor 1	0.56
Sensor 3	0.23

B.6 Uncertainty Analysis

The dry soot concentration in the exhaust for any engine operating condition and sensor geometry can be expressed as follows

$$C(g/m^3) = \frac{Sensor(V) * S^{1.28}}{K \cdot LV_o e^{0.62U}} \qquad \text{(B.11)}$$

The uncertainty in the soot concentration measured by the sensor can be computed as follows

$$u_C = \pm\sqrt{\left[\left(\frac{\partial C}{\partial Sensor(V)}u_{Sensor(V)}\right)^2 + \left(\frac{\partial C}{\partial S}u_S\right)^2 + \left(\frac{\partial C}{\partial L}u_L\right)^2 + \left(\frac{\partial C}{\partial V_o}u_{V_o}\right)^2 + \left(\frac{\partial C}{\partial U}u_U\right)^2\right]} \tag{B.12}$$

where C is the carbon mass concentration in g/m^3, S and L are the spacing between the electrodes and the length in meters respectively, V_o is the applied bias voltage in volts and V is the bulk flow velocity in m/s.

$$\frac{\partial C}{\partial Sensor(V)} = \frac{S^{1.28}}{KLV_o e^{0.62U}}\,;\ u_{Sensor(V)} = S_{yx}$$

$$\frac{\partial C}{\partial S} = \frac{1.28 \cdot Sensor(V) \cdot S^{0.28}}{KLV_o e^{0.62U}}\,;\ u_S = \frac{Least.Count}{2} = 4 * 10^{-04}\,m$$

$$\frac{\partial C}{\partial L} = -\frac{Sensor(V) \cdot S^{1.28}}{KL^2 V_o e^{0.62U}}\,;\ u_L = \frac{Least.Count}{2} = 4 * 10^{-04}\,m$$

$$\frac{\partial C}{\partial V_0} = -\frac{Sensor(V) \cdot S^{1.28}}{KLV_o^2 e^{0.62U}}\,;\ u_{V_o} = \frac{Least.Count}{2} = 25V$$

$$\frac{\partial C}{\partial U} = -\frac{0.62 \cdot Sensor(V) \cdot S^{1.28}}{KLV_o e^{0.62U}}\,;\ u_U = 0m/s \,\&\, u_U = 0.5m/s$$

The uncertainty in the dry soot concentration measured by a typical sensor is computed at 1250 RPM and five load conditions ranging from idle to 90% of full load using Equation B.12. The uncertainty values at the five engine operating conditions are given in Table B.9 for zero-order uncertainty in the bulk flow velocity and in Table B.10 for an uncertainty of 0.5 m/s in the flow velocity.

Table B.9: Uncertainty values at the five engine operating conditions for zero-order uncertainty in the flow velocity

Load @ 1250 RPM	$u_C (g/m^3)$
Idle	± 0.005
3 lb-ft (25% of full load)	± 0.006
6 lb-ft (50% of full load)	± 0.007
9 lb-ft (75% of full load)	± 0.009
10.5 lb-ft (90% of full load)	± 0.017

Table B.10: Uncertainty values at the five engine operating conditions for an uncertainty of 0.5 m/s in the flow velocity

Load @ 1250 RPM	$u_C (g/m^3)$
Idle	± 0.007
3 lb-ft (25% of full load)	± 0.008
6 lb-ft (50% of full load)	± 0.01
9 lb-ft (75% of full load)	± 0.012
10.5 lb-ft (90% of full load)	± 0.022

References

[1] EPA. *Health Assessment Document for Diesel Exhaust*, 2000 http://www.epa.gov/nceawww1/pdfs/diesel/ch1final.pdf

[2] Mehta, D., "The development of a Nephelometer System for Time-Resolved Particulate Measurements from Direct Injection Spark Ignition Engines", M.S Thesis, Department of Mechanical Engineering, The University of Texas at Austin, 2000

[3] Witze, P.O., "Diagnostics for the Measurement of Particulate Matter Emissions from Reciprocating Engines", *Proceedings of the Fifth International Symposium on Diagnostics and Modeling of Combustion in Internal Combustion Engines* - *COMODIA 2001*, 2001.

[4] Stovell, C.H., R.D. Matthews, B.E. Johnson, H. Ng and B. Larsen, "Emissions and Fuel Economy of a 1998 Toyota with a Direct Injection Spark Ignition Engine", SAE Paper 1999-01-1527, 1999.

[5] Hendrix, B., "Development of a Production Style Probe to Measure Particulate Emissions in Commercial Diesel Engine Exhaust", M.S Thesis, Department of Mechanical Engineering, The University of Texas at Austin, 2002.

[6] Warey, A., "Effects of In-Cylinder Wall Wetting on Size and Mass of Particulate Matter Emissions in Direct Injection Spark Ignition Engines", M.S Thesis, Department of Mechanical Engineering, The University of Texas at Austin, 2003.

[7] Kayes, D. and S. Hochgreb, "Mechanisms of Particulate Matter Formation in Spark-Ignition Engines: (1) Effect of Engine Operating Conditions. Environmental Science and Technology", 33(22), 1999.

[8] Kayes, D. and S. Hochgreb, "Mechanisms of Particulate Matter Formation in Spark-Ignition Engines: (2) Effect of Fuel, Oil, and Catalyst Parameters. Environmental Science and Technology", 33(22), 1999.

[9] Kayes, D. and S. Hochgreb, "Mechanisms of Particulate Matter Formation in Spark-Ignition Engines: (3) Model of PM Formation", Environmental Science and Technology, 33(22), 1999.

[10] Heywood, J.B., "Internal Combustion Engine Fundamentals", McGraw-Hill, 1988

[11] Snelling, D.R., G.J. Smallwood, R.A. Sawchuk, W.S. Neill, D. Gareau, W.L. Chippior, F. Liu, O.L. Gülder and W.D. Bachalo, "Particulate Matter Measurements in a Diesel Engine Exhaust by Laser-Induced Incandescence and the Standard Gravimetric Procedure", SAE Paper 1999-01-3603, 1999.

[12] Matthews, R.D., "Internal Combustion Engines and Automotive Engineering", Draft Textbook.

[13] Kayes, D., S. Hochgreb, M.M. Marciq, D.H. Podsiadlik and R.E. Chase, "Particulate Matter Emission During Start-up and Transient Operation of a Spark-Ignition Engine (2): Effect of Speed, Load, and Real-World Driving Cycles", SAE Paper 2000-01-1083, 2000.

[14] Marciq, M.M., R.H. Munoz, J. Yang and R.W. Anderson, "Sooting Tendencies in an Air-Forced Direct Injection Spark-Ignition (DISI) Engine", SAE Paper 2000-01-0255, 2000.

[15] Stevens, E., and R. Steeper, "Piston Wetting in an Optical DISI Engine: Fuel Films, Pool Fires, and Soot Generation", SAE Paper 2001-01-1203, 2001.

[16] Okrent, D.A., "Optimization of a Third Generation TEOM Monitor for Measuring Diesel Particulate in Real-Time", SAE Paper 980409, 1998.

[17] TEOM Series 1105 Diesel Particulate Monitor, Product Information Brochure, Rupprecht & Patashnick Co., Inc.

[18] Model 3936-Series Scanning Mobility Particle Sizer, Product Information Brochure, TSI Incorporated.

[19] Source Test Cascade Impactor, Operations Manual, M.J. Pilat, Department of Civil Engineering, University of Washington, Seattle, 1998. www.cascadeimpactor.com/publications/opman.htm

[20] Electrical Low Pressure Impactor (ELPI), Product Information Brochure, Dekati Ltd.

[21] Witze, P.O. and B. Axelson, "Qualitative Laser-Induced Incandescence Measurements of Particulate Emissions During Transient Operation of a TDI Diesel Engine", SAE Paper 2001-01-3574, 2001.

[22] Witze, P.O., "Real-Time Measurement of the Volatile Fraction of Diesel Particulate Matter Using Laser-Induced Desorption with Elastic Light Scattering (LIDELS)", SAE Paper 2002-01-1685, 2002.

[23] Smallwood, G.J., D.R. Snelling, W.S. Neill, F. Liu, W.D. Bachalo and O.L. Gülder, "Laser-Induced Incandescence Measurements of Particulate Matter Emissions in the Exhaust of a Diesel Engine", *Proceedings of the Fifth International Symposium on Diagnostics and Modeling of Combustion in Internal Combustion Engines - COMODIA 2001*, 2001.

[24] Schweimer, G.W., “Ion Probe in the Exhaust Manifold of Diesel Engines”, SAE Paper 860012, 1986.

[25] Collings, N., N. Baker, W.G. Wolber, “Real-Time Smoke Sensor for Diesel Engines”, SAE Paper 860157, 1986.

[26] Hong, G., N. Collings and N.J. Baker, “Diesel Smoke Transient Control Using a Real-Time Smoke Sensor”, SAE Paper 871629, 1987.

[27] Allan, W.D.E., R.D. Freeman, G.R. Pucher, D. Faux, M.F. Bardon and D.P. Gardiner, “Development of a Smoke Sensor for Diesel Engines”, SAE Paper 2003-01-3084, 2003.

[28] Ishida, K., "Study of Continuous Measurement Method for Diesel Exhaust Emissions”, Horiba Internal Paper, Horiba Instruments Inc.

[29] Stanard, A.P., "Study of the Effects of Water-Emulsified Diesel Fuel on the Performance and Emissions of a Single Cylinder Direct Injection Diesel Engine”, M.S Thesis, Department of Mechanical Engineering, The University of Texas at Austin, 2003.

[30] Warey, A., B. Hendrix, M. Hall and T. Nevius, “A New Sensor for On-Board Detection of Particulate Carbon Mass Emissions from Engines”, SAE Paper 2004-01-2906, 2004.

[31] Kim, N., "Emissions and Engine Performance of an Ultra-Low Sulfur Diesel Fuel in a Utility DI Diesel Engine”, M.S Thesis, Department of Mechanical Engineering, The University of Texas at Austin, 2004.

[32] Mehta, D., T. Alger, M. Hall and R. Matthews, "Particulate Characterization of a DISI Research Engine using a Nephelometer and In-Cylinder Visualization", SAE Paper 2001-01-1976, 2001.

[33] Smyth, K.C. and C.R. Shaddix, "The Elusive History of m = 1.57-0.56i for the Refractive Index of Soot", Combustion and Flame, 107, 1996.

[34] Model 3320 Aerodynamic Particle Sizer Spectrometer, Instruction Manual, TSI Incorporated.

[35] Cheung, T.K., "Development of a Scanning Nephelometer for Rapid Particle Size Analysis", M.S Thesis, Department of Mechanical Engineering, The University of Texas at Austin, 2004.

[36] Model 3302A Aerosol Diluter, Product Information Brochure, TSI Incorporated.

[37] OPA111AM-ND, Technical Catalog, Digi-Key Corporation.

[38] OPA128JM-ND, Technical Catalog, Digi-Key Corporation.

[39] Koenig, M.H., "Development of an Infrared Fiber Optic Instrumented Sparkplug for Measuring Local Fuel Concentrations in Fired Liquid Fueled SI Engines", Ph.D. Dissertation, Department of Mechanical Engineering, The University of Texas at Austin, 1997.

[40] Vincenti, W.G. and C.H. Kruger, “Introduction to Physical Gas Dynamics”, R. Krieger Publishing Company, 1982.

[41] Mitchner, M. and C.H. Kruger, “Partially Ionized Gases”, John Wiley & Sons.

[42] Barve, V.V., “Simulation of Gravitational Settling under Electric Fields”, M.S Thesis, Department of Mechanical Engineering, The University of Texas at Austin, 2002.

[43] Friedlander, S.K., “Smoke Dust and Haze: Fundamentals of Aerosol Behavior”, John Wiley & Sons.

[44] Upadhyay, R.R. and O.A. Ezekoye, “Treatment of Size Dependent Aerosol Transport Processes using Quadrature based Moment Methods”, Accepted for publication, Journal of Aerosol Science.

[45] Wagner, R.M., J.B. Green, Jr., J.M Storey and C.S. Daw, “Extending Exhaust Gas Recirculation Limits in Diesel Engines”, Internal Paper, Oak Ridge National laboratory.

[46] Figolia, R.S. and D.E. Beasley, "Theory and Design for Mechanical Measurements", 3 ed., John Wiley & Sons, 2000.

VITA

Alok Arun Warey was born in Nagpur, India on July 19, 1978. After completing school in 1996, he enrolled in the Mechanical Engineering program at Regional Engineering College, Tiruchirappalli, India. He received the degree of Bachelor of Engineering (First class with distinction) in Mechanical Engineering in May 2000. The following semester, he began his graduate research work at The University of Texas at Austin with the Combustion Research group. He received the degree of Master of Science in Mechanical Engineering in August 2003.

Permanent address: 08A Tower D, Viceroy Park, Thakur Village,
Kandivali (E), Mumbai 400101
India.

This dissertation was typed by the author.